Thesis for the degree
Master of Science

Submitted to the Scientific Council of the
Weizmann Institute of Science
Rehovot, Israel

עבודת גמר (תזה) לתואר
מוסמך למדעים

מוגשת למועצה המדעית של
מכון ויצמן למדע
רחובות, ישראל

By
Yotam Shapira

מאת
יותם שפירה

שזירה עמידה של קיוביטים במערכת יונים לכודים
Robust entanglement of trapped ion qubits

Advisor:
Prof. Roee Ozeri

מנחה:
פרופ' רועי עוזרי

December 2017

טבת תעש"ח

First and foremost, I would like to thank my advisor, Roee Ozeri, for teaching me how a physicist thinks and for having the patience to wait for me to catch up with this way of thinking (while listening to my endless ramblings). I would like to thank the 185 lab team: Ravid Shaniv and Tom Manovitz, which exist in a superposition of being my partners and my teachers in this endeavor, which could not have existed without them. I would also like to thank all the trapped ions group members: Nitzan, Ziv, Tomas, Ruti, Lee, Meirav & Yonatan, for their support, interest and ideas.

Lastly I would like to thank my spouse Shahaf, who gracefully managed to simultaneously be my partner in life and a critical-thinking physicist. This work is dedicated to you.

"*The reason anyone would do this is, if they could, which they can't, would be because they could, which they can't.*"

— Pickle Rick, Rick and Morty (2017)

Contents

1 Introduction

Quantum information processing (QIP) is a field in quantum physics which deals with carefully controlling quantum carriers of information in order to perform computational tasks. The Hilbert space structure of quantum theory, namely the existence of superposition and entanglement, introduces a variety of computational tools which pertain capabilities that are not allowed in classical information theory. A celebrated example for such capabilities is attributed to Peter Shor who in 1995 proposed a quantum algorithm for factorizing an integer in polynomial time (in the size of the input), as opposed to sub-exponential time in classical computers [1] .

A basic concept of QIP is that of the quantum bit (qubit), which is the quantum analog of the (classical) bit. The qubit is a quantum two level system (usually denoted by the states $|0\rangle$ and $|1\rangle$) which constitutes the building block of any quantum information process, in the sense that any quantum information process involves controlling and measuring a register of (usually many) qubits.

The "holy grail" of this field is probably the quantum computer, a digital fully controllable QIP machine, which has already been implemented in several proof-of-principle experiments, however a large scale quantum computer which surpasses the classical computer capabilities remains elusive [2]. The DiVincenzo criteria specify the necessary properties of a system for it to be a quantum computer [3]. These include:

1. A scalable physical system with well characterized qubits.
2. A "universal" set of quantum gates.
3. Long relevant coherence times as compared with the typical gate time.
4. The ability to initialize the state of the qubits to a simple fiducial state.
5. A qubit-specific measurement capability.

The crux of these criteria relates in a circular fashion to scalability, universality and long coherence times. It has been shown that the ability to perform any single qubit rotations and to perform a controlled-NOT gate on any 2 qubits of the register is sufficient to arbitrarily approximate any unitary operator in Hilbert space [4]. In other words, single qubit rotations and a 2 qubit controlled-NOT gate constitute a universal gate set (criterion 2). However the performance of these operations, especially entanglement, is greatly reduced when attempting to coherently control many qubits or maintaining long coherence times in a noisy environment, however a more fundamental explanation lies in the exponential growth of Hilbert space dimension with the number of qubits (accompanied by the exponential growth of the noisy Liouville space).

It is widely agreed that overcoming these challenges is possible only by using active error correcting methods. In analogy to classical error correction, quantum error correction (QEC) encodes a single logical qubit state in many physical qubits, such that errors in the physical qubits may be monitored in an iterative fashion, and corrected, thus allowing for decoherence-free logical systems and correction of control errors. However all QEC schemes inherently

make use of entangling gates, thus we seem to be stuck in a loop, where high fidelity operations are needed in order to maintain high fidelity operations.

However, Dorit Aharonov and others have shown that a noisy quantum computer may simulate a noise-less quantum computer provided that the level of noise is below a certain threshold [5] - this is the celebrated quantum fault-tolerance theorem. To put more simply - the loop may be broken by almost implementing DiVincenzo's criteria, we need to implement a "good enough" universal gate set which can then simulate a perfect one. This understanding has motivated many works and proposals aiming at optimal QEC methods and implementing high fidelity and robust operations.

It is also worth mentioning that even though a fully functional quantum computer has yet to appear, more modest, yet extremely beneficial avenues of QIP have already been successfully implemented and used, these include: precise measurements using QIP tools [6, 7, 8, 9, 10], quantum simulations [11, 12] etc. These generally also make use of entangling gates and depend on high fidelity operations.

Trapped ions are systems where ions are electrically trapped in (usually) linear chains. These systems are well understood and highly controllable and are thus considered a leading platform for QIP experiments. The ions have typically long life times in the trap and may be cooled, initialized, controlled and measured by applying different laser and microwave transitions. Typically a short lived fluorescent internal transition is used to Doppler cool and measure the ion state, and two internal long lived levels are used to encode the logical state $|0\rangle$ and $|1\rangle$. The normal modes of ions in the crystal can be treated as uncoupled harmonic oscillators, which can selectively couple between different ions.

Thus, trapped ions systems are a prime platform for exploring high fidelity and robust methods for entangling qubits. Indeed, recently a host of proposals and realizations for entangling gates appeared which focus on methods to optimize robustness, increase fidelity and minimize operation time [13, 14, 15, 16, 17, 18]. Most of which are based on the well known Mølmer-Sørensen entangling gate [19, 20] and aim towards a stable and reliable realization of arbitrary two qubit entangling gate in a large qubit register.

This work aims to add some analytical and intuitive interpretation for increasing gate robustness, propose methods to reduce certain error mechanisms and most importantly demonstrate these methods experimentally.

2 Theory

Here we introduce the theoretical background for the experiments. Specifically, the first sub-section provides a brief overview of trapped ion - laser interactions, the second sub-section describes the Mølmer-Sørensen (MS) gate by following [19, 20], which is used as a basis for this work. Then we show in detail an analytical solution of the MS gate evolution by tracing out external degrees of freedom (a more compact derivation is provided in [13]).

The next sub-sections introduce the composite entangling gate, and show how additional degrees of freedom in it allow to optimize robustness to gate timing-errors, off resonance couplings and harmonic trap frequency errors. These are, to the best of knowledge, all new results.

2.1 Ion-light interaction

To demonstrate how trapped ions act as qubits we quickly derive the interaction of a trapped ion with a classical electromagnetic field created by a laser (semi-classical approximation). We consider a hydrogen-like ion, that is, a charged atom with one electron in the valence shell, we assume that all other electrons remain in a fixed state such that the only degrees of freedom are those of the valence electron and the center of mass coordinates of the ion.

The Hamiltonian is of the form:

$$\hat{H} = \hat{H}_{\text{ion}} + \hat{V}_{\text{ion-laser}} \tag{1}$$

Such that:

$$\begin{cases} \hat{H}_{\text{ion}} = & \sum_{\boldsymbol{n}} E_{\boldsymbol{n}} \left|\boldsymbol{n}\right\rangle \left\langle \boldsymbol{n}\right| + \hbar\nu \hat{a}^{\dagger}\hat{a} \\ \hat{V}_{\text{ion-laser}} = & \sum_{\boldsymbol{n}\neq\boldsymbol{m}} \Omega_{\boldsymbol{n},\boldsymbol{m}} \left|\boldsymbol{n}\right\rangle \left\langle \boldsymbol{m}\right| \cos\left(k\hat{x} - \omega_l t + \phi\right) \end{cases} \tag{2}$$

Where $|\boldsymbol{n}\rangle$ is the state of the (valence electron of the) ion, $E_{\boldsymbol{n}}$ is the eigen-energy of associated with the state, ν is the harmonic trap frequency and $\hat{a}$ is the harmonic trap lowering operator (the atom's center of mass degrees of freedom), for simplicity we consider here only a 1d trap, the extension to 3d is trivial. We note there is no electromagnetic field free Hamiltonian since this is a semi-classical approximation,

The semi-classical interaction is given by a plane wave with frequency ω_l and an effective Rabi frequency $\Omega_{\boldsymbol{n},\boldsymbol{m}}$ which corresponds to the leading order coupling between $|\boldsymbol{m}\rangle$ and $|\boldsymbol{n}\rangle$ in a multipole expansion. Here we make use of the a dipole forbidden quadropole allowed transition (as is described in more detail in 3). In addition we used a wave vector,k, in the trap direction (the extension to 3d is trivial).

An effective two level system is formed by detuning the laser to a specific transition between two states. For this purpose we will use one state from the $S_{\frac{1}{2}}$ manifold and one from the $D_{\frac{5}{2}}$ manifold which we loosely denote as $|S\rangle$ and $|D\rangle$ respectively and assume (wlog) that $E_S = 0$. The crucial points is that by tuning the laser such that, except for the $|S\rangle \leftrightarrow |D\rangle$ transition, all transitions obey $\left|\frac{\hbar\Omega_{\boldsymbol{n},\boldsymbol{m}}}{\hbar\omega_l - (E_{\boldsymbol{m}} - E_{\boldsymbol{n}})}\right| \ll 1$.

By changing to an interaction picture with respect to $\hat{H}_{rot} \equiv \sum_{\boldsymbol{n}} E_{\boldsymbol{n}} |\boldsymbol{n}\rangle \langle \boldsymbol{n}| + \hbar\delta |D\rangle \langle D|$ with $\hbar\delta = \hbar\omega_l - E_D$ then all the detuned transitions may then be neglected in a rotating wave approximation (RWA). We obtain:

$$\hat{H}_{TLS} = \frac{\hbar\delta}{2}\hat{\sigma}_z + \hbar\nu\hat{a}^\dagger\hat{a} + \frac{\Omega}{2}\left(\hat{\sigma}_+ e^{-i\eta\left(\hat{a}^\dagger+\hat{a}\right)}e^{-i\phi} + h.c\right) + \mathcal{O}\left(\frac{\Omega}{\omega_l}\right) \tag{3}$$

Where we used $\Omega \equiv \Omega_{SD}$, assumed it is real (any phase in it can be absorbed in ϕ) and shifted the Hamiltonian by $\frac{\hbar\delta}{2}$ to rewrite in terms of Pauli matrices. The important point here is that this Hamiltonian exclusively couples the states $|S\rangle$,$|D\rangle$ and no other. This is effectively a two level system (TLS) Hamiltonian for the internal degrees of freedom.

In addition we have introduced the Lamb-Dicke parameter by using:

$$k\hat{x} = k\sqrt{\frac{\hbar}{2m\nu}}\left(\hat{a}^\dagger + \hat{a}\right) \equiv \eta\left(\hat{a}^\dagger + \hat{a}\right) \tag{4}$$

This parameter measures the ratio of the harmonic wave function extent to the optical wavelength. As we will shortly show the nomenclature is appropriate since the optical field acting on the moving ion is a frequency modulation in the reference frame of the ion. To show this we rotate once again with respect to $\frac{\hbar\delta}{2}\hat{\sigma}_z + \hbar\nu\hat{a}^\dagger\hat{a}$. By using the identities:

$$\begin{cases} e^{i\frac{\delta}{2}\hat{\sigma}_z}\hat{\sigma}_+ e^{-i\frac{\delta}{2}\hat{\sigma}_z} & = \hat{\sigma}_+ e^{i\delta t} \\ e^{i\nu\hat{a}^\dagger\hat{a}}e^{-i\eta\left(\hat{a}^\dagger+\hat{a}\right)}e^{-i\nu\hat{a}^\dagger\hat{a}} & = e^{-i\eta\left(\hat{a}^\dagger e^{i\nu t}+\hat{a}e^{-i\nu t}\right)} \end{cases} \tag{5}$$

We obtain the interaction picture TLS Hamiltonian

$$\hat{H}_{TLS,I} = \frac{\Omega}{2}\left(\hat{\sigma}_+ e^{i\delta t}e^{-i\eta\left(\hat{a}^\dagger e^{i\nu t}+\hat{a}e^{-i\nu t}\right)}e^{-i\phi} + h.c\right) + \mathcal{O}\left(\frac{\Omega}{\omega_l}\right) \tag{6}$$

Assuming $\eta \ll 1$, i.e. that we are well within the Lamb-Dicke Regime, we expand the exponent to obtain:

$$\hat{H}_{TLS,I} = \hat{H}_C + \hat{H}_{RSB} + \hat{H}_{BSB} + \mathcal{O}\left(\frac{\Omega}{\omega_l}, \eta^2\right) \tag{7}$$

Where the three terms are carrier, red side-band (RSB), blue side-band (BSB) respectively:

$$\begin{cases} \hat{H}_C & = \frac{\Omega}{2}\hat{\sigma}_+ e^{i(\delta t-\phi)} + h.c \\ \hat{H}_{RSB} & = -\frac{i\eta\Omega}{2}\hat{\sigma}_+\hat{a}e^{-i(\nu-\delta)t}e^{-i\phi} + h.c \\ \hat{H}_{BSB} & = -\frac{i\eta\Omega}{2}\hat{\sigma}_+\hat{a}^\dagger e^{i(\nu+\delta)t}e^{-i\phi} + h.c \end{cases} \tag{8}$$

Here we get three types of possible interactions. For $\delta = 0$ the carrier transition is resonant and we perform a $\hat{\sigma}_\phi$ rotation without affecting the external degrees of freedom. For $\delta = \nu$ the RSB Hamiltonian is resonant and we

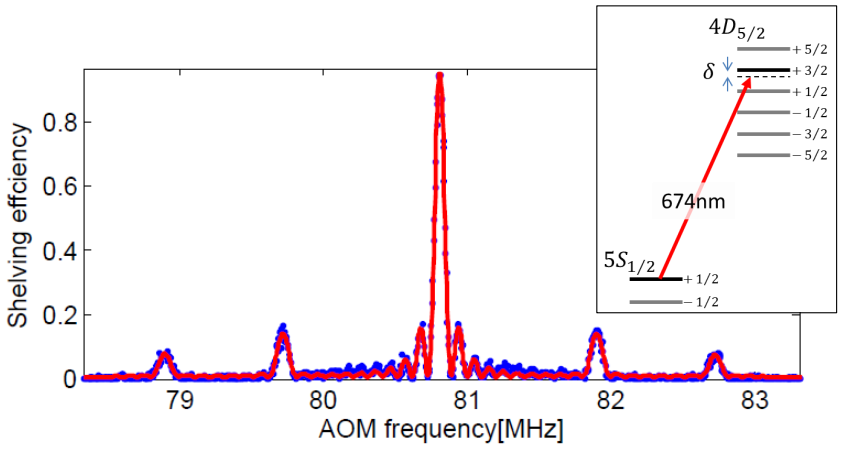

Figure 1: **Spectroscopic scan of $5S_{\frac{1}{2},+\frac{1}{2}} \longrightarrow 4D_{\frac{5}{2},+\frac{3}{2}}$ transition of a single $^{88}Sr^{+}$ ion** (adapted from Fig. 3.13 of [21]). Here the horizontal axis shows the detuning of the optical field frequency and the vertical axis measures the ratio of population in the $|D\rangle$ state. $\delta = 0$ corresponds to the peak slightly left of 81 MHz. Approximately 1 MHz apart in each direction smaller resonances are observed which correspond to the blue and red side-band respectively. The next two peaks on the right and left correspond to side-bands of an orthogonal mode of the 3d harmonic oscillator. The inset shows the relevant levels of a single $^{88}Sr^{+}$ ion and the coupling laser (not to scale). As long as the Rabi frequency is small enough only the two $|S\rangle$ and $|D\rangle$ levels (bold black) are coupled, here $|S\rangle \equiv \left|5S_{\frac{1}{2},+\frac{1}{2}}\right\rangle$ and $|D\rangle \equiv \left|4D_{\frac{5}{2},+\frac{3}{2}}\right\rangle$.

excite the ion from $|S\rangle$ to $|D\rangle$, while annihilating a phonon from the harmonic degree of freedom (or reciprocally, de-exciting the ion while creating a phonon), this term is the well known Janes-Cummings Hamiltonian in quantum optics. Similarly, by choosing $\delta = -\nu$ the BSB Hamiltonian is resonant and we excite the ion while creating a phonon. Since typically $\nu \gg \eta\Omega$ the side-band transitions are usually suppressed (in a RWA) when using $\delta = 0$, while the opposite is not always true.

Reminding that $\hat{a}\,|n\rangle = \sqrt{n}\,|n-1\rangle$, we note that the appearance of the ladder operators in the side-band Hamiltonians allows employing these transition for thermometry. That is the effective Rabi frequency of these transitions depends on the harmonic state, thus by measuring the population oscillations under such a Hamiltonian and Fourier transforming one may extract the population in each harmonic state.

We observe these resonances by scanning the laser detuning δ and measuring the excited population (details on exactly how this is done are given in 3). Indeed, Fig. 1 shows a spectroscopic scan experiment on a $5S_{\frac{1}{2},+\frac{1}{2}} \longrightarrow 4D_{\frac{5}{2},+\frac{3}{2}}$ transition of a single $^{88}Sr^{+}$ ion (adapted from Fig 3.13 of [21]), in which a main carrier resonance is easily observed and smaller side-band resonances are also observable.

It is possible to obtain a more refined form of Eq. 7 without assuming $\eta \ll 1$, by expanding the exponent $e^{-i\eta\left(\hat{a}^{\dagger}e^{i\nu t}+\hat{a}e^{-i\nu t}\right)}$ and gathering raising and lowering terms. The Hamiltonian is then given by:

$$\begin{cases} \left\langle D;n'\left|\hat{H}_{TLS,I}\right|S;n\right\rangle = \frac{\Omega}{2}e^{-i\left[\delta-\left(n'-n\right)\nu t\right]}D_{n,n'} \\ D_{n,n'} = \left\langle n'\left|e^{i\eta\left(\hat{a}^{\dagger}+\hat{a}\right)}\right|n\right\rangle = e^{-\frac{\eta^2}{2}}\left[\frac{n_<!}{n_>!}\right]^{\frac{1}{2}}\eta^{\left|n-n'\right|}L_{n_<}^{\left|n-n'\right|}\left(\eta^2\right) \end{cases} \tag{9}$$

Where $D_{n,n'}$ is the Debye-Waller factor (the overlap between a displaced initial wave function and some destination wave function) and $L^{\alpha}_{n_<}$ is the modified Laguerre polynomial such that $n_< = \min(n, n')$ and $n_> = \max(n, n')$. At this point we may take the limit $\eta \ll 1$ in a more controlled fashion to obtain:

$$\begin{cases} D_{n,n} & = 1 - \eta^2 \left(n + \frac{1}{2}\right) + \mathcal{O}\left(\eta^3\right) \\ D_{n,n+1} & = i\sqrt{n+1}\eta + \mathcal{O}\left(\eta^2\right) \\ D_{n,n-1} & = i\sqrt{n}\eta + \mathcal{O}\left(\eta^2\right) \end{cases} \tag{10}$$

Which recovers Eq. 7 up to order η, however also allows to extend the derivation to higher orders. Namely, the dependence of the carrier Rabi frequency on harmonic state: $\Omega_{n,n} = \Omega\left(1 - \eta^2\left(n + \frac{1}{2}\right)\right)$, such that thermometry may also be performed on the carrier transition (and not only side-band transitions as discussed above).

2.2 Mølmer-Sørensen gate

In 1999 Klaus Mølmer and Anders Sørensen proposed a method to entangle two trapped ions by using bi-chromatic drive [19]. This method, later termed as the Mølmer-Sørensen (MS) gate, entangles ions by addressing their harmonic trap degrees of freedom, regardless of their initial state (as long as they are in the Lamb-Dicke regime), which may interpreted as insensitivity to the ion's temperature (over many realizations). This was considered a substantial improvement over previous methods which required cooling to the harmonic trap ground state, such as the Cirac-Zoller gate [22]. This method was first demonstrated with a reported fidelity of $F = 0.83 \pm 0.01$ for two ions [23] and later became a standard tool for entanglement in the trapped ions community.

A year later K. Mølmer and A. Sørensen published a more comprehensive description and solution to their proposed method [20], which we will follow here as a basis to robust entanglement.

2.2.1 System Hamiltonian

Following [20], we consider a system of two ions in a harmonic trap such that the Hilbert space is composed of two effective two-level systems and two 3d harmonic oscillator degrees of freedom (one for each ion, or, preferably one 1d oscillator for each normal mode of motion in the ion crystal). Here we will use the $|S\rangle \equiv \left|5S_{\frac{1}{2},+\frac{1}{2}}\right\rangle \longrightarrow \left|4D_{\frac{5}{2},+\frac{3}{2}}\right\rangle \equiv |D\rangle$ dipole forbidden quadropole allowed optical clock transition of $^{88}Sr^{+}$ ions.

The ions are driven by a red-detuned and blue-detuned laser such that only one normal mode is resonant (and all other modes may be neglected in a RWA), therefore a sufficient description of any pure state of this system is: $|\psi\rangle = \sum_{i,j\in\{S,D\}} \sum_{n=0}^{\infty} \alpha_{i,n} |ij;n\rangle$ where by the ket we mean $|ij;n\rangle \equiv |i\rangle |j\rangle |n\rangle$ such that i, j are each one of the two level states $|S\rangle, |D\rangle$ and $|n\rangle$ is a Fock state of the harmonic oscillator. This structure is shown pictorially in Fig. 2.

The system Hamiltonian is given by:

$$\hat{H} = \hat{H}_0 + \hat{V} \tag{11}$$

Where:

$$\begin{cases} \hat{H}_0 = \nu\left(\hat{a}^\dagger\hat{a} + \frac{1}{2}\right) + \sum_i \omega_{SD}\frac{\hat{\sigma}_z^{(i)}}{2} \\ \hat{V} = \hat{V}\left(\omega_r\right) + \hat{V}\left(\omega_b\right) \\ \hat{V}\left(\omega\right) = \sum_i \frac{\hbar\Omega}{2}\left[\hat{\sigma}_+^{(i)} e^{i(k\hat{x}-\omega t+\phi)}\right] + h.c \\ \eta\left(\hat{a}^\dagger + \hat{a}\right) = k\hat{x} \end{cases} \tag{12}$$

Here ν is the harmonic trap frequency, ω_{SD} is the two level separation, $\sigma_j^{(i)}$ is the j'th Pauli operator of the i'th ion, Ω is the laser Rabi frequency, η is the Lamb-Dicke parameter, $\hat{a} = \frac{\hat{x}+i\hat{p}}{\sqrt{2}}$ is the harmonic trap annihilation operator, ω is the laser frequency and ϕ is its phase. Note that we already assumed here that the Rabi frequency and Lamb-Dicke parameter are the same for both ions.

We move to an interaction picture with respect to $\hat{H}_0$ and apply a RWA by assuming $\Omega \ll \nu$ to obtain the interaction Hamiltonian (see appendix: 6.1.1):

$$\hat{V}_I = \frac{\hbar\eta\Omega}{2}\sum_i \left[i\hat{\sigma}_+^{(i)} e^{-i\phi}\left(\hat{a}e^{-i(\delta-\xi)t} + \hat{a}^\dagger e^{-i(\delta+\xi)t}\right) + h.c\right] \tag{13}$$

Where we defined the red and blue detuned lasers:

$$\begin{cases} \omega_r = \omega_{SD} - \nu - \xi + \delta \\ \omega_b = \omega_{SD} + \nu + \xi + \delta \end{cases} \tag{14}$$

This interaction may be interpreted as follows - the drive induces an excitation of the ion internal degrees of freedom (qubit) while creating or annihilating a harmonic trap phonon, these excitations are detuned by the *symmetric detuning* ξ and the *anti-symmetric detuning* δ. This is shown pictorially in Fig. 2, which reveals the origin of the names of the two detunings - the symmetric detuning, ξ, is subtracted from the red detuned laser and added to the blue detuned such that it cancels in their sum, while the anti-symmetric detuning is a true detuning of the sum of the two frequencies the two-photon transition $|SS;n\rangle \longrightarrow |DD;n\rangle$.

As seen in Fig. 2, a single photon transition is always as associated with a change in one phonon of the harmonic trap from the initial condition. For example, when the initial qubit state is $|SS\rangle$, a transition to $|SD\rangle$ or $|DS\rangle$ requires creation or annihilation of a harmonic trap quantum (but not for a transition from $|SS\rangle$ to $|DD\rangle$). Thus, when the initial state is indeed $|SS\rangle$ we often refer to the population in $|SD\rangle$ and $|DS\rangle$ as *motion* (we show this relation directly and justify the naming below).

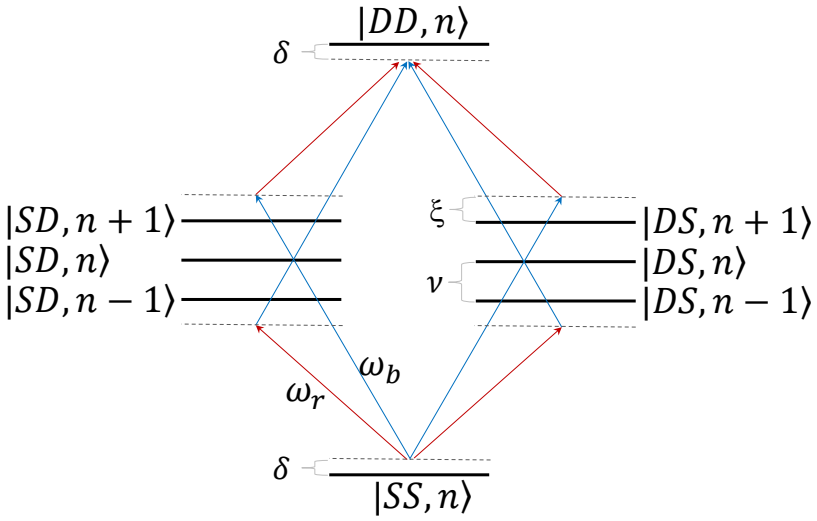

Figure 2: **Energy levels and interaction Hamiltonian of the MS gate.** The Hilbert space of two qubits in a harmonic trap is made of the four internal qubit states $|SS\rangle, |SD\rangle, |DS\rangle, |DD\rangle$ superimposed by the external harmonic ladder $|n\rangle$. The interaction Hamiltonian excites the qubit states while annihilating (ω_r, red detuned beam) or creating (ω_b, blue detuned beam) a harmonic trap phonon. The decomposition to symmetric detuning ξ and anti-symmetric detuning δ is such that there are four paths from $|SS; n\rangle$ to $|DD; n\rangle$ which are detuned by 2δ, while ξ only determines the detuning of the intermediate levels $|SD; n \pm 1\rangle$ and $|DS; n \pm 1\rangle$. The diagram is not to scale since we assume that $\omega_{r,b} \gg \nu \gg \Omega, \xi, \delta$.

2.2.2 Unitary evolution and classical analogy

We assume an on resonance drive, that is $\delta = 0$. We also assume that (wlog) $\phi = 0$ such that the interaction becomes:

$$\hat{V}_I = -\hbar\eta\Omega \sum_i \hat{\sigma}_y^{(i)} \left(\hat{a}e^{i\xi t} + \hat{a}^\dagger e^{-i\xi t}\right) \tag{15}$$

$$= -\sqrt{2}\hbar\eta\Omega\hat{J}_y \left(\cos\left(\xi t\right)\hat{x} - \sin\left(\xi t\right)\hat{p}\right) \tag{16}$$

$$\equiv f\left(t\right)\hat{J}_y x + g\left(t\right)\hat{J}_y\hat{p} \tag{17}$$

Where we defined the global spin operator:

$$\hat{J}_y = \frac{\hat{\sigma}_y^{(1)} \otimes \mathbb{1}^{(2)} + \mathbb{1}^{(1)} \otimes \hat{\sigma}_y^{(2)}}{2} \tag{18}$$

The solution is given by the unitary evolution operator (see appendix: 6.1.2):

$$\hat{U}\left(t; 0\right) = e^{-iA(t)\hat{J}_y^2} e^{-iF(t)\hat{J}_y\hat{x}} e^{-iG(t)\hat{J}_y\hat{p}} \tag{19}$$

Where we defined the time dependent functions:

$$\begin{cases} G(t) = \int_0^t d\tau g(\tau) = \frac{\sqrt{2}\eta\Omega}{\xi}\left(1-\cos(\xi t)\right) \\ F(t) = \int_0^t d\tau f(\tau) = -\frac{\sqrt{2}\eta\Omega}{\xi}\sin(\xi t) \\ A(t) = -\int_0^t d\tau F(\tau) g(\tau) = \frac{\eta^2\Omega^2}{\xi}\left(t - \frac{\sin(2\xi t)}{2\xi}\right) \end{cases} \tag{20}$$

We note that the first (right-most) term in $\hat{U}$ is a translation in position ($\hat{x}$) by a magnitude $G(t)$ multiplied by the eigenvalue of $\hat{J}_y$, similarly, the next term is a translation in momentum by a magnitude $F(t)$ multiplied by the eigenvalue of $\hat{J}_y$. These constitute *spin-dependent forces*, i.e. they generate a change in the normal mode position and momentum by a magnitude that depends on the spin state projected on the $\hat{J}_y$ direction. We note that already in the form of $\hat{V}_I$ such dynamics may be predicted since it represents the action of an off-resonance driving force acting on the oscillator, which is multiplied by the spin operator $\hat{\sigma}_y$ (as opposed, for example, for just $\hat{H}_{RSB}$ alone which conditions an excitation of a phonon on an excitation of the ion).

To appreciate this fully we note that:

$$\left\langle \hat{J}_y\hat{x} \right\rangle = \left\langle \psi(t) \left| \hat{J}_y\hat{x} \right| \psi(t) \right\rangle = \left\langle \psi(0) \left| \hat{U}^\dagger(t;0)\,\hat{J}_y\hat{x}\hat{U}(t;0) \right| \psi(0) \right\rangle \tag{21}$$

$$= \left\langle \psi(0) \left| e^{iG(t)\hat{J}_y\hat{p}}\hat{J}_y\hat{x}e^{-iG(t)\hat{J}_y\hat{p}} \right| \psi(0) \right\rangle \tag{22}$$

$$= G(t) - \left\langle \psi(0) \left| \hat{J}_y\hat{x} \right| \psi(0) \right\rangle \equiv G(t) + x_0 \tag{23}$$

Similarly one can show that:

$$\left\langle \hat{J}_y\hat{p} \right\rangle \equiv F(t) + p_0 \tag{24}$$

Therefore one can interpret $(G(t)+x_0, F(t)+p_0)$ as a curve in the $\hat{J}_y$ conditioned $(\hat{x},\hat{p})$ phase space of the harmonic trap, where (x_0,p_0) are determined by the initial conditions. By considering the explicit expressions for G, F we note they form a circle with center $\left(\frac{\sqrt{2}\eta\Omega}{\xi}+x_0, p_0\right)$ and radius $\frac{\sqrt{2}\eta\Omega}{\xi}$. For what is to come we will assume that $x_0 = p_0 = 0$.

We turn to the last term (left-most) of Eq. 19 and note that since $\hat{J}_y^2 = \frac{\mathbb{1}^{(1)}\otimes\mathbb{1}^{(2)}+\hat{\sigma}_y^{(1)}\otimes\hat{\sigma}_y^{(2)}}{2}$, then it acts as a correlated rotation in the qubit subspace. Such that: $e^{-i\theta\hat{J}_y^2}|SS\rangle = e^{-\frac{i\theta}{2}}\left(\cos\left(\frac{\theta}{2}\right)|SS\rangle + i\sin\left(\frac{\theta}{2}\right)|DD\rangle\right)$ and similarly $e^{-i\theta\hat{J}_y^2}|SD\rangle = e^{-\frac{i\theta}{2}}\left(\cos\left(\frac{\theta}{2}\right)|SD\rangle - i\sin\left(\frac{\theta}{2}\right)|DS\rangle\right)$. For the choice $\theta = \frac{\pi}{2}$ we get a rotation between the product states and the fully entangled states:

$$|SS\rangle \longrightarrow e^{-i\frac{\pi}{4}}\frac{|SS\rangle + i|DD\rangle}{\sqrt{2}}, \qquad |SD\rangle \longrightarrow e^{-i\frac{\pi}{4}}\frac{|SD\rangle - i|DS\rangle}{\sqrt{2}} \tag{25}$$

The angle θ of this correlated rotation is in fact determined by $A(t) = -\int_0^t d\tau F(\tau) g(\tau)$, that is the area enclosed by the phase space curve plotted by $(G(t), F(t))$, as shown in Fig. 3. By applying single qubit rotations before

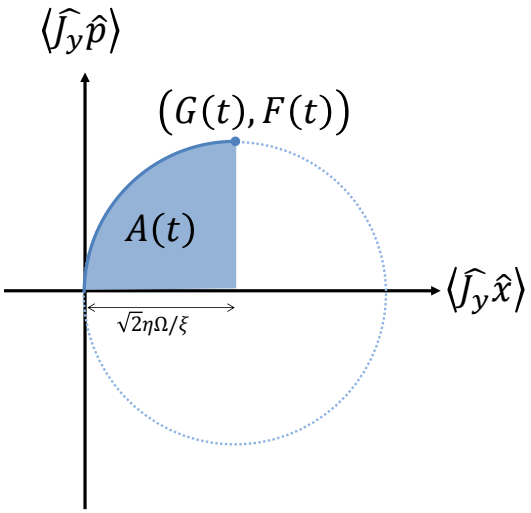

Figure 3: **Phase space picture of the MS gate.** The unitary evolution operator $\hat{U}(t;0)$ can be represented as a curve in the harmonic trap $\hat{J}_y$ conditional phase space. The trap degrees of freedom evolve according to the curve $(G(t), F(t))$ while the accumulated correlated angle evolves according to the area enclosed by this curve. By considering G, F explicitly we note that the curve forms a circle whose center is $\left(0, \frac{\sqrt{2}\eta\Omega}{\xi}\right)$ and radius its $\frac{\sqrt{2}\eta\Omega}{\xi}$.

and after this correlated rotation with $\theta = \frac{\pi}{2}$, a Controlled-NOT gate may be implemented.

To obtain an entangling gate we demand that at some time $t = T$ which we denote the *gate time* the phase space trajectory is closed and the accumulated correlated angle is $\theta = \frac{\pi}{2}$, we obtain the following solutions:

$$\begin{cases} G(T) = F(T) = 0 \\ A(T) = \frac{\pi}{2} \end{cases} \Rightarrow \begin{cases} \xi_n = 2\sqrt{n}\eta\Omega \\ T = \frac{2\pi}{\xi_n} \end{cases} \tag{26}$$

Where $n = 1, 2, 3, ...$, the shortest gate time is therefore $\xi = 2\eta\Omega$ and $T = \frac{2\pi}{\xi}$. At this time the phase space trajectory plots exactly one circle such that its area is $\frac{\pi}{2}$.

We note that the bi-chromatic driving field required for the MS interaction is of the form:

$$\begin{aligned} \Omega(t) &= \frac{\Omega_0}{2}\left[\sin\left(\left(\omega_{SD} + (\nu + \xi)\right)t\right) + \sin\left(\left(\omega_{SD} - (\nu + \xi)\right)t\right)\right] \\ &\equiv \Omega_0 \sin(\omega_{SD} t)\, E(t) \end{aligned} \tag{27}$$

Where Ω_0 is the amplitude of the driving field. That is, the drive consists of a fast carrier field $\sin(\omega_{SD} t)$ which is amplitude modulated by a slow envelope: $E(t) \equiv \cos\left(\left(\nu + \xi\right)t\right)$. As we show below, it is beneficial to defines the rotating-frame envelope $E_I(t) = E(t)|_{\nu=0}$ which in this case is simply $\cos(\xi t)$.

2.2.3 Direct carrier off-resonance coupling

In deriving Eq. 19 we used a RWA to neglect the term:

$$\hat{H}_d = 2\Omega \hat{J}_x \cos\left(\left(\nu - \xi\right) t\right) \tag{28}$$

This term creates direct carrier off-resonance coupling (i.e. a transition between $|S\rangle$ and $|D\rangle$ without exciting the normal mode). In order to keep this term negligible (and justify the RWA) we impose the restriction: $\Omega \ll \nu$. This enforces a physical lower bound on the gate time: $T = \frac{\pi}{\eta\Omega} \gg \frac{1}{\nu}$.

To obtain a more accurate estimation of this term's effect, we change to an interaction picture with respect to the unitary interaction operator $\hat{U}\left(t;0\right)$ and calculate the remaining evolution by constructing a Dyson series:

$$\begin{cases} \hat{H}_{d,I}\left(t\right) = U^{\dagger}\left(t\right)\hat{H}_d\left(t\right)\hat{U}\left(t\right) \\ \hat{U}_I\left(t;0\right) = \mathbb{1} - i\int_0^t dt_1 \hat{H}_{d,I}\left(t_1\right) - \int_0^t dt_1 \int_0^{t_1} dt_2 \hat{H}_{d,I}\left(t_1\right)\hat{H}_{d,I}\left(t_2\right) + ... + \left(-i\right)^n \int_0^t dt_1 \cdots \int_0^{t_{n-1}} dt_n \hat{H}_{d,I}\left(t_1\right)\cdots\hat{H}_{d,I}\left(t_n\right) \end{cases} \tag{29}$$

$\hat{H}_d$ is fast oscillating, thus may treat $\hat{U}\left(t\right)$ as a constant during the integration. Near the gate time we set $\hat{U}\left(t\right) = e^{i\frac{\pi}{2}\hat{J}_y^2}$ and obtain:

$$\hat{U}_I\left(t\right) \approx \mathbb{1} - 2i\left(\frac{\Omega}{\nu-\xi}\right)\sin\left(\left(\nu-\xi\right)t\right)U^{\dagger}\hat{J}_x\hat{U} - 2\left(\frac{\Omega}{\nu-\xi}\sin\left(\left(\nu-\xi\right)t\right)\right)^2 U^{\dagger}\hat{J}_x^2\hat{U} + \mathcal{O}\left(\left(\frac{\Omega}{\nu-\xi}\right)^3\right) \tag{30}$$

By retaining only leading order contributions in $\frac{\Omega}{\nu-\xi}$ we can calculate the resulting infidelity by considering the initial state $|\psi\left(0\right)\rangle = |SS\rangle$. The evolution is then given by:

$$|\psi_I\left(t\right)\rangle = \hat{U}_I\left(t\right)|\psi_I\left(0\right)\rangle = \hat{U}_I\left(t\right)\hat{U}^{\dagger}|\psi\left(0\right)\rangle = \hat{U}_I\left(t\right)\frac{|SS\rangle + i\,|DD\rangle}{\sqrt{2}} \tag{31}$$

$$= \frac{|SS\rangle + i\,|DD\rangle}{\sqrt{2}} - e^{i\frac{\pi}{4}}\left(\frac{\Omega}{\nu-\xi}\sin\left(\left(\nu-\xi\right)t\right)\right)^2\left(|SS\rangle + |DD\rangle\right) \tag{32}$$

$$+ i\left(\frac{\Omega}{\nu-\xi}\right)\sin\left(\left(\nu-\xi\right)t\right)e^{-i\frac{\pi}{4}}\left(|SD\rangle + |DS\rangle\right) \tag{33}$$

The direct carrier infidelity is therefore given by:

$$1 - F_d = 1 - |\langle\psi_{\text{target}}|\psi\left(t\right)\rangle| = 1 - |\langle\psi_I\left(0\right)|\psi_I\left(t\right)\rangle| \tag{34}$$

$$\approx \frac{1}{2}\left(\frac{\Omega}{\nu-\xi}\right)^2\left(1 - \cos\left(2\left(\nu-\xi\right)t\right)\right) + \mathcal{O}\left(\left(\frac{\Omega}{\nu-\xi}\right)^2\right) \tag{35}$$

We note the infidelity oscillates due to this carrier coupling. It is minimized by allowing additional control over

the trap frequency, such that the gate ends exactly when the infidelity vanishes:

$$\begin{cases} \frac{(\eta\Omega)^2}{\xi}t = \frac{\pi}{2} \\ \xi t = 2\pi n \\ (\nu - \xi)\, t = 2\pi m \end{cases} \Rightarrow \begin{cases} \xi_0 = 2\sqrt{n}\eta\Omega \\ \nu_0 = \frac{2n+m}{\sqrt{n}}\eta\Omega \\ t_0 = \frac{\pi\sqrt{n}}{\eta\Omega} \end{cases} \tag{36}$$

Where $n, m \in \mathbb{Z}$, and typically $m \gg n$. However ν is in general difficult to stabilize with the required resolution of $\eta\Omega$ therefore in the worst case we obtain the consistent scaling:$1 - F_d \approx \left(\frac{\Omega}{\nu}\right)^2$.

2.3 Evolution in the qubit subspace (tracing out motion)

In their work, K. Mølmer and A. Sørensen provide a solution for the qubit degrees of freedom which is obtained by tracing out the trap degrees of freedom [20].

Here, we first calculate the Kraus operators related the unitary evolution operator (and obtain a similar result to that of [20]). Then we assume an initial thermal state and derive an analytic expression for the evolution of the two-qubit subspace density matrix. Alternatively, these results may be derived using displacement operators formalism as described in [13]. The qubit evolution allows for a complete analytic expression of the evolution of populations, coherences, fidelities etc.

2.3.1 Kraus decomposition

We are interested in tracing out the trap degrees of freedom and acquiring an evolution for the qubit subspace. The system Hilbert space is composed of the two-qubit sub-space degrees of freedom and motional degrees of freedom which we denote by $\mathcal{H} = \mathcal{H}_q \otimes \mathcal{H}_h$. The evolution in two-qubits sub-space is then given by Kraus decomposition, which is obtained by tracing out motion [24]:

$$\hat{\rho}_q(t) = \mathrm{Tr}_h\left(\hat{\rho}(t)\right) = \sum_{n,m} \hat{K}_{m,n}(t)\, \hat{\rho}_q(0)\, \hat{K}^\dagger_{m,n}(t) \tag{37}$$

Where $\hat{\rho}(t)$ and $\hat{\rho}_q(t)$ are the full system and two-qubit density matrices respectively. When the initial state is unentangled, that is, $\hat{\rho}(0) = \hat{\rho}_q(0) \otimes \hat{\rho}_h(0)$, then the $\hat{K}_{m,n}(t)$'s are Kraus operators given by (see appendix: 6.2.1):

$$\hat{K}_{i,j}(t) = \sqrt{\lambda_j}\left\langle \psi^h_j \middle| \hat{U}(t;0) \middle| \psi^h_i \right\rangle \tag{38}$$

Where $\hat{\rho}_h(0) = \sum_i \lambda_i \left|\psi^h_i\right\rangle \left\langle\psi^h_i\right|$. That is, they are determined by the harmonic oscillator initial state and the unitary evolution operator.

In our case, assuming that the $\hat{\rho}_h(0) = \sum_n \lambda_n |n\rangle\langle n|$ leads to the expression (see appendix: 6.2.2):

$$\left\langle n\left|\hat{U}\right|n'\right\rangle = (-1)^{n_>}\sqrt{\frac{n_<!}{n_>!}}e^{-\left(iA(t)+\frac{F^2(t)+G^2(t)}{4}+\frac{iF(t)G(t)}{2}\right)}\hat{J}_y^{n+n'}\left(\frac{G(t)+iF(t)}{\sqrt{2}}\right)^{n_>-n_<}L_{n_<}^{n_>-n_<}\left(\frac{F^2(t)+G^2(t)}{2}\right) \tag{39}$$

$$+\delta_{n,n'}\frac{\mathbb{1}\otimes\mathbb{1}-\sigma_y\otimes\sigma_y}{2} \tag{40}$$

Where L_n^α is an α generalized order n Laguerre polynomial, and $n_< = \max\{n, n'\}$. The evolution operator is obtained by decomposing the harmonic oscillator initial state (which is diagonal in the $\{|n\rangle\}$ basis) and summing over the Kraus operators.

2.3.2 Evolution of density matrix

For an initial thermal distribution of the harmonic oscillator, characterized by the average occupation number $\bar{n}$:

$$\hat{\rho}_h(0) = \frac{1}{\bar{n}+1}\sum_{n=0}^{\infty}\left(\frac{\bar{n}}{\bar{n}+1}\right)^n |n\rangle\langle n|, \tag{41}$$

we perform the above summation and obtain a closed form analytical expression for the two-qubit subspace density matrix (see appendix: 6.2.3):

$$\hat{\rho}_q(t) = \hat{\rho}_q(0) + \frac{\hat{J}_y^2\hat{\rho}_q(0)\hat{J}_y^2}{2}\left(e^{-2(2\bar{n}+1)\frac{F^2(t)+G^2(t)}{2}}-1\right) \tag{42}$$

$$-\frac{\hat{J}_y\hat{\rho}_q(0)\hat{J}_y}{2}\left(e^{-2(2\bar{n}+1)\frac{F^2(t)+G^2(t)}{2}}-1\right) \tag{43}$$

$$+\hat{J}_y^2\hat{\rho}_q(0)\frac{\mathbb{1}\otimes\mathbb{1}-\sigma_y\otimes\sigma_y}{2}\left(e^{-\left(\bar{n}+\frac{1}{2}\right)\frac{F^2(t)+G^2(t)}{2}-i\left(A(t)+\frac{F(t)G(t)}{2}\right)}-1\right) \tag{44}$$

$$+\frac{\mathbb{1}\otimes\mathbb{1}-\sigma_y\otimes\sigma_y}{2}\hat{\rho}_q(0)\hat{J}_y^2\left(e^{-\left(\bar{n}+\frac{1}{2}\right)\frac{F^2(t)+G^2(t)}{2}+i\left(A(t)+\frac{F(t)G(t)}{2}\right)}-1\right) \tag{45}$$

For the initial qubit state $\hat{\rho}_q(0) = |SS\rangle\langle SS|$ the population dynamics is then given by:

$$\begin{cases} Pr(SS) = \frac{3+e^{-4\left(\bar{n}+\frac{1}{2}\right)\frac{F^2+G^2}{2}}+4e^{-\left(\bar{n}+\frac{1}{2}\right)\frac{F^2+G^2}{2}}\cos\left(A+\frac{FG}{2}\right)}{8} \\ Pr(DD) = \frac{3+e^{-4\left(\bar{n}+\frac{1}{2}\right)\frac{F^2+G^2}{2}}-4e^{-\left(\bar{n}+\frac{1}{2}\right)\frac{F^2+G^2}{2}}\cos\left(A+\frac{FG}{2}\right)}{8} \\ Pr(SD) = \frac{1-e^{-4\left(\bar{n}+\frac{1}{2}\right)\frac{F^2+G^2}{2}}}{8} \\ Pr(DS) = \frac{1-e^{-4\left(\bar{n}+\frac{1}{2}\right)\frac{F^2+G^2}{2}}}{8} \end{cases} \tag{46}$$

As mentioned above, when the initial state is $|SS\rangle$ we refer to the populations of $|SD\rangle$ and $|DS\rangle$ as motion, here the reason becomes even more apparent as the populations of these levels depends directly on $R^2 \equiv F^2 + G^2$,

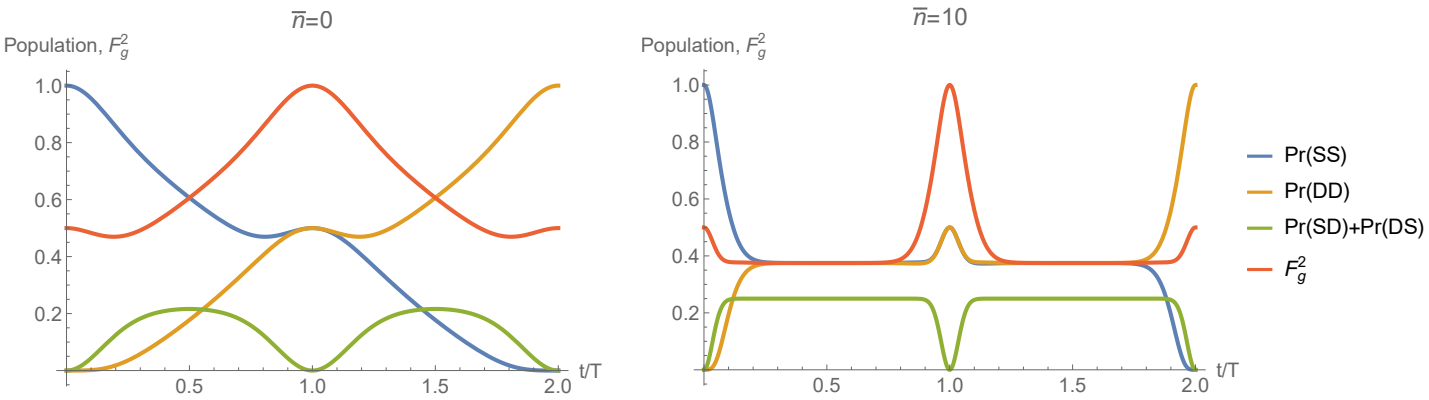

Figure 4: **Population and fidelity evolution of the MS gate.** In both plots the symmetric detuning is $\xi = 2\eta\Omega$. such that at $t = T$, after a single oscillation of the motion (green), an entangling gate is achieved, as seen by the crossing of the SS population (blue) and DD population (orange) at 0.5. At this point the Fidelity (red) reaches 1. The "cold" gate at $\bar{n} = 0$ (left) easily demonstrates the evolution of the different populations and corresponds well with the phase space picture. While the "hot" gate at $\bar{n} = 10$ (right) has flat part in which "nothing" seems to happen and then a steep approach to the qubit entanglement, as seen by the narrow feature of the fidelity function.

which measures the phase space trajectory distance from the initial position.

The fidelity for the transition $|\psi_{\text{initial}}\rangle = |SS\rangle \rightarrow |\psi_{\text{final}}\rangle = \frac{|SS\rangle + i|DD\rangle}{\sqrt{2}}$ is given by:

$$F_g^2 = \text{Tr}\left(\hat{\rho}_q \left|\psi_{\text{final}}\right\rangle \left\langle\psi_{\text{final}}\right|\right) \tag{47}$$

$$= \frac{1}{2}\left(\hat{\rho}_{SS,SS} + \hat{\rho}_{DD,DD} - 2\Im\left[\hat{\rho}_{SS,DD}\right]\right) \tag{48}$$

$$= \frac{3 + e^{-4\left(\bar{n}+\frac{1}{2}\right)\frac{F^2+G^2}{2}}}{8} + \frac{1}{2}\sin\left(A + \frac{FG}{2}\right) e^{-\frac{F^2+G^2}{2}\left(\bar{n}+\frac{1}{2}\right)} \tag{49}$$

As expected, $F_g = 1$ if an only if $F^2 + G^2 = 0$ and $\sin(A) = 1$.

We also use the state purity as a measure of disentanglement from motion:

$$F_p(t) = \text{Tr}\left(\hat{\rho}_q^2\right) = \frac{3 + 4e^{-\left(\bar{n}+\frac{1}{2}\right)\left(F^2+G^2\right)} + e^{-4\left(\bar{n}+\frac{1}{2}\right)\left(F^2+G^2\right)}}{8} \tag{50}$$

Which only depends on G and F since only coupling to the trap degrees of freedom may result in a mixed state.

The time evolution and fidelity of the gate for the initial state $\hat{\rho}(0) = |SS\rangle\langle SS| \otimes \hat{\rho}_{h,\bar{n}}$ may now be easily plotted, where by $\hat{\rho}_{h,\bar{n}}$ we mean a thermal state of the harmonic trap with an average occupation number $\bar{n} \geq 0$. These are shown in Fig. 4.

2.4 Composite entangling gate

We generalize the MS gate by adding more driving fields. We show that in order to retain the properties of an entangling gate we must use harmonics of the original drive frequency, nevertheless we have more degrees of freedom, namely the driving amplitudes, which we may employ to optimize different aspects of the gate.

2.4.1 Adding driving fields

We propose a *composite gate* by driving with N red and blue detuned frequency pairs. The Hamiltonian now reads:

$$\hat{H} = \hat{H}_0 + \sum_{i=1}^{N} r_i \left[\hat{V}\left(\omega_{r,i}\right) + \hat{V}\left(\omega_{b,i}\right)\right] \tag{51}$$

Where r_i are the relative amplitudes of the frequency pair $\omega_{r_i}, \omega_{b_i}$, and:

$$\begin{cases} \hat{H}_0 = \nu\left(\hat{a}^\dagger\hat{a} + \frac{1}{2}\right) + \sum_i \omega_{eg}\frac{\hat{\sigma}_z^{(i)}}{2} \\ \hat{V}\left(\omega_i\right) = \sum_i \frac{\hbar\Omega}{2}\left[\hat{\sigma}_+^{(i)} e^{i(k\hat{x} - \omega_i t - \phi_i)}\right] + h.c \\ \eta\left(\hat{a}^\dagger + \hat{a}\right) = k\hat{x} \end{cases} \tag{52}$$

In addition we now allow each frequency a different phase, such that we have for each frequency pair:

$$\omega_{(b,r),i} = \omega_{eg} \pm \left(\nu + \xi_i\right) + \delta_i \tag{53}$$

Where the $\pm$ are the blue and red detuned respectively with phases $\phi_{r,i}, \phi_{b,i}$, and ξ_i and δ_i are the symmetric and anti-symmetric detuning of each pair. Similar to the original derivation we change to the interaction picture, assume $\eta \ll 1$, and make use of a rotating wave approximation by assuming $\frac{\Omega}{\nu} \ll 1$ to obtain:

$$r_i\left[\hat{V}_I\left(\omega_{r,i}\right) + \hat{V}_I\left(\omega_{b,i}\right)\right] = \frac{r_i\hbar\eta\Omega}{2}\sum_i \left(ie^{-i\delta_i}e^{-i\frac{\phi_{r,i}+\phi_{b,i}}{2}}\hat{\sigma}_+^{(i)} + h.c\right)\left(e^{i\xi_i t}e^{-i\frac{\phi_{r,i}-\phi_{b,i}}{2}}\hat{a} + h.c\right) + \mathcal{O}\left(\eta^2, \frac{\nu}{\Omega}\right) \tag{54}$$

In order to obtain a Hamiltonian similar in form to that of the MS gate we must impose the condition $\forall i \quad \phi_{r,i} = -\phi_{b,i}$ such that all rotations in the two-qubit subspace are around the $\hat{y}$ axis. This allows us to redefine a single phase for each pair of the form: $\phi_i = \frac{\phi_r - \phi_b}{2}$.

Furthermore, we assume an on-resonance drive ($\forall i \quad \delta_i = 0$), and obtain the interaction Hamiltonian:

$$\hat{V}_I^{RWA} = -\sqrt{2}\hbar\eta\Omega\hat{J}_y\sum_i r_i\left(\cos\left(\xi_i t - \phi_i\right)\hat{x} - \sin\left(\xi_i t - \phi_i\right)\hat{p}\right) \tag{55}$$

Thus, each pair has three degrees of freedom: frequency, relative amplitude and phase: ξ_i, r_i, ϕ_i.

We note that the Hamiltonian still abides the MS form:

$$\hat{V}_I = f\left(t\right)\hat{J}_y x + g\left(t\right)\hat{J}_y\hat{p} \tag{56}$$

Thus, the unitary evolution operator solution is unchanged (see appendix: 6.1.2):

$$\begin{cases} \hat{U}\left(t,0;\xi,\delta=0\right)=e^{-iA(t)\hat{J}_y^2}e^{-iF(t)\hat{J}_y\hat{x}}e^{-iG(t)\hat{J}_y\hat{p}} \\ F\left(t\right)=\int\limits_0^t d\tau f\left(\tau\right)=\sqrt{2}\eta\Omega\sum_{i=1}^N\frac{r_i}{\xi_i}\left(\sin\left(\phi_i\right)-\sin\left(\xi_i t+\phi_i\right)\right) \\ G\left(t\right)=\int\limits_0^t d\tau g\left(\tau\right)=\sqrt{2}\eta\Omega\sum_{i=1}^N\frac{r_i}{\xi_i}\left(\cos\left(\phi_i\right)-\cos\left(\xi_i t+\phi_i\right)\right) \\ A\left(t\right)=-\int\limits_0^t d\tau F\left(\tau\right)g\left(\tau\right) \end{cases} \tag{57}$$

Since the previous sub-section is written only in terms of F, G, A the qubit evolution and fidelity obtained above are unchanged.

We note that the driving field can still be viewed as an amplitude modulation, taking the form:

$$\Omega\left(t\right)=\frac{\Omega_0}{2}\sum_{i=1}^N r_i\left[\sin\left(\left(\omega_{SD}+\left(\nu+\xi_i\right)\right)t\right)+\sin\left(\left(\omega_{SD}-\left(\nu+\xi_i\right)\right)t\right)\right]=\Omega_0\sin\left(\omega_{SD}t\right)E\left(t\right) \tag{58}$$

Such that rotating picture envelope is: $E_I\left(t\right)=\sum\limits_{i=1}^N\cos\left(\xi_i t\right)$.

2.4.2 Harmonic gate and robustness

To obtain an entangling gate we again demand a gate time T in which the motion vanishes (or returns to the initial conditions) and the accumulated correlated phase is $\frac{\pi}{2}$. The first condition reads:

$$R^2\left(T\right)\equiv F^2\left(T\right)+G^2\left(T\right)=0 \tag{59}$$

We note that this is trivially solved by the setting: $\forall i,\quad \xi_i T=2\pi n$. Therefore we define: $\xi_i=\xi_0 n_i$ where $\xi T=2\pi$, thus we reduced our continuous degree of freedom ξ_i to a discrete one n_i, such that all the driving components are harmonics of a fundamental frequency ξ_0, we term this is a *harmonic gate*.

The second condition reads:

$$\frac{\pi}{2}=A\left(T\right)=\frac{\eta^2\Omega^2T^2}{2\pi}\sum_{i=1}^N\frac{r_i^2}{n_i}\Rightarrow\sum_{i=1}^N\frac{r_i^2}{n_i}=1 \tag{60}$$

Where we used $T=\frac{2\pi}{\xi_0}=\frac{\pi}{\eta\Omega}$. This constitutes another constraint for the gate. Thus, a harmonic gate is a set of drive components: $\left\{\left(n_i,r_i,\phi_i\right)\right\}_{i=1}^N$ such that $\sum\limits_{i=1}^N\frac{r_i^2}{n_i}=1$, where $n_i\in\mathbb{Z}$ and $r_i\geq 0$.

Therefore, the harmonic gate has N amplitudes degrees of freedom, where one degree of freedom is used to ensure the desired correlated angle. The remaining $N-1$ degrees of freedom may be employed to optimize the desired properties of the gate. Fig. 5, shows the phase space interpretation of these degrees of freedom. For increasing n_i (left figure) the radius of motion decreases since it is determined by $\frac{r_i}{\xi_0 n_i}$ and the angular velocity is increased, since it is determined by $n_i\xi_0$, such that a larger portion of the circle is traversed. While for increasing only r_i (right

figure), only the radius increases while the angular velocity is unchanged. Changing the angle ϕ_i (middle figure) changes the orientation of the plotted circle with respect to the conditioned phase axes.

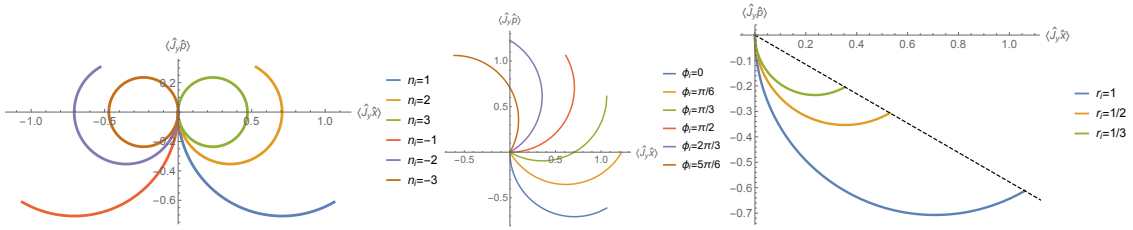

Figure 5: **Effect of the different degrees of freedom.** All plots show phase space trajectories of a single component gate while varying one of the degrees of freedom. The resulting phase space trajectory is shown from $t = 0$ to $t = \frac{T}{3}$. **Left:** When increasing the harmonic, n_i, the radius of motion decreases while angular velocity increases, choosing a negative driving frequency flips the motion around the $\left\langle \hat{J}_y\hat{p} \right\rangle$ axis. **Middle:** Scanning the phase, ϕ_i, rotates the orientation of the trajectory with respect to the phase space axes. **Right:** Increasing the relative amplitude, r_i, the radius increases whilst keeping the angular velocity constant.

When several harmonics are combined the motion is superimposed such that a variety of shapes may be plotted in phase space, covering a range of trajectories which is much broader than circles. Some examples for the various shapes are shown in Fig. 6.

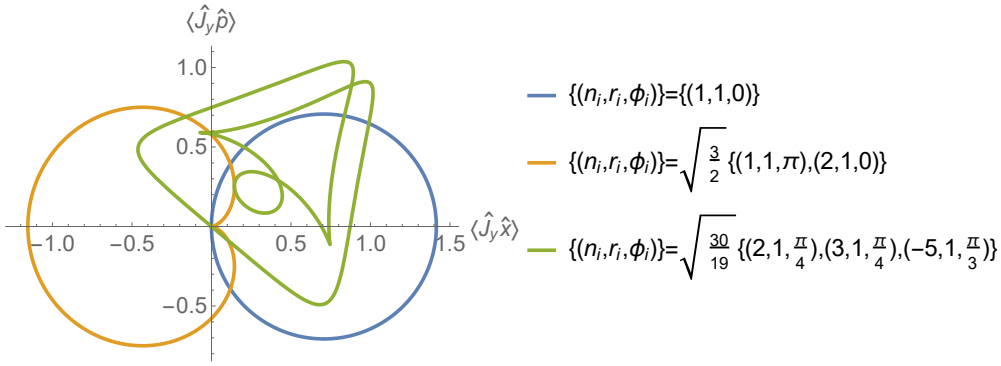

Figure 6: **Examples for phase space trajectories of harmonic gates.** For each of these three examples the drive parameters are specified as $\{(n_i, r_i, \phi_i)\}_{i=1}^{N}$ where N is the number of components and each component is characterized by harmonic numbers, amplitudes and phases respectably. The MS gate (blue) is generated by a single harmonic components. Non-trivial trajectories are easily formed, nevertheless all three are valid entangling schemes.

To increase the gate robustness to an error in one of the gate parameters α, where $\alpha = \alpha_0 + \delta\alpha$ may be any relevant parameter such as: $t, \xi, \nu, ...$ with its "correct" value α_0, we expand the gate fidelity with respect to α around the maximum:

$$F_g^2\left(\alpha; \{(n_i, r_i, \phi_i)\}_{i=1}^{N}\right) = 1 + \frac{1}{2}\frac{\partial^2 F_g^2\left(\alpha; \{(n_i, r_i, \phi_i)\}_{i=1}^{N}\right)}{\partial\alpha^2}|_{\alpha=\alpha_0}(\delta\alpha)^2 + ... \tag{61}$$

If this second order derivative (and similarly higher order derivatives) is some non-trivial function of the degrees of freedom $\{(n_i, r_i, \phi_i)\}_{i=1}^{N}$, these degrees of freedom can be chosen such that it may be diminished or eliminated. Then robustness to errors in this parameter may be accomplished. This would result in a more "flat" or "robust" response of the gate fidelity to errors in α.

The fidelity function F_g may be written in terms of the phase space functions G, F, A, therefore robustness may be achieved by eliminating derivatives of these functions.

2.5 Optimizing robustness to gate timing-errors

We derive the conditions on the gate parameters in order to increase the robustness to gate timing-errors of the form $t = T + \delta t$. To this end, it is enough to demand $\frac{\partial^n F(t)}{\partial t^n}|_{t=T} = \frac{\partial^n G(t)}{\partial t^n}|_{t=T} = 0$ for $n = 0, 1, 2, ...$ This is since the derivative of $A(t)$ has the form:

$$\frac{\partial^n A(t)}{\partial t^n} = \frac{\partial^{n-1}}{\partial t^{n-1}}\left(F(t)\frac{\partial G(t)}{\partial t}\right) = \sum_{k=1}^{n-1}\binom{n-1}{k}\frac{\partial^{n-1-k}}{\partial t^{n-1-k}}F(t)\frac{\partial^{k+1}}{\partial t^{k+1}}G(t) \tag{62}$$

We note that for $k = 1, 2, 3, ...$ we have :

$$\begin{cases} \frac{\partial^{2k-1}G(t)}{\partial t^{2k-1}}|_{t=T} = -(-1)^k \frac{\sqrt{2}\eta\Omega}{\xi_0}\sum_{i=1}^{N}\frac{r_i}{n_i}(n_i\xi_0)^{2k-1}\sin(\phi_i) \\ \frac{\partial^{2k}G(t)}{\partial t^{2k}}|_{t=T} = -(-1)^k \frac{\sqrt{2}\eta\Omega}{\xi_0}\sum_{i=1}^{N}\frac{r_i}{n_i}(n_i\xi_0)^{2k}\cos(\phi_i) \\ \frac{\partial^{2k-1}F(t)}{\partial t^{2k-1}}|_{t=T} = (-1)^k \frac{\sqrt{2}\eta\Omega}{\xi_0}\sum_{i=1}^{N}\frac{r_i}{n_i}(n_i\xi_0)^{2k-1}\cos(\phi_i) \\ \frac{\partial^{2k}F(t)}{\partial t^{2k}}|_{t=T} = (-1)^k \frac{\sqrt{2}\eta\Omega}{\xi_0}\sum_{i=1}^{N}\frac{r_i}{n_i}(n_i\xi_0)^{2k}\sin(\phi_i) \end{cases} \tag{63}$$

By setting $\tilde{r}_i = r_i e^{i\phi_i}$ we can rewrite these in terms of the order $N-1$ Vandermonde matrix:

$$N_{\{n_1,..,n_N\}} = \begin{pmatrix} 1 & 1 & 1 & \cdots & 1 \\ n_1 & n_2 & n_3 & \cdots & n_N \\ n_1^2 & n_2^2 & n_3^2 & \cdots & n_N^2 \\ \vdots & \vdots & \vdots & \ddots & \vdots \\ n_1^{N-1} & n_2^{N-1} & n_3^{N-1} & \cdots & n_N^{N-1} \end{pmatrix} \tag{64}$$

Such that:

$$N_{\{n_1,..,n_N\}}\tilde{\boldsymbol{r}} = \mathbf{0} \tag{65}$$

That is, we are looking for the kernel of the order $N-1$ Vandermonde matrix (which is of dimension 1). This is simply given by the unique solution:

$$\tilde{r_j} = \prod_{j\neq k=1}\frac{1}{n_j - n_k} \tag{66}$$

Therefore we conclude that without loss of generality $\boldsymbol{r}$ is real and is proportional to $\tilde{\boldsymbol{r}}$. In terms of our degrees of freedom, this result can be seen by setting $\phi_i \in \{0, \pi\}$ such that:

$$\begin{cases} \frac{\partial^{2k-1} G(t)}{\partial t^{2k-1}}|_{t=T} = 0 \\ \frac{\partial^{2k} F(t)}{\partial t^{2k}}|_{t=T} = 0 \end{cases}, \quad \begin{cases} \frac{\partial^{2k} G(t)}{\partial t^{2k}}|_{t=T} = -(-1)^k \frac{\sqrt{2}\eta\Omega}{\xi_0} \sum_{i=1}^{N} \frac{r_i}{n_i} (n_i \xi_0)^{2k} \cos(\phi_i) \\ \frac{\partial^{2k-1} F(t)}{\partial t^{2k-1}}|_{t=T} = (-1)^k \frac{\sqrt{2}\eta\Omega}{\xi_0} \sum_{i=1}^{N} \frac{r_i}{n_i} (n_i \xi_0)^{2k-1} \cos(\phi_i) \end{cases} \tag{67}$$

It is also beneficial to define $\phi_i = 0$ and in exchange allow: $r_i \in \mathbb{R}$. Finally, robustness is obtained by incorporating the normalization condition $\sum_{i=1}^{N} \frac{r_i^2}{n_i} = 1$. We obtain the solution:

$$r_j = \frac{1}{\sqrt{K}} \prod_{j \neq k=1}^{N} \frac{1}{n_j - n_k}, \quad K = \sum_{j=1}^{N} \frac{\tilde{r_j}^2}{n_j} \tag{68}$$

To complete the picture we note in terms of the the rotating frame drive envelope, this solution is equivalent to simply demanding that $E_I^{(n)}(t=0) = 0$ for $n = 0, 1, ..., N-1$. That is, order $N-1$ gate timing-error robustness is achieved by driving the ions with an order $N-1$ smooth driving force in the frame rotating with the harmonic trap.

2.5.1 Cardioid & Antioid - 2 driving components

A simple example of such an optimization is by using just two driving components, $N = 2$. We obtain the following:

$$\tilde{r_1} = \frac{1}{n_1 - n_2}, \qquad \tilde{r}_2 = \frac{1}{n_2 - n_1} \tag{69}$$

Thus:

$$r_1 = \sqrt{\frac{n_1 n_2}{n_1 + n_2}}, \quad r_2 = -r_1 \tag{70}$$

When choosing $n_1 = 1$ and $n_2 = 2$ then the phase space trajectory plotted by this scheme generates a heart shaped curve which is called a *Cardioid*. This curve, originally discovered by Giovanni Francesco di Castiglione in 1741, appears in nature in numerous examples such as the main lobe of the Mandelbrot set or the caustics of a light ray hitting a round cup, shown in Fig. 7. most commonly it may be generated by tracing a point on the perimeter of a circle that is rolling around a fixed circle of the same radius.

Due to this similarity we denote this driving scheme as Cardioid (n_1, n_2), such that di Castiglione's Cardioid is generated by using the Cardioid $(1, 2)$ scheme.

We note that by choosing $r_1 = r_2 = \sqrt{\frac{n_1 n_2}{n_1 + n_2}}$ we maximize the leading order contribution such that we "anti-optimize", thus we call this scheme an Antioid (n_1, n_2), since it is similar to the Cardioid (n_1, n_2) in form and

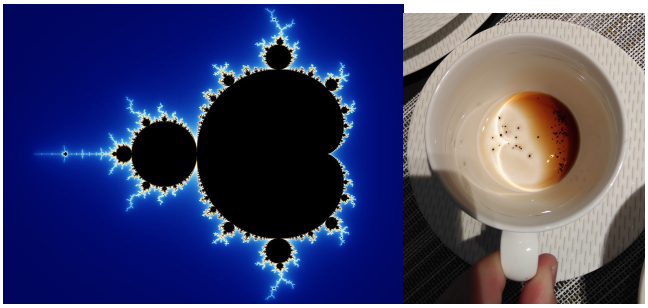

Figure 7: **Cardioids in nature. Left:** The main lobe of the Mandelbrot set is a Cardioid (adapted from Wikipedia:Mandelbrot set). **Right:** Cardioid formed by caustics on the bottom of a sad and empty coffee cup (image taken by author).

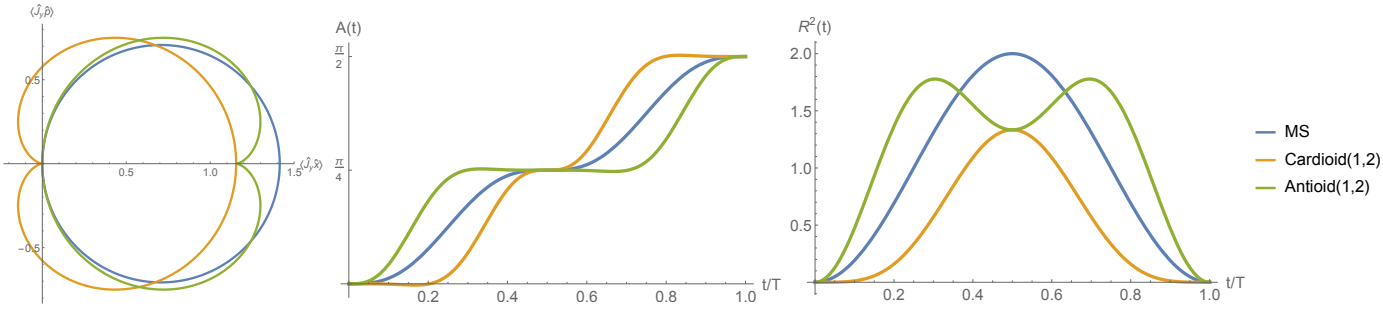

Figure 8: **Phase space of basic gate scheme.** For all plots we compare the MS gate (blue), Cardiod $(1,2)$ (orange) and Antioid $(1,2)$ (green). **Left:** Phase space trajectory from $t=0$ to $t=T$. The MS gate has a circle shaped trajectory while Cardioid $(1,2)$ and Antioid $(1,2)$ both plot a heart shaped trajectory which are flipped one with respect to the other. **Middle:** Accumulated correlated rotation angle evolution, the Cardioid $(1,2)$ has a flat response around $t=T$ while Antioid $(1,2)$ is much steeper at $t=T$. **Right:** Motion, R^2, generated of drives. Cardioid $(1,2)$ approaches $R^2=0$ with a flat $\sim\left(\frac{\delta t}{T}\right)^4$ response as opposed to Antioid$(1,2)$ or MS which are quadratic.

trajectory yet does the exact opposite in terms of robustness. The phase space trajectories, phase accumulation and motion of these drives are shown in Fig. 8.

We note that the phase accumulation of Cardioid $(1,2)$ drive leads to a flat response around the gate time $t=T$. Furthermore, we note that the motion is also flatter around the gate time. The Antioid $(1,2)$ does exactly the opposite, that is, it approaches the gate time sharply both in phase accumulation and motion. Thus the penalty to fidelity caused by a small gate timing-error $t=T+\delta t$ will be suppressed by using a Cardioid $(1,2)$ drive and increased by Antioid $(1,2)$. This robustness cannot be explained by additional power used to drive the gate since Cardioid and Antioid use the exact same power and differ only by phases, this is a coherent effect!

We can also gain intuition about the different schemes by considering their time evolution, as shown in Fig. 9, where we observe the flatness of the populations of Cardioid $(1,2)$ around the gate time $t=T$ at cold ($\bar{n}=0$) or hot ($\bar{n}=10$) conditions. The dependence of the fidelity function on $\bar{n}$ immediately implies that errors due to deviation of $F(T)$ and $G(T)$ from 0 are exponentially amplified by $\bar{n}$, thus the fidelity will have a steeper behavior for high $\bar{n}$ gates as is clearly seen in the figure.

All these properties are best summarized by simply considering the fidelity function (which is what we initially

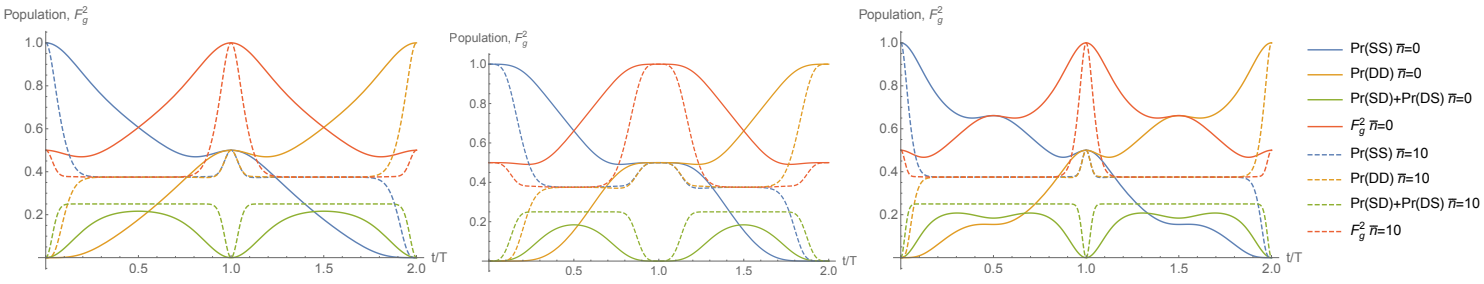

Figure 9: **Evolution and fidelity of basic gate schemes.** MS gate (left), Cardioid $(1,2)$ (middle) and Antioid $(1,2)$ (right). Notably, for Cardioid $(1,2)$ the fidelity and gate evolution has the flattest features around gate time. In addition, errors are considerably more penalized for high temperature, $\bar{n}=10$ (dashed) with respect to ground state $\bar{n}=0$ (solid).

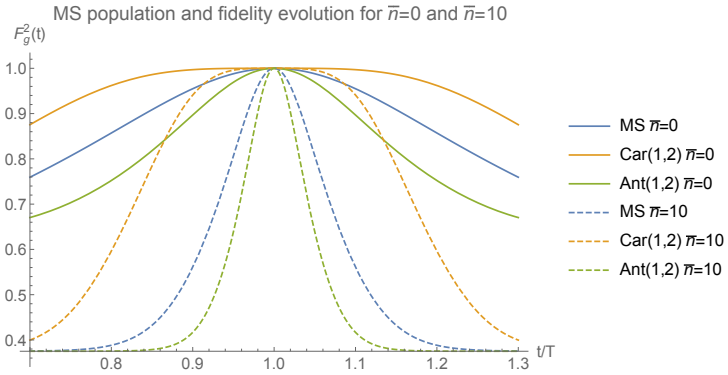

Figure 10: **Fidelity of different schemes for $\bar{n}=0$ and $\bar{n}=10$.** Notably, the Cardioid $(1,2)$ scheme (orange) is preferable for both the ground state, $\bar{n}=0$ (solid) and hot state, $\bar{n}=10$ (dashed) and scales as δt^4. While both MS (blue) and Antioid $(1,2)$ (green) scale as δt^2.

optimized) as shown in Fig. 10. Indeed, around the gate time, the Cardioid has the flattest response, which is by construction $F^2_{g,\mathrm{Car}}(T+\delta t) = 1 + \frac{1}{4!}\frac{\partial^4 F^2_{g,\mathrm{Car}}}{\partial \delta t^4}|_{\delta t=0}\delta t^4 + \mathcal{O}\left(\delta t^6\right)$. While for Antioid or MS the response is $F^2_{g,\mathrm{MS\backslash Ant}}(T+\delta t) = 1 + \frac{1}{2}\frac{\partial^2 F^2_{g,\mathrm{MS\backslash Ant}}}{\partial \delta t^2}|_{\delta t=0}\delta t^2 + \mathcal{O}\left(\delta^4\right)$.

We note that so far there are no restrictions whatsoever on n_1, n_2. While they are indeed degrees of freedom they have decoupled from the optimization problem in the sense that they cannot be used to eliminate increasing orders of δt. However the leading order is indeed dependent on their choice. Specifically, $\frac{\partial^4 F^2_{g,\mathrm{Car}}}{\partial \delta t^4}|_{\delta t=0}$ is a function of n_1, n_2, therefore it is beneficial to choose the harmonics such that this leading order is minimized.

To do so we must write the derivative explicitly:

$$-\frac{1}{4!}\frac{\partial^4 F^2_{g,\mathrm{Car}}}{\partial \delta t^4}|_{\delta t=0}\delta t^4 = \left(\bar{n}+\frac{1}{2}\right)\frac{n_1 n_2 \left(n_1-n_2\right)^2}{n_1+n_2}\eta\Omega^4\delta t^4 = \left(\bar{n}+\frac{1}{2}\right)\eta\Omega^4\delta t^4 \begin{cases} \frac{2}{3} & (1,2) \\ \frac{6}{5} & (2,3) \\ 3 & (1,3) \\ \frac{150}{7} & (2,12) \end{cases} \tag{71}$$

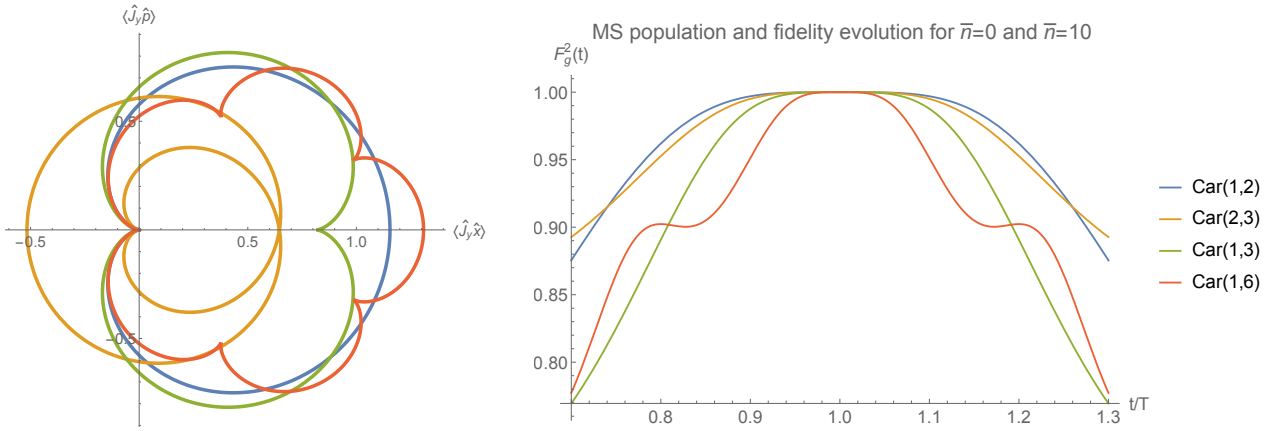

Figure 11: **Phase space trajectories and fidelity function for various Cardioid (n_1, n_2) driving schemes**. Obviously Cardioid $(1, 2)$ is optimal, however deviates only slightly from Car $(2, 3)$ and other schemes.

The 4th order term is therefore minimized by choosing $n_1 = 1$ and $n_2 = 2$, thus indeed the Cardioid $(1, 2)$ is optimal. We also emphasize the Cardioid $(2, 3)$, which we are interested in due to technical non-linear responses in our system (see 2.8). Fig. 11 shows the phase space trajectory of different Cardioid (n_1, n_2). While the "heart" shape is only a characteristic of Cardioid $(1, 2)$ we retain the name for the other schemes as well since they all share the same scaling of fidelity.

2.5.2 Cardioid ladder gate

Generalizing further the definition for Cardioid (n_1, n_2) we defined Cardioid $(n_1, n_2, ..., n_N)$ as a composite gate with harmonics $\{n_j\}_{j=1}^N \in \mathbb{Z}^N$ such that the amplitudes abide the Vandermonde solution above:

$$r_j = \frac{1}{\sqrt{K}} \prod_{j \neq k=1}^{N} \frac{1}{n_j - n_k}, \quad K = \sum_{j=1}^{N} \frac{\tilde{r}_j^2}{n_j} \tag{72}$$

We denote the specific choice $n_j = j$ as a *ladder Cardioid* (or Cardioid $(N) \equiv$ Cardioid $(1, 2, ..., N)$), for which analytic closed form results are more easily obtained. The unnormalized amplitudes are given by:

$$\tilde{r}_j = \prod_{j \neq k} \frac{1}{j - k} = \frac{(-1)^{N-j}}{(j-1)!\,(N-j)!} \tag{73}$$

And are easily normalized such that:

$$r_j = \frac{1}{\sqrt{K}} \tilde{r}_j = (-1)^{N-j} \frac{N!}{2^N} \sqrt{\frac{2\sqrt{\pi}}{(N-1)!\Gamma\left(N + \frac{1}{2}\right)}} \binom{N-1}{j-1} \tag{74}$$

These form an oscillating positive-negative pattern with an envelope that approaches a Gaussian as $N \to \infty$ with $\mu \to \frac{N+1}{2}$ and $\sigma^2 \to \frac{N}{4}$, as shown in Fig. 12. By using a Stirling approximation we note that the scaling of the maximal amplitude is $r_{N/2} \sim \left(\frac{N}{\pi}\right)^{\frac{1}{4}}$.

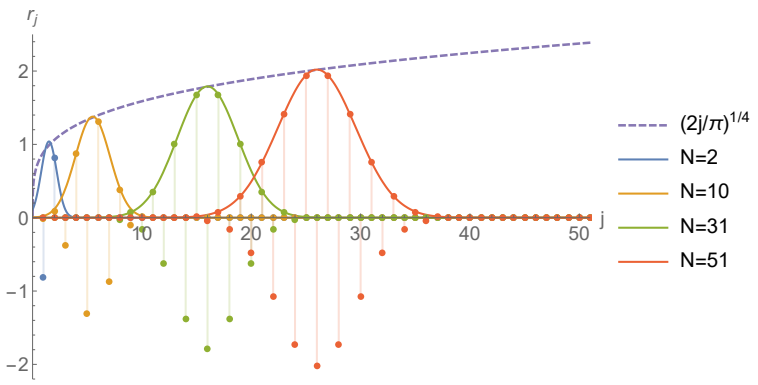

Figure 12: **Amplitudes of ladder Cardioid.** The required amplitude form a oscillating positive-negative pattern with a Gaussian envelope such that $\mu = \frac{N+1}{2}$ and $\sigma^2 = \frac{N}{4}$. The largest amplitudes is r_j for $j = \left\lfloor \frac{N+1}{2} \right\rfloor$ and scales as $\left(\frac{N}{\pi}\right)^{\frac{1}{4}}$ (dashed purple).

We note that so far our analysis treated Ω as a parameter of the system (and not a degree of freedom). While Ω is limited by the off-resonance carrier coupling (see: 2.2.3), in some implementations there might be technical limitations on the maximum or total field or power of the laser components. Assuming we are limited by some maximum total Rabi frequency $\Omega_{\max}$, such that $\Omega \sum_{j=1}^{N} 2\left|r_j\right| \leq \Omega_{\max}$ (set, for example, by the maximal instantaneous laser power available). Then we obtain the following scaling for the gate time:

$$T_\Omega = \frac{2\pi}{\xi_0} = \frac{\pi}{\eta\Omega} = \frac{\pi}{\eta\Omega_{\max}} N \sqrt{\frac{2\sqrt{\pi}\Gamma\left(N\right)}{\Gamma\left(N+\frac{1}{2}\right)}} \overset{N\gg 1}{\longrightarrow} \left(4\pi N^3\right)^{\frac{1}{4}} \tag{75}$$

Thus, for a field-limited source the gate time scales with $N^{\frac{3}{4}}$. The phase space trajectory coordinates are given by:

$$\begin{cases} G\left(t\right) = \sqrt{\frac{\sqrt{\pi}(N-1)!}{\Gamma\left(N+\frac{1}{2}\right)}} \sin^N\left(\frac{\xi_0 t}{2}\right)\left(\left(\frac{1-(-1)^N}{2}\right)(-1)^{\frac{N+1}{2}} \sin\left(\frac{N\xi_0 t}{2}\right) + \left(\frac{1+(-1)^N}{2}\right)(-1)^{\frac{N}{2}} \cos\left(\frac{N\xi_0 t}{2}\right)\right) \\ F\left(t\right) = \sqrt{\frac{\sqrt{\pi}(N-1)!}{\Gamma\left(N+\frac{1}{2}\right)}} \sin^N\left(\frac{\xi_0 t}{2}\right)\left(\left(\frac{1-(-1)^N}{2}\right)(-1)^{\frac{N+1}{2}} \cos\left(\frac{N\xi_0 t}{2}\right) - \left(\frac{1+(-1)^N}{2}\right)(-1)^{\frac{N}{2}} \sin\left(\frac{N\xi_0 t}{2}\right)\right) \end{cases} \tag{76}$$

Where the prefactor scales as $\left(\frac{\pi}{N}\right)^{\frac{1}{4}}$ for $N \gg 1$. Presenting this using radial coordinates is much simpler:

$$\begin{cases} R\left(t\right) = \sqrt{G^2\left(t\right) + F^2\left(t\right)} = \sqrt{\frac{\sqrt{\pi}(N-1)!}{\Gamma\left(N+\frac{1}{2}\right)}} \left|\sin^N\left(\frac{\xi_0 t}{2}\right)\right| \\ \phi\left(t\right) = \arctan\left(\frac{F(t)}{G(t)}\right) = (-1)^N \frac{N\xi_0 t}{2} \end{cases} \tag{77}$$

The trajectories formed by this driving scheme are shown in Fig. 11. We note that as N increases the trajectory crosses itself more times and eventually creates a higher order cusp at the origin (since $\frac{d^n F}{d^n G} = \frac{d^n F}{d^n t} / \frac{d^n G}{d^n t} \to \frac{0}{0}$ for $n = 1, ..., N$).

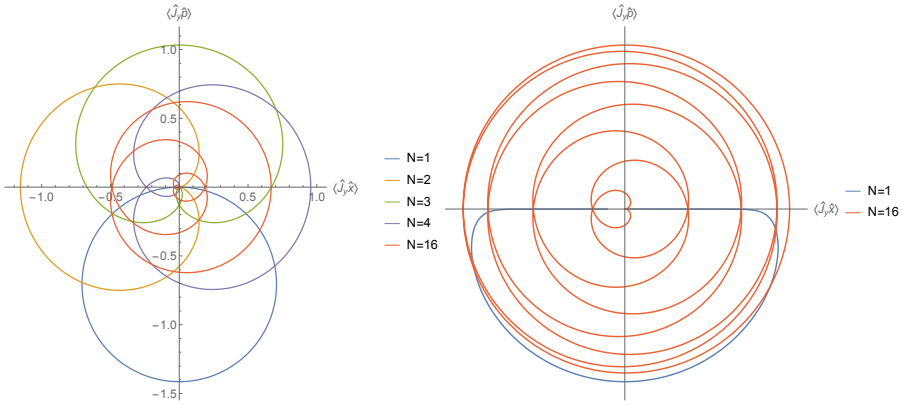

Figure 13: **Phase space trajectories of the ladder Cardioid. Left:** Examples of trajectories for $N = 1, 2, 3, 4, 8$. The standard MS gate is given by $N = 1$ (blue) and Cardioid $(1, 2)$ is given by $N = 2$ (orange). As N increases the trajectory intersects more times. These intersections occur closer and closer to the origin. **Right:** Stretched phase space trajectory: $\left(x(t)^{\frac{1}{16}}, y(t)^{\frac{1}{16}}\right)$, such that the finer details of $N = 16$ (red) close to the origin are now easily apparent. To emphasize the stretching the MS gate is also plotted (blue). Both trajectories correspond to MS $N = 1$ and $N = 16$ in the left plot.

The accumulated phase is then given by (see appendix: 6.3.2):

$$A(t) = \frac{\pi}{4} - \frac{\sqrt{\pi}N!}{2\Gamma\left(N+\frac{1}{2}\right)}\cos\left(\frac{\xi_0 t}{2}\right){}_2F_1\left(\frac{1}{2}, \frac{1}{2}-N; \frac{3}{2}; \cos^2\left(\frac{\xi_0 t}{2}\right)\right) - \frac{1}{4}R^2(t)\sin(2\phi(t)) \tag{78}$$

$$\equiv a(t) - \frac{1}{4}R^2(t)\sin(2\phi(t)) \tag{79}$$

Where ${}_2F_1(a, b; c; z)$ is the hypergeometric function, and we leave the second term implicit since it cancels terms in $\hat{\rho}(t)$ and $F_g^2(t)$. This allows a closed form expression for population evolution and fidelity of the ladder Cardioid gate:

$$\begin{cases} Pr(SS) = \frac{3+e^{-4\left(\bar{n}+\frac{1}{2}\right)\frac{R^2(t)}{2}}+4e^{-\left(\bar{n}+\frac{1}{2}\right)\frac{R^2(t)}{2}}\cos(a(t))}{8} \\ Pr(DD) = \frac{3+e^{-4\left(\bar{n}+\frac{1}{2}\right)\frac{R^2(t)}{2}}-4e^{-\left(\bar{n}+\frac{1}{2}\right)\frac{R^2(t)}{2}}\cos(a(t))}{8} \\ Pr(SD) = \frac{1-e^{-4\left(\bar{n}+\frac{1}{2}\right)\frac{R^2(t)}{2}}}{8} \\ Pr(DS) = \frac{1-e^{-4\left(\bar{n}+\frac{1}{2}\right)\frac{R^2(t)}{2}}}{8} \\ F_g^2 = \frac{3+e^{-4\left(\bar{n}+\frac{1}{2}\right)\frac{R^2(t)}{2}}}{8} + \frac{1}{2}\sin(a(t))e^{-\frac{R^2(t)}{2}\left(\bar{n}+\frac{1}{2}\right)} \end{cases} \tag{80}$$

These are shown in Fig. 14, where the increasing flatness of the gate is obvious both in population evolution and fidelity.

It is also beneficial to calculate the driving fields - this is given by:

$$\Omega(t) \propto \left[\sin\left(\left(\omega_{SD} + \nu + \frac{N+1}{2}\xi_0\right)t\right) + \sin\left(\left(\omega_{SD} - \nu - \frac{N+1}{2}\xi_0\right)t\right)\right]\sin^{N-1}\left(\frac{\xi_0 t}{2}\right) \tag{81}$$

That is, Cardioid (N) is equivalent to a $\sin^{N-1}\left(\frac{\xi_0 t}{2}\right)$ amplitude modulation of a standard MS gate with

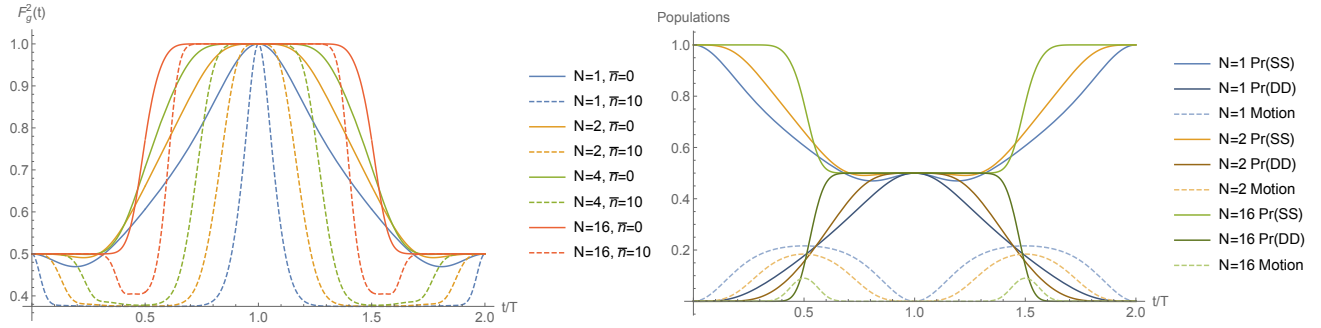

Figure 14: **Fidelity and evolution of ladder Cardioid. Left:** Fidelity for different N's. The fidelity becomes flat around gate time $t = T$ as N increases. This effect becomes obvious for hot ($\bar{n} = 10$) initial conditions (dashed). **Right:** Time evolution for different N's. As N increases the evolution around gate time becomes flatter (solid) and the maximal motion decreases (dashed).

symmetric detuning equal to $\frac{N+1}{2}\xi_0$. It is not hard to show that $\int_0^T dt \left|\sin^N\left(\frac{\xi_0 t}{2}\right) - e^{-\frac{N}{2}\left(\frac{\xi_0}{2}\right)^2\left(t-\frac{\pi}{2}\right)^2}\right| \underset{N\to\infty}{\longrightarrow} 0$, therefore the optimal modulation converges to a Gaussian (but is definitely not a Gaussian for low N).

2.6 Optimizing off-resonance carrier coupling

We remind that in order to derive the interaction Hamiltonian allowing all the derivations above, we assumed $\Omega \ll \nu$ and used a RWA. For the standard MS gate we followed [20] to obtain a more accurate bound on the gate infidelity due to this approximation (see: 2.2.3).

We would like to follow a similar procedure for the composite gate and obtain a more accurate infidelity due to failure of the RWA, and use the harmonic degrees of freedom in order to minimize this infidelity. The term we neglected in the rotating frame approximation, is given by:

$$\hat{H}_d = 2\Omega\hat{J}_x \sum_{i=1}^{N} r_i \cos\left(\left(\nu + \xi_0 n_i\right) t - \phi_i\right) \equiv \hat{J}_x h_d\left(t\right) \tag{82}$$

Which creates direct carrier off-resonance coupling (i.e without exciting motion). As we did for the MS gate case, we re-introduce the direct carrier term and change to an interaction picture with respect to the unitary interaction operator $\hat{U}\left(t;0\right)$. We then calculate the remaining evolution by constructing a Dyson series:

$$\begin{cases} \hat{H}_{d,I}\left(t\right) = U^{\dagger}\left(t\right)\hat{H}_d\left(t\right)\hat{U}\left(t\right) \\ \hat{U}_I\left(t;0\right) = \mathbb{1} - i\int_0^t dt_1 \hat{H}_{d,I}\left(t_1\right) - \int_0^t dt_1 \int_0^{t_1} dt_2 \hat{H}_{d,I}\left(t_1\right)\hat{H}_{d,I}\left(t_2\right) + ... + \left(-i\right)^n \int_0^t dt_1 \cdots \int_0^{t_{n-1}} dt_n \hat{H}_{d,I}\left(t_1\right)\cdots\hat{H}_{d,I}\left(t_n\right) \end{cases} \tag{83}$$

$\hat{H}_d$ is fast oscillating, thus may treat $\hat{U}\left(t\right)$ as a constant during the integration. Near the gate time we set $\hat{U}\left(t\right) = e^{i\frac{\pi}{2}\hat{J}_y^2}$. Using:

$$\left(e^{-i\frac{\pi}{2}\hat{J}_y^2}\hat{J}_x e^{i\frac{\pi}{2}\hat{J}_y^2}\right)^n = \left(-\frac{\sigma_z\otimes\sigma_y+\sigma_y\otimes\sigma_z}{2}\right)^n = (-1)^n\begin{cases}\frac{\sigma_z\otimes\sigma_y+\sigma_y\otimes\sigma_z}{2} & n \text{ odd}\\ \hat{J}_y^2 & n \text{ even}\end{cases} \tag{84}$$

We note that for $|\psi(0)\rangle = |SS\rangle$ we have:

$$\begin{cases}\left\langle\psi_I(0)\left|\frac{\sigma_z\otimes\sigma_y+\sigma_y\otimes\sigma_z}{2}\right|\psi_I(0)\right\rangle = 0\\ \left\langle\psi_I(0)\left|\hat{J}_y^2\right|\psi_I(0)\right\rangle = \frac{1}{2}\end{cases} \tag{85}$$

Thus we are only concerned with the even terms of this series. For the time dependent term we have:

$$I_n \equiv (-i)^n\int_0^T dt_1\cdots\int_0^{t_{n-1}} dt_n\hat{h}_{d,I}(t_1)\cdots\hat{h}_{d,I}(t_n) \tag{86}$$

$$= (-i)^n(2\Omega)^n\int_0^T dt_1\cdots\int_0^{t_{n-1}} dt_n\left[\sum_{i=1}^N r_i\cos\left(\left(\nu-\xi_0 n_i\right)t_1-\phi_i\right)\right]\cdots\left[\sum_{i=1}^N r_i\cos\left(\left(\nu-\xi_0 n_i\right)t_n-\phi_i\right)\right] \tag{87}$$

$$= \frac{(-i)^n}{n!}\left[2\Omega\sum_{i=1}^N r_i\frac{\sin(\nu T-\phi_i)}{\nu-\xi_0 n_i}\right]^n \tag{88}$$

Thus, the direct carrier coupling fidelity is given by:

$$F_d = \sum_{n=0}^{\infty} I_{2n} = \sum_{n=0}^{\infty}\frac{(-1)^n}{(2n)!}\left(2\Omega\sum_{i=1}^N r_i\frac{\sin(\nu T-\phi_i)}{\nu-\xi_0 n_i}\right)^{2n} \tag{89}$$

Assuming $\nu = \nu_0+\delta\nu$ such that $\nu_0 = m\xi_0$ with $m\in\mathbb{Z}$, and assuming that $\phi_i = 0$ (and $r_i\in\mathbb{R}$) we obtain:

$$F_d = \sum_{n=0}^{\infty} I_{2n} = \sum_{n=0}^{\infty}\frac{(-1)^n}{(2n)!}\left(\frac{2\Omega}{\nu}\sin(\delta\nu T)\sum_{i=1}^N r_i\frac{1}{1-\frac{\xi_0 n_i}{\nu}}\right)^{2n} + \mathcal{O}\left(\frac{n_N\xi_0}{\nu}\right) \tag{90}$$

$$= \sum_{n=0}^{\infty}\frac{(-1)^n}{(2n)!}\left(\frac{2\Omega}{\nu}\sin(\delta\nu T)\sum_{i=1}^N r_i\left(\sum_{j=0}^{\infty}\left(\frac{\xi_0 n_i}{\nu}\right)^j\right)\right)^{2n} \tag{91}$$

Therefore, we obtain conditions to eliminating carrier coupling order by order:

$$\begin{pmatrix}1 & 1 & \cdots & 1\\ \frac{\xi_0 n_1}{\nu} & \frac{\xi_0 n_2}{\nu} & \cdots & \frac{\xi_0 n_N}{\nu}\\ \left(\frac{\xi_0 n_1}{\nu}\right)^2 & \left(\frac{\xi_0 n_2}{\nu}\right)^2 & \cdots & \left(\frac{\xi_0 n_N}{\nu}\right)^2\\ \vdots & \vdots & \ddots & \vdots\\ \left(\frac{\xi_0 n_1}{\nu}\right)^{N-1} & \left(\frac{\xi_0 n_2}{\nu}\right)^{N-1} & \cdots & \left(\frac{\xi_0 n_N}{\nu}\right)^{N-1}\end{pmatrix}\begin{pmatrix}r_1\\ r_2\\ r_3\\ \vdots\\ r_N\end{pmatrix} = \mathbf{0} \tag{92}$$

Which is of course a Vandermonde matrix very similar in form to that obtained when optimizing gate timing-error robustness (see: 2.5). It is solved by the exact same Cardioid solution:

$$\tilde{r_j} = \prod_{j \neq k=1} \frac{1}{n_j - n_k} \tag{93}$$

Thus, optimizing time robustness is exactly the same as minimizing off-resonance carrier coupling. The correspondence between reducing off-resonance carrier coupling and using a smooth driving force has a simple intuition - since the gate is finite in time its Fourier transform is made of the drive's spectral lines which are convoluted with some response function with decaying tails. As is known from Fourier theory, the decay is faster as the time-domain function is smoother. Therefore a smooth drive creates a narrower spectrum, which reduces the spectral overlap with the carrier.

This has already been noticed in [13] where a double $\cos^2$ envelope had been suggested, and in [14] where a Blackman window had been implemented. In this context, we have provided here an exact analysis which verifies this intuition from the point of view of the spectral degrees of freedom. In addition, [13] suggests using an intermediate pulse which is required due to a spectral overlap of the $\cos^2$ envelop with the red and blue side-bands, which in our method are avoided by construction.

The infidelity due to carrier coupling of a ladder Cardioid is given by:

$$1 - F_d = 1 - \sum_{n=0}^{\infty} \frac{(-1)^n}{(2n)!} \left(\frac{2\Omega}{\nu} \sin(\delta\nu T) \sum_{j=1}^{N} r_j \left(\frac{\xi_0 j}{\nu} \right)^{N-1} \right)^{2n} + \mathcal{O}\left(\left(\frac{\xi_0 n_i}{\nu} \right)^{2N+2} \right) \tag{94}$$

$$= 1 - \cos\left(\frac{2\Omega}{\nu} \sin(\delta\nu T) \sum_{j=1}^{N} r_j \left(\frac{\xi_0 j}{\nu} \right)^{N-1} \right) \sim \left(\frac{\Omega}{\nu} \right)^{2N} \eta^{2N-2} \tag{95}$$

We note the error is doubly reduced as both $\frac{\Omega}{\nu}$ and η are assumed to be small. This infidelity is shown in Fig. 15. As expected, the worst case occurs for $\delta\nu = \frac{\pi}{2T}$. We note that adding components greatly reduces the infidelity, which allows the use of stronger driving fields. For example, when increasing $\frac{\Omega}{\nu}$ from $\frac{1}{10}$ to $\frac{1}{2}$ (increasing the intensity by 25!) only 3 driving components are required in order to keep the infidelity below 10^{-5} (where we used $\eta^{-1} = 26$), which is lower than using $\frac{\Omega}{\nu} = \frac{1}{10}$ and $N = 1$. The gate time is ultimately decreased:

$$\frac{T\left(N = 3, \frac{\Omega}{\nu} = \frac{1}{2}\right)}{T\left(N = 1, \frac{\Omega}{\nu} = \frac{1}{10}\right)} \to \frac{1}{5} \cdot 3 \sqrt{\frac{2\sqrt{\pi}\Gamma(3)}{\Gamma\left(3 + \frac{1}{2}\right)}} \approx 0.44 \tag{96}$$

Where the first factor is due to the increase in Ω and the second is due to using a Cardioid (3) ladder gate.

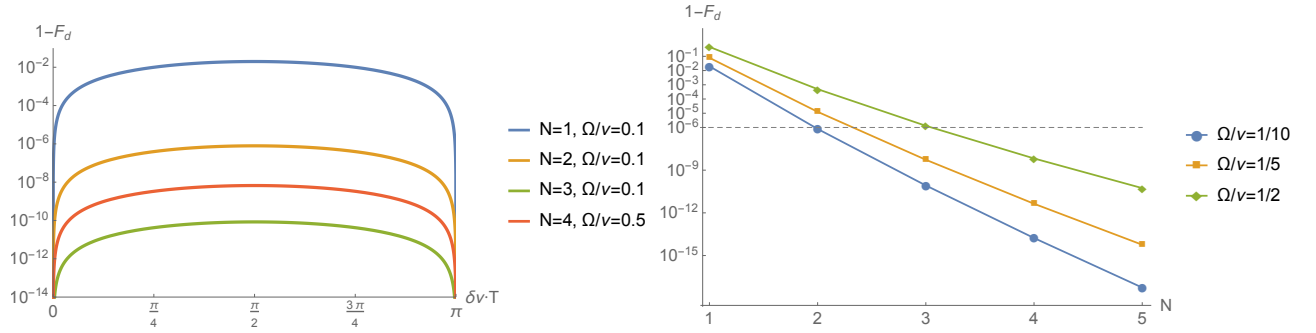

Figure 15: **Infidelity due to off resonance carrier coupling for N and Ω. Left:** Infidelity due to off resonance direct carrier coupling ladder Cardioid gate (for a typical $\eta^{-1} = 26$). At $\delta\nu = 0$ the infidelity is 0 for all gate types, however it maximizes at $\delta\nu \to \frac{\pi}{2}$. For a standard MS gate the infidelity peaks at ~ 0.02 (blue), for conventional Rabi frequency and trap frequency such that $\frac{\Omega}{\nu} = 0.1$. As N increases the worst case value quickly decays by 2 orders of magnitude per harmonic (log scale). For comparison we show that for $N = 3$ one may increase the ratio to $\frac{\Omega}{\nu} = 0.5$ and still have extremely low infidelities. **Right:** Worst case infidelity (for $\eta^{-1} = 26$) for different Rabi frequencies and driving components. We note that one may increase the Rabi frequency by factor 5 and compensate the infidelity by using $N = 3$, this results in a shorter gate time: $T_{N=3} \approx T_{N=1} \cdot 0.44$.

2.7 Optimizing robustness to harmonic trap frequency drifts

Another systematic error which might prove to be a more serious problem in gate implementations, is an error in the harmonic trap frequency ν. The trap frequency is usually measured via red and blue side-band spectroscopy and may suffer from calibration errors as well as trap voltage drifts. We note that an error of the form $\nu \to \nu_0 + d\nu$, where ν_0 is the actual trap frequency and $d\nu$ is a systematic error, will change the driving frequencies such that $\xi_j = n_j\xi_0 \to n_j\xi_0 - d\nu$. This no longer satisfies the constrain $T\xi_j = 2\pi n_j$, and therefore the ions' initial motional state will not be recovered at gate time. We remind that the driving frequency also controls the radius of motion in phase space, therefore the phase space area will also change such that the accumulated correlated phase will deviate from $\frac{\pi}{2}$ at gate time.

Due to such an error the phase space positions at gate time becomes:

$$\begin{cases} F(T) = \sqrt{2}\sum_{i=1}^{N} \frac{r_i}{2n_i - \frac{d\nu}{\eta\Omega}} \left(\sin\left(\pi \frac{d\nu}{\eta\Omega}\right)\right) \\ G(T) = \sqrt{2}\sum_{i=1}^{N} \frac{r_i}{2n_i - \frac{d\nu}{\eta\Omega}} \left(1 - \cos\left(\frac{d\nu}{\eta\Omega}\pi\right)\right) \end{cases} \tag{97}$$

Where we already assumed that $\xi_0 = 2\eta\Omega$. We immediately recognize that $\eta\Omega$ is the correct frequency scale for $d\nu$.

To optimize robustness against such errors we demand $\frac{\partial^n F(T)}{\partial d\nu^n}|_{d\nu=0} = \frac{\partial^n G(T)}{\partial d\nu^n}|_{d\nu=0} = 0$ for $n = 0, 1, 2, ...$ Thus in the first order we obtain:

$$\begin{cases} \frac{\partial F(T)}{\partial d\nu}|_{d\nu=0} \propto \sum_{i=1}^{N} \frac{r_i}{n_i} \\ \frac{\partial G(T)}{\partial d\nu}|_{d\nu=0} = 0 \end{cases} \tag{98}$$

And in the second order:

$$\begin{cases} \frac{\partial^2 F(T)}{\partial d\nu^2}|_{d\nu=0} \propto \sum_{i=1}^{N} \frac{r_i}{n_i^2} \\ \frac{\partial^2 G(T)}{\partial d\nu^2}|_{d\nu=0} \propto \sum_{i=1}^{N} \frac{r_i}{n_i} \end{cases} \tag{99}$$

And in the third:

$$\begin{cases} \frac{\partial^3 F(T)}{\partial d\nu^2}|_{d\nu=0} \propto C_1 \sum_{i=1}^{N} \frac{r_i}{n_i^3} + C_2 \sum_{i=1}^{N} \frac{r_i}{n_i} \\ \frac{\partial^3 G(T)}{\partial d\nu^3}|_{d\nu=0} \propto \sum_{i=1}^{N} \frac{r_i}{n_i^2} \end{cases} \tag{100}$$

This may be summarized by the conditions:

$$\begin{pmatrix} \frac{1}{n_1} & \frac{1}{n_2} & \cdots & \frac{1}{n_N} \\ \frac{1}{n_1^2} & \frac{1}{n_2^2} & \cdots & \frac{1}{n_N} \\ \vdots & & \ddots & \\ \frac{1}{n_1^{N-1}} & \frac{1}{n_2^{N-1}} & \cdots & \frac{1}{n_N^{N-1}} \end{pmatrix} \begin{pmatrix} r_1 \\ r_2 \\ \vdots \\ r_N \end{pmatrix} = \mathbf{0} \tag{101}$$

This is yet again a Vandermonde matrix which is solved by the (unnormalized) amplitudes:

$$\tilde{r_j} = \prod_{j \neq k=1} \frac{1}{\frac{1}{n_j} - \frac{1}{n_k}} \tag{102}$$

This condition is sufficient to increase robustness to the state purity $P = \mathrm{Tr}\left(\hat{\rho}_q^2\right)$. However, to increase the robustness of the total fidelity one must also demand: $\frac{\partial^n A}{\partial d\nu}|_{d\nu=0} = 0$, this is given by:

$$\frac{\partial A}{\partial d\nu}|_{d\nu=0} \propto \sum_{i,j=1}^{N} \frac{r_i r_j}{n_i n_j} \tag{103}$$

Combined with $\sum \frac{r_i^2}{n_i} = 1$, this condition cannot be fulfilled with non zero amplitudes. Thus we settle for optimizing the robustness of the purity (this in turn also increases the fidelity but not in an order-by-order manner). We denote such a gate a *Nuoid*. One may combine constraints such that direct off-resonance carrier coupling (and time robustness) are achieved in the first order together with purity robustness to harmonic frequency errors. For $N = 3$ this is given by the set:

$$\begin{cases} \sum_{i=1}^{3} \frac{r_i^2}{n_i} = 1 & \text{Normalization} \\ \sum_{i=1}^{3} r_i = 0 & \text{Cardioid} \\ \sum_{i=1}^{3} \frac{r_i}{n_i} = 0 & \text{Nuoid} \end{cases} \tag{104}$$

Which we denote *CarNu*. We note that 3 driving components are enough to implement this gate. This gate's phase space trajectory and time evolution are shown Fig. 16, where we note that the CarNu $(1, 2, 3)$ trajectory is closed (in an extremely good approximation) in the presence of harmonic trap errors while MS or Cardioid $(1, 2, 3)$

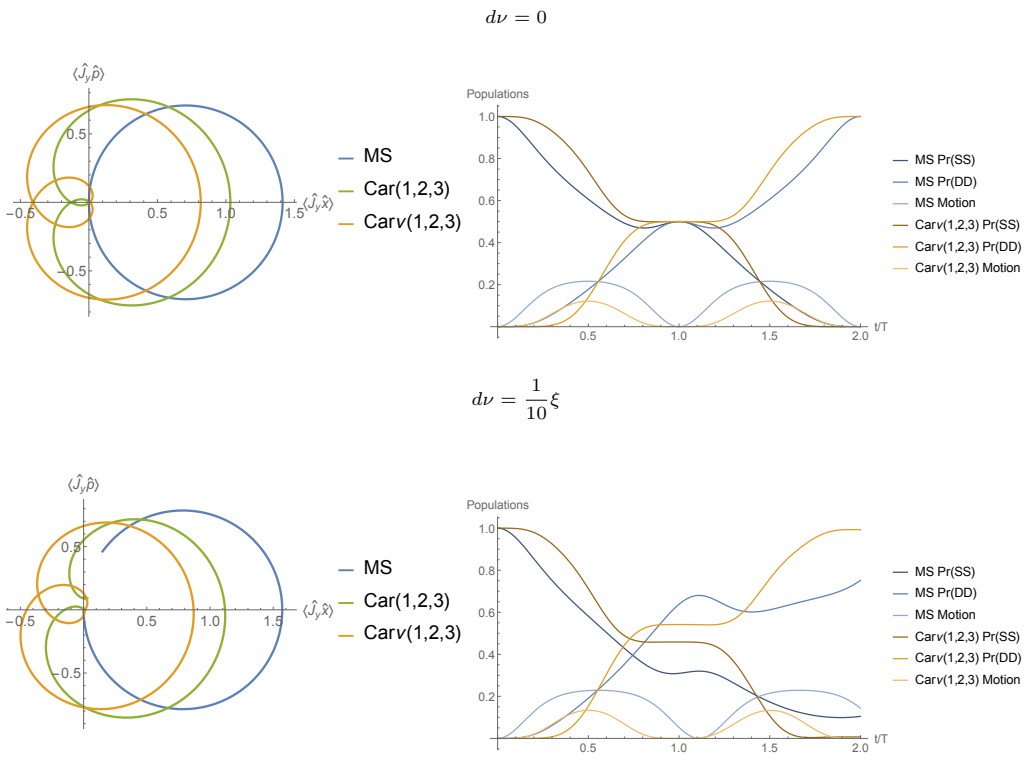

Figure 16: **Phase space trajectory and evolution of CarNu gate. Top Left:** Phase space comparing MS gate (blue), Cardioid $(1,2,3)$ gate (green) and CarNu $(1,2,3)$ gate (orange) for $d\nu = 0$. All these trajectories correspond to valid entangling gates. **Top Right:** Time evolution of MS gate (blue) and CarNu $(1,2,3)$ gate (orange) for $d\nu = 0$. We note that the time evolution of CarNu $(1,2,3)$ is flat due to the Cardioid constraint it satisfies in the first order. **Bottom Left:** Same phase space trajectories as in the top left figure, in the presence of a harmonic trap frequency error $d\nu = \frac{1}{10}\xi_0$. The CarNu $(1,2,3)$ gate almost returns completely to the origin while the MS and Cardioid $(1,2,3)$ gates completely miss the origin at gate time. **Bottom right:** Same time evolution as the top right figure, in the presence of a harmonic trap frequency error $d\nu = \frac{1}{10}\xi_0$. As expected the MS gate (blue) creates a large imbalance between the $|SS\rangle$ and $|DD\rangle$ populations, which indicates a large error in the enclosed phase space area. Moreover the MS gate generates motion since the minima of $|SD\rangle$ and $|DS\rangle$ misses the gate time. In contrary, the imbalance between $|SS\rangle$ and $|DD\rangle$ for CarNu $(1,2,3)$ is small and the motion is kept minimal at the gate time. Both indicate increased robustness to harmonic trap frequency errors.

do not return to the origin. The resulting robustness to time errors and trap frequency errors is shown in Fig. 17, where the fidelity "landscape" due to gate timing-errors and harmonic trap errors is fast varying for the MS gate and "boring" for the CarNu $(1,2,3)$ gate.

2.8 Technical non-linear response

A conventional method to implement a composite entangling gate (and the standard MS gate as well) is by modulating a (slightly detuned) carrier laser beam with the appropriate side-bands using an acusto-optical modulator, this is convenient since generating the modulating signal is easier in the RF domain than the optical domain (as is done in this work, see 3). However, such an approach is prone to 3rd order non-linear response which creates an on-resonance coherent driving.

To understand how these appear we will consider a conventional RF amplifier (the analysis is analogous to other

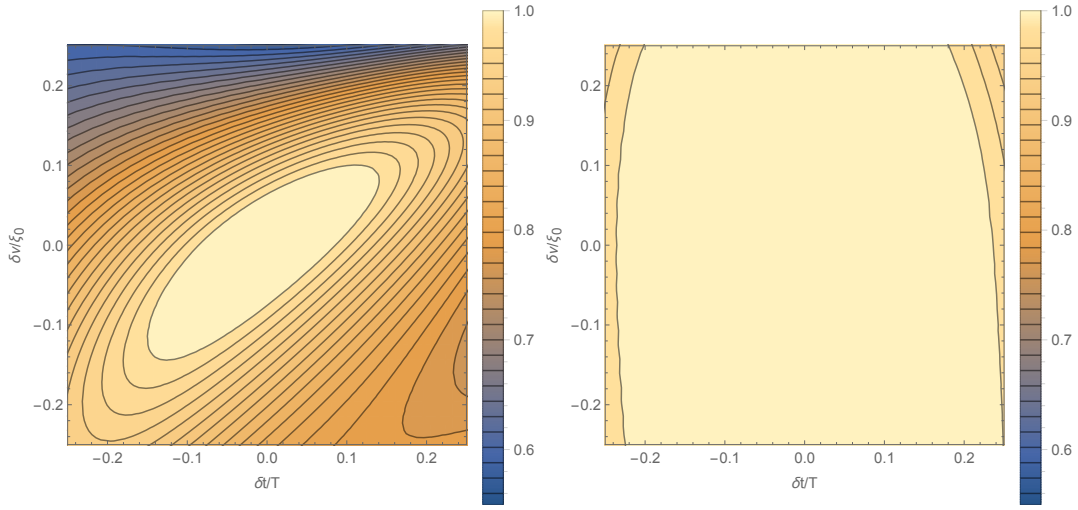

Figure 17: **Robustness of CarNu $(1,2,3)$ and MS gates to gate timing-errors and harmonic trap frequency errors.** Both show the gate fidelity as a function of $\frac{\delta t}{T}$ and $\frac{\delta \nu}{\xi_0}$. For MS gate (left) we note that the gate is extremely sensitive to the these errors while the CarNu $(1,2,3)$ gate (right) is robust, thus the response is almost completely flat.

typical RF devices such as arbitrary waveform generators and AOMs), which can be modeled by the simple response function: $O(s) = Gs - D_2 s^2 - D_3 s^3$, where G is the linear amplification and D_2 and D_3 are second and third order responses. For an input signal of the form: $E_{in} = \sum_{i=1}^{N} E_i e^{i\omega_i t + \phi_i}$ the amplifier response is:

$$E_{out} = A_1 E_{in} + A_2 \sum_{i,j=1}^{N} E_i^{(*)} E_j^{(*)} e^{i(\pm\omega_i \pm \omega_j)t \pm \phi_i \pm \phi_j} \tag{105}$$

$$+ A_3 \sum_{i,j,k=1}^{N} E_i^{(*)} E_j^{(*)} E_k^{(*)} e^{i(\pm\omega_i \pm \omega_j \pm \omega_k)t \pm \phi_i \pm \phi_j \pm \phi_k} \tag{106}$$

Where the first term is the linear response, and the next terms are the second and third order non-linear responses, represented by A_2 and A_3 (which correspond to D_2 and D_3). The amplitude is conjugated when the frequency is subtracted. For example, a Cardioid $(1,2)$ will require frequency components of the form: $\omega_{\pm,n} = \omega_{AOM} \pm (\nu + n\xi_0)$, where ω_{AOM} is the detuning of the laser from the carrier frequency (we assume $\omega_{AOM} > \nu$), and $n = 1, 2$. One of the terms of the third order response is:

$$\omega_{NL3} = \omega_{+,1} + \omega_{+,1} - \omega_{+,2} = \omega_0 + \nu \tag{107}$$

Which is an on-resonance blue side-band drive, similarly a red side-band on-resonance drive is generated. We also note that such an effect occurs for all odd responses. We note that even though A_3 is typically small, this effect is-non negligible since the typical coupling for it is determined by the side-band Rabi frequency $\eta\Omega$ while the

coupling of ω_{b_i,r_i} is typically determined by the off-resonance effective Rabi frequency $\eta\tilde{\Omega}$, with:

$$\eta\tilde{\Omega} = \frac{\eta\Omega}{\sqrt{1+\left(\frac{n_i\xi_0}{\eta\Omega}\right)^2}} = \frac{\eta\Omega}{\sqrt{1+2n_i^2}} = \frac{\eta\Omega}{\sqrt{5}} \tag{108}$$

Where we used $n_i = 2$ in the last term. The phase space trajectory of an on-resonance drive is a straight line (circle with infinite radius), therefore it excites motion without relaxing it.

Three types of solutions may be used to overcome this problem:

1. Use devices with a negligible 3rd order non-linear coefficient (A_3 above) - devices in which the non-linearity is completely negligible are difficult to find. In realistic devices we were able to find the problem was reduced but not eliminated.

2. Determine a corrected input signal $\tilde{E}_i$ which contains weak on resonance components which will exactly cancel the non-linear effect such that $E_{out} = A_1 E_i$ - this is feed-forward approach which is limited due to the fact that the non-linear coefficients are typically unstable.

3. Drive with frequency components that cannot sum up to an on-resonance drive by a third order non-linearity, for example, Cardioid $(2,3)$.

The third solution is the easiest to implement and robust, thus in the experimental part of the work we implemented Cardioid and CarNu with the harmonic sequence $\{2,3,7,8,12,13,...\}$. We note that other sequences may also be used such as : $\{n_i\} = \{1,3,5,7,...\}$ or $\{n_i\} = \{3,4,5,11,12,13,..\}$ etc. such that each term cannot be written as a sum of any two terms appearing earlier in the sequence.

2.9 Intermezzo: Floquet expansion for off-resonance drive

So far we have only dealt with on-resonance entangling gates, that is, gates where the two photon transition is resonant ($\delta = 0$). Here we will relax this constraint and provide a solution which is an expansion in orders of $\frac{\delta}{\xi}$ based on a Floquet expansion.

The unitary evolution operator suggested in [20] is no longer a solution for the general $\delta \neq 0$ case. To see this we rewrite the interaction Hamiltonian in the RWA (see: 2.2.1):

$$\hat{V}_I = \frac{\hbar\eta\Omega}{2}\sum_i \left[i\hat{\sigma}_+^{(i)} e^{-i\phi}\left(\hat{a}e^{-i(\delta-\xi)t} + \hat{a}^\dagger e^{-i(\delta+\xi)t}\right) + h.c\right] \tag{109}$$

$$= \sqrt{2}\hbar\eta\Omega\left(\sin(\delta t+\phi)\,\hat{J}_x - \cos(\delta t+\phi)\,\hat{J}_y\right)(\cos(\xi t)\,\hat{x} - \sin(\xi t)\,\hat{p}) \tag{110}$$

Similarly to the on-resonance solution, we get a $\hat{x}$ and $\hat{p}$ excitation of the harmonic oscillator, however the spin rotation now oscillates between $\hat{J}_y$ and $\hat{J}_x$ with rate δ. We note that the different terms of the Hamiltonian are

no longer commuting over a constant due to the commutation $\left[\hat{J}_x, \hat{J}_y\right] = i\hat{J}_z$, thus a unitary similar to that of the on-resonance solution will no longer be a valid solution for this system (in other words, the Magnus expansion of such a Hamiltonian leads to an infinite series rather than only three terms).

By using the interaction picture $|\psi\rangle = e^{i(\delta t+\phi)\hat{J}_z}\left|\tilde{\psi}\right\rangle$ we obtain the interaction Hamiltonian:

$$\tilde{V}_I = -\eta\Omega\hat{J}_y\left(\hat{a}^\dagger e^{i\xi t} + \hat{a}e^{-i\xi t}\right) + \delta\hat{J}_z \tag{111}$$

Thus, an alternative and more intuitive picture for this interaction is that besides the "standard" entangling interaction we get an additional detuning term (similar to that of detuned Rabi oscillations) - this fits more nicely with the pictorial level scheme in Fig. 2. Again, this also shows why a simple $\hat{J}_y$ based unitary evolution is no longer a valid solution.

Therefore we need an alternative method for deriving the unitary evolution. By assuming that $\xi \gg \delta, \eta\Omega$ we are able to decompose the Hamiltonian to a time independent term $\delta\hat{J}_z$ and a fast oscillating time dependent term $\hat{V}_I^{\delta=0}$. Hamiltonian of this form may be treated in a Floquet framework such that the unitary evolution operator is decomposed into two parts - a slow varying time-independent *Floquet Hamiltonian* $\hat{H}_F$ and a fast oscillating *micro-motion operator* $\hat{U}_{\text{mm}}$ ([25]).

A constructive approach for approximating $\hat{H}_F$ and $\hat{U}_{\text{mm}}$ in increasing orders of $\frac{\delta}{\xi}, \frac{\eta\Omega}{\xi}$ is provided by [26], which can be thought of as deriving higher order of the conventional rotating wave approximation. We will follow this approach here for the off-resonance MS drive. The essence of the approach is as follows (see appendix: 6.4.1 for a more comprehensive overview of the method). Given a $\tau = \frac{1}{\xi}$ periodic Hamiltonian:

$$\hat{H}(t) = \hat{H}(t+\tau) = \hat{H}_0 + \hat{V}(t) \tag{112}$$

We derive a rotating frame $\hat{U}_{\text{mm}} = e^{iF(t)}$ and a time independent Floquet Hamiltonian given by this rotation:

$$\hat{H}_F = e^{i\hat{F}(t)}\hat{H}e^{-i\hat{F}(t)} + i\left[\partial_t e^{i\hat{F}(t)}\right]e^{-i\hat{F}(t)} \tag{113}$$

We expand the right hand side of this expression in orders of ξ^{-n} and demand self consistency, that is $\partial_t\hat{H}_F = 0$. This provides sufficient conditions for calculating the next order. The evolution is then given by:

$$\hat{U}(t) = e^{-i\hat{F}(t)}e^{-i\hat{H}_F t}e^{i\hat{F}(0)} \tag{114}$$

That is, rotating to the time independent frame, evolving a time independent Hamiltonian, and rotating back.

Executing this procedure up to order ξ^{-4} we obtain the Floquet Hamiltonian (see appendix: 6.4.3):

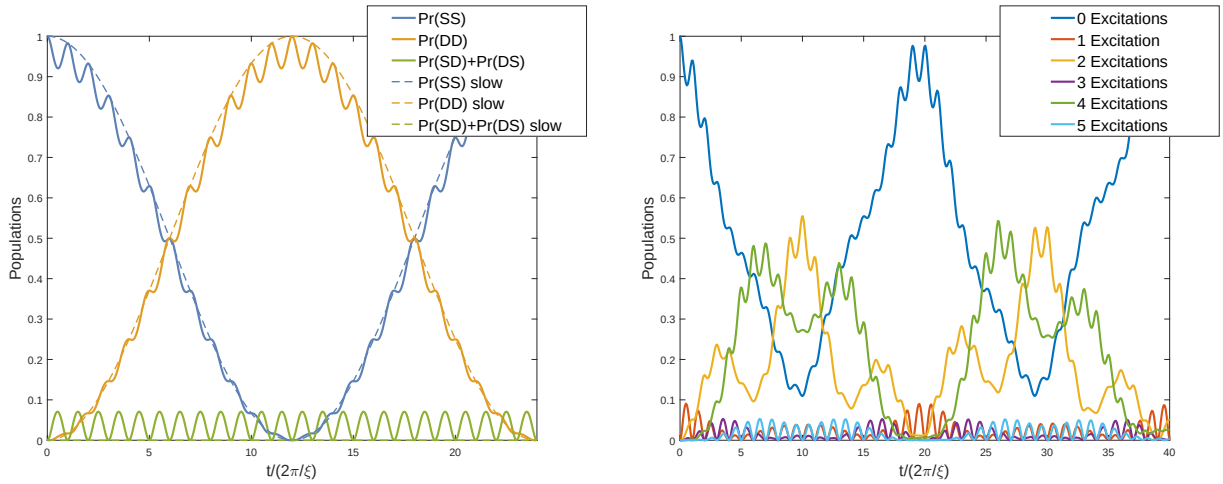

Figure 18: **Floquet expansion for off resonance MS gate. Left:** Time evolution of the MS gate with $n = 6$ (6th gate) such that $\xi = 2\sqrt{6}\eta\Omega$ and $T = 6 \cdot \frac{2\pi}{\xi}$. We note that the gate evolution is composed of two contributions: A slow evolution with large amplitude (dashed) due to the Floquet Hamiltonian $\hat{H}_F$, which creates an entangling gate at $t = T$ and flips the populations at $t = 2T$. And a fast and oscillating evolution due to $\hat{U}_{\text{mm}}$ superimposed on it (combined evolution in solid). We note that an entangling gate is still created at $t = T$ however the evolution is much more complex and involves motion population $|SD\rangle$ and $|DS\rangle$. **Right:** Population evolution of 5 ions using Floquet expansion for $\xi = 2\sqrt{10}\eta\Omega$ and $\delta = \frac{1}{100}\eta\Omega$. There are 32 different qubits states which we evolve in time, in the plot we sum populations according to the number of excitations, for example, 2 excitations (red) includes the state $|SSSDD\rangle$, $|SSDSD\rangle$, $|DSSSD\rangle$, etc.

$$\hat{H}_F = \hat{J}_z\delta\left(1 - \frac{\delta\left(\eta\Omega\right)^2}{\xi^2}\left(\hat{a}^\dagger\hat{a} + \frac{1}{2}\right)\right) - \frac{\left(\eta\Omega\right)^2}{\xi}\left(1 + \frac{\delta^2}{\xi^2}\right)\hat{J}_y^2 + \mathcal{O}\left(\xi^{-4}\right) \tag{115}$$

And the micro-motion operator:

$$\hat{F} = \frac{i\eta\Omega\hat{J}_y}{\xi}\left(\hat{a}^\dagger e^{i\xi t} - \hat{a}e^{-i\xi t}\right) - \frac{\eta\Omega\delta}{\xi^2}\hat{J}_x\left(\hat{a}^\dagger e^{i\xi t} + \hat{a}e^{-i\xi t}\right) \tag{116}$$

$$+ \frac{1}{\xi^3}\left[i\delta^2\eta\Omega\hat{J}_y\left(\hat{a}^\dagger e^{i\xi t} - \hat{a}e^{-i\xi t}\right) + i\delta\left(\eta\Omega\right)^2\hat{J}_z\left(\left(\hat{a}^\dagger\right)^2 e^{2i\xi t} - \left(\hat{a}\right)^2 e^{-2i\xi t}\right)\right] \tag{117}$$

$$+ \frac{1}{\xi^4}\left[\delta\left(\eta\Omega\right)^3\left(i\frac{29}{12}\hat{J}_z\hat{J}_y\hat{a}^\dagger e^{i\xi t} + \frac{5}{3}\hat{J}_x\hat{a}^\dagger e^{i\xi t} + \frac{11}{24}\hat{J}_x\left(\hat{a}^\dagger\right)^2\hat{a}e^{i\xi t} - \frac{3}{72}\hat{J}_x\left(\hat{a}^\dagger\right)^3 e^{3i\xi t}\right) - \delta^3\eta\Omega\hat{J}_x\hat{a}^\dagger e^{i\xi t} + h.c\right] + \mathcal{O}\left(\xi^{-5}\right) \tag{118}$$

This should be interpreted as follows, as $\frac{\delta}{\xi} \to 0$ the evolution may be divided to a fast "small" evolution and slow evolution. The fast evolution is determined by the (complicated) micro-motion operator $\hat{F}$, and the slow evolution is determined by a time independent Floquet Hamiltonian $\hat{H}_F$. Its structure is not surprising - a correlated rotation $\hat{J}_y^2$ with an effective coupling (Rabi frequency) $\frac{(\eta\Omega)^2}{\xi}$, which is the same scaling we know from the on-resonance solution. In addition a detuning term $\hat{J}_z$ which is dominated by δ. This contribution is shown in Fig. 18 where the micro-motion is superimposed on the slow and "dominant" evolution, the two different time scales are easily apparent.

A less intuitive result however is the appearance of the ladder operator $\hat{n} = \hat{a}^\dagger \hat{a}$ multiplying the anti-symmetric detuning in Eq. 115. That is, the detuning is corrected in order ξ^{-2} by $\bar{n}$ such that high temperatures imply a broadening and thus a less detuned response. In the next order we note the the entangling operation $\hat{J}_y^2$ is corrected as well by the anti-symmetric detuning. As a consistency check we note that for $\delta = 0$ the exact solution is recovered.

This method becomes extremely useful compared to the conventional time step numerical ODE when using more than 2 ions, since the simulation run-time increases exponentially with the number of ions (due to the exponential increase of Hilbert space dimension). Fig. 18 (right) shows such a calculation using 5 ions (the comparison to a simulation was not even attempted...).

To compare the exact solution and the Floquet expansion we simulate a few examples of gate evolution (making use of the Runge-Kutta ODE solvers in MATLAB® and [27]). We compare the behavior in different gate regimes $\xi \sim \delta$, $\xi > \delta$, $\xi \gg \delta$ and different temperatures. These are shown in Fig. 19.

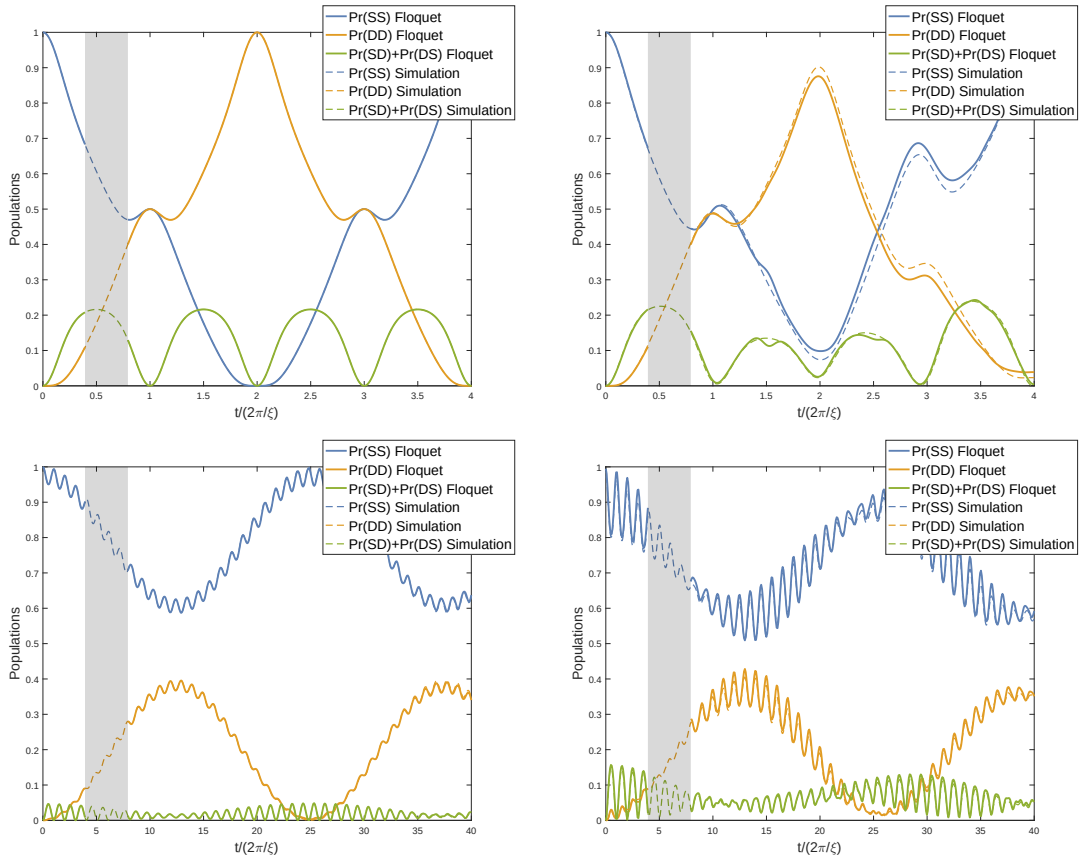

Figure 19: **Examples of population evolution comparing the Floquet expansion (solid) and direct simulation (dashed).** In the shaded areas we left out the solid line in order to see only the simulation. **Top left:** Standard MS gate, $\delta = 0$, $\xi = 2\eta\Omega$, in this regime the Floquet approximation is exact, as is easily seen in the figure. **Top right:** Off-resonance gate, $\delta = \frac{\xi}{20}$. Since $\frac{\delta}{\xi}$ is not small the Floquet expansion provides only a qualitative prediction. **Bottom left:** Off-resonance $n = 10$ gate such that $\xi = 2\sqrt{10}\eta\Omega$ and $\frac{\delta}{\xi} = \frac{1}{20\sqrt{10}}$ is small enough such that the Floquet expansion is extremely accurate. **Bottom right:** Same as left figure but with $\bar{n} = 2$ showing that the accuracy persists for mixed initial states as well.

3 Experimental system

The experimental system consists of a linear Paul trap, which uses a fast oscillating electric field in order to create a 3d harmonic pseudo-potential, and of lasers which are used to ionize ^{88}Sr atoms, Doppler cool, initialize, measure, excite\de-excite and repump them. Here we provide a brief overview of the system. Extensive details regarding the ion trap, lasers, optical paths and electronics are given in [28, 21].

3.1 Ion trap

The linear Paul trap consists of 6 electrodes (see Fig. 20, adapted from Fig. 1.3 of [21]). The two central electrodes, called end-caps, are put under a positive voltage such that they create a trapping DC potential for a positively charged particle along the axis parallel to them, called the axial direction, and an anti-trapping potential in the perpendicular plane, which is spanned by the radial directions. To compensate for this anti-trapping plane the remaining 4 electrodes create a trapping harmonic pseudo-potential by driving a $\Omega_{RF} = 21.7$ MHz fast oscillating voltage in two opposite electrodes, called RF electrodes, and a DC voltage in the two other, called DC electrodes. This effectively creates a quadropole electric field in this plane which changes direction at the fast oscillation rates. Similar to a Kapitza pendulum mechanism, these fast oscillations can be "traced out" and create a trapping harmonic potential. The formal description for the trap is given by the Mathieu equation, however this effect can be intuitively explained by separating the ion motion to a fast motion governed by the fast oscillating field and slow degrees of freedom which describe the effective motion: $x(t) = x_{\text{slow}}(t) + x_{\text{fast}}(t)$, and consider the average kinetic energy over the fast time scale:

$$\langle K \rangle_{\Omega_{RF}^{-1}} = \left\langle \frac{1}{2} m x^2(t) \right\rangle = \frac{1}{2} m \left(\left\langle x_{\text{slow}}^2(t) \right\rangle + 2 \left\langle x_{\text{fast}}(t) x_{\text{slow}}(t) \right\rangle + \left\langle x_{\text{fast}}^2(t) \right\rangle \right) \tag{119}$$

By assuming no correlation between the slow and fast degrees of freedom we obtain:

$$\langle K \rangle_{\Omega_{RF}^{-1}} = \frac{1}{2} m \left(\left\langle x_{\text{slow}}^2(t) \right\rangle + \left\langle x_{\text{fast}}^2(t) \right\rangle \right) \tag{120}$$

As the position of the ion is further from the quadropole minimum the field amplitude increases (quadratically around the minimum point), thus we may approximate the contribution of the fast term by a harmonic potential for the slow degree of freedom and obtain an effective trap:

$$\langle K \rangle_{\Omega_{RF}^{-1}} = \frac{1}{2} m \left\langle x_{\text{slow}}^2(t) \right\rangle + \omega^2 x_{\text{slow}}^2 + \text{const} \tag{121}$$

The DC electrode is used to break the $\frac{\pi}{2}$ symmetry of the quadropole plane such that the effective 3d harmonic potential is not degenerate (which is important for laser cooling). The parameters in our setup are such that the

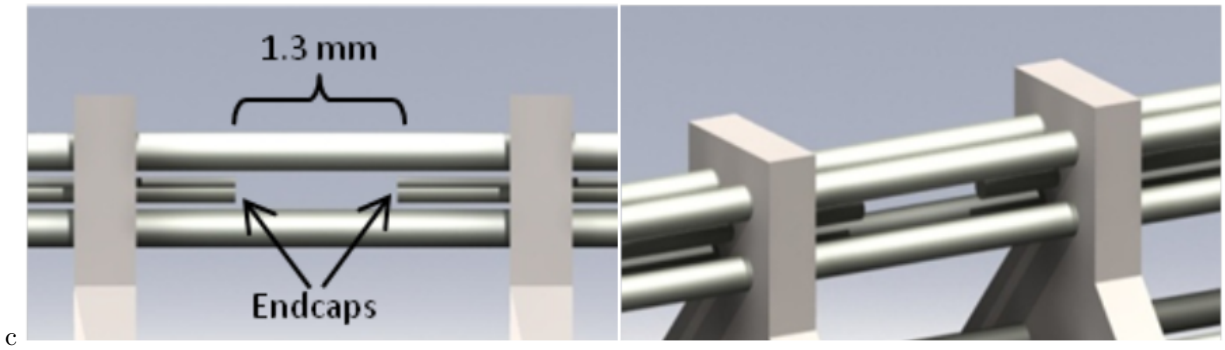

c

Figure 20: **Schematics of a linear Paul trap,** (adapted from Fig. 1.3 of [21]). The end caps are the middle electrodes which create a trapping potential in the axial axis spanned between them, while the 2 RF and 2 DC electrodes create a fast oscillating quadrupole potential which can be effectively treated as a harmonic potential in the radial plane.

axial trapping frequency is typically ~ 1.5 MHz and the radials are ~ 2.5 MHz.

3.2 Laser interaction with the ion

All operations on the ion are implemented with lasers which are tuned to the relevant transitions. These include: ionization, Doppler cooling, state preparation, measurement, qubit excitation, side-band cooling and repumps. Fig. 21 shows the relevant energy levels of the ^{88}Sr atom and $^{88}Sr^{+}$ ion and the lasers used in the system to couple the different levels (adapted from Figs 2.1 and 2.2 in [21]).

The main tools are the 422 nm and 674 nm lasers which are described in more detail below. Additional lasers are the two repump lasers: due to a $\sim 1:17$ branching ratio from the $5P_{\frac{1}{2}}$ manifold to $4D_{\frac{3}{2}}$ manifold a 1092 nm repump laser is used, and in order to pump the system to the ground state an 1033 nm laser repumps the $4D_{\frac{5}{2}}$ manifold to the $5P_{\frac{3}{2}}$ manifold, which decays fast to the ground state. Additionally there are ionization lasers, which create a two step ionization process.

3.2.1 422 nm laser: cooling, preparation and measurement

The 422 nm laser couples the $5S_{\frac{1}{2}}$ manifold, through a dipole transition, to the $5P_{\frac{1}{2}}$ manifold (see Fig. 21). The laser width is broad enough such that all levels are in principle coupled (assuming the transitions are allowed). This is used to implement Doppler cooling, state preparation and measurement of the effective two level system.

Doppler cooling is implemented by using a red detuned beam with frequency $\omega_{422} = \omega_{S_{\frac{1}{2}} \to P_{\frac{1}{2}}} - \delta$. When the ion has a velocity components v towards the laser beam's k-vector then due to Doppler effect the frequency in the ion frame of reference is increased by $\Delta\omega(v) = k \cdot v$. The laser is detuned such that $\delta \sim \Delta\omega(v)$ which means the laser is resonant with the moving ion and is excited to $5P_{\frac{1}{2}}$ while absorbing photons with momentum $-\hbar k$, which gradually slow it down. The ion emits the absorbed photons randomly (when decaying back to $5S_{\frac{1}{2}}$) which only adds fluctuations. Since the ion is set in a harmonic trap it is only necessary that the 422 nm overlaps all the

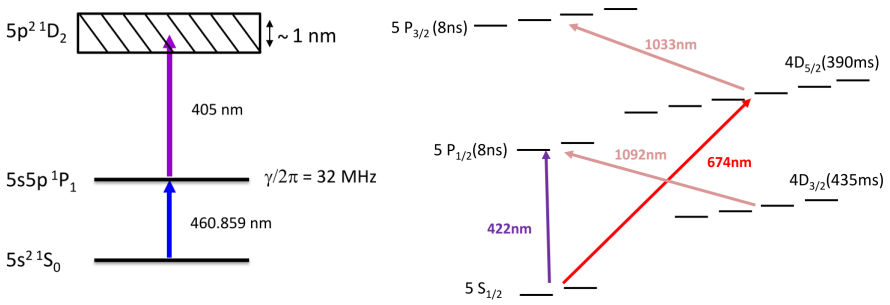

Figure 21: **Energy level of ^{88}Sr atom and ^{88}Sr$^+$ ion and the lasers used in the system,** (adapted from Figs. 2.1 and 2.2 in [21]). **Left:** Ionization scheme. A 460 nm beam ionizes one electron from the $5S$ ground state to the $5P$ orbital, a second 405 nm beam ionizes an additional electron from the $5S$ ground state to the continuum and effectively ionizes the atom, the remaining electron then spontaneously decays back to the $5S$ ground state. **Right:** Energy level of ^{88}Sr$^+$ ion, life times, and available laser in the setup. The 422 nm laser couples the $5S_{\frac{1}{2}}$ manifold through a dipole transition to the short lived (8 ns) $5P_{\frac{1}{2}}$ manifold, this transition is used for state preparation, state measurement and Doppler cooling. Due to a $\sim 1:17$ branching ratio from the $5P_{\frac{1}{2}}$ manifold to $4D_{\frac{3}{2}}$ manifold an 1092 nm repump laser is used. The 674 nm ultra narrow laser couples one state of the $5S_{\frac{1}{2}}$ manifold, through a quadropole transition, to one state of the $4D_{\frac{5}{2}}$ manifold, this transition is used as the effective qubit due to the long life times of the $4D_{\frac{5}{2}}$ manifold (390 ms) relative to the typical Rabi time (~ 3 μs). In order to pump the system to the ground state an 1033 nm laser repumps the $4D_{\frac{5}{2}}$ manifold to the $5P_{\frac{3}{2}}$ manifold, which decays fast to the ground state.

normal modes of the 3d trap such that it effectively adds damping to the ion dynamics and slows it down in all directions. This method is limited by the fluctuations generated in the decays, thus the minimal temperature is $T_{\text{Dop}} = \frac{\hbar\gamma}{2k_B} \approx 0.5$ mK, where γ is the decay rate from $5P_{\frac{1}{2}}$ to $5S_{\frac{1}{2}}$.

Fig. 22 (left) shows carrier Rabi oscillations of the $5S_{\frac{1}{2}} \rightarrow 4D_{\frac{5}{2}}$ transition after Doppler cooling an ion and the fitted oscillation which corresponds to an average occupation number of $\bar{n} = 9.8$.

State preparation is done by optical pumping on the $S_{\frac{1}{2}} \rightarrow P_{\frac{1}{2}}$ transition. This is performed by shining the ions with circular polarized light such that the wave vector is parallel to the magnetic field axis (which splits $S_{\frac{1}{2},\pm\frac{1}{2}}$). For example a σ^+ polarized light only couples to the $5S_{\frac{1}{2},-\frac{1}{2}} \rightarrow 5P_{\frac{1}{2},\frac{1}{2}}$ transition, which then quickly decays to $5S_{\frac{1}{2},\frac{1}{2}}$ or $5S_{\frac{1}{2},-\frac{1}{2}}$ with equal probability, however any remaining population in $5S_{\frac{1}{2},-\frac{1}{2}}$ will be excited again, therefore after n cycles the probability of measuring the ion in $5S_{\frac{1}{2},-\frac{1}{2}}$ is $\frac{1}{2^n}$, for $n \gg 1$ we say that the state is "pumped" to $5S_{\frac{1}{2},\frac{1}{2}}$.

Finally, state measurement is achieved by state selective fluorescence. Assuming the ion state is in the $5S_{\frac{1}{2}}$ manifold, then by turning on an on-resonance 422 nm beam the ion will be excited to the $5P_{\frac{1}{2}}$ and quickly spontaneously decay back to the $5S_{\frac{1}{2}}$ while emitting a 422 nm photon, and then be excited and decay again and again. Since the emitted photons have a completely random direction a camera which is outside of the laser optical path may collect these photons. However if the ion state has no overlap with $5S_{\frac{1}{2}}$ (say it is entirely in the $4D_{\frac{5}{2}}$ manifold) then no excitation-decay cycle will occur and no photons will be collected by the camera. Thus collecting photons on the camera are a measurement of the ion state (or more specifically, whether the ion is in the $5S_{\frac{1}{2}}$ manifold or not). By repeating experiments many times and measuring the ion state by this method one effectively measures the observable $\langle\hat{\sigma}_z\rangle$. Fig. 22 (right) shows the image of two ions pumped to the $5S_{\frac{1}{2}}$ manifold

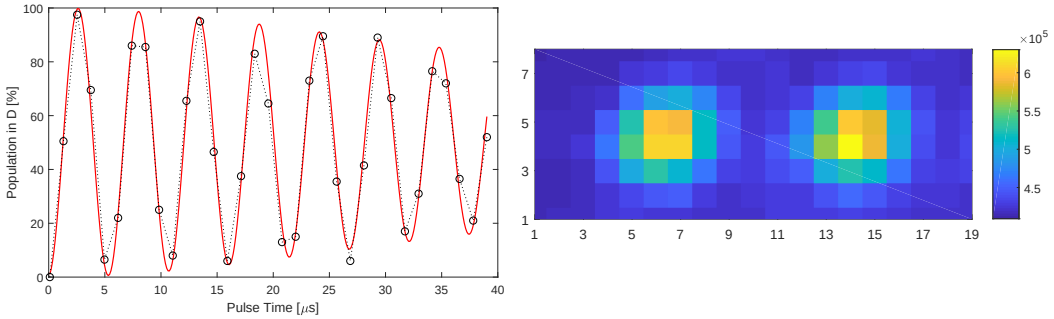

Figure 22: **Left:** Rabi oscillations of a single ion between the $5S_{\frac{1}{2}}$ and $4D_{\frac{5}{2}}$ manifolds. Data points (black) are obtained by averaging 625 repetitions (such that the projection noise is at most 2%) and the fit (red) corresponds to $\bar{n} = 9.81$. **Right:** 2 ions in the $5S_{\frac{1}{2}}$ manifold as captured by the EMCCD camera. The image is obtained by averaging 200 images of an exposure time of 1 ms each. The axis units are arbitrary pixels and the scale corresponds to the amplified electric readout of each pixel (corresponds non-linearly to photon count).

as captured by an EMCCD camera directed at the trap center.

3.2.2 674 nm laser: addressing the effective two level system

The 674 nm beam couples the $5S_{\frac{1}{2}} \rightarrow 4D_{\frac{5}{2}}$ manifold through a quadropole transition. This is an extremely narrow laser ($FWHM \sim 100$ Hz) which allows carefully choosing and coupling one state of $5S_{\frac{1}{2}}$ and one state of $4D_{\frac{5}{2}}$ with long coherence times. This is achieved by employing two Pound-Drever-Hall locking schemes in serial, with high finesse optical cavities (for more information see [28]).

The flop time is typically 2.5 μs, while the lifetime of the $4D_{\frac{5}{2}}$ manifold is ~ 390 ms such that many operations may be performed using this transition before any non-negligible decoherence occurs.

A multi-tone drive is generated by applying a multi-tone RF signal to a single pass AOM which modulates the RF field onto the laser light. This may be done by combining several RF generator signals, however a more general approach is to use an arbitrary waveform generator which in principle allows modulating any multi-tone signal onto the laser (up to the bandwidth of the generator or the AOM). In this work we have used the Keysight Trueform Series model 33622A, which provides 10^9 samples per second and 64 Mbyte of storage. This allows not only to program the various composite drives but also to add more complex schemes such as dynamic decoupling and parity rotation pulses which are coherent with the gate drive.

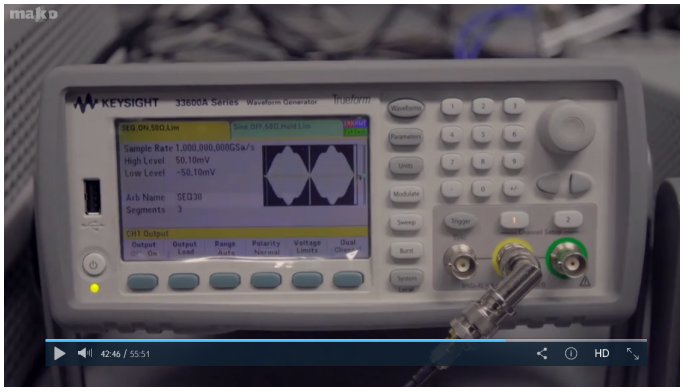

Figure 23: Arbitrary waveform generator (Keysight 33622A) used to modulate a multi-tone drive to the 674 nm laser as aired by "Eretz Nehederet" on season 15 episode 1 (Mako, 2017). The screen shows a 4 component drive (creating the hill like shape), with a dynamic decoupling pulse in the middle of the gate (short rectangle) and a parity rotation pulse at the end (an additional rectangle pulse)

4 Experiments and results

We discuss briefly the calibration procedure required to produce the different entangling gates. Then we provide the main experimental result of this work - time scans and fidelity scans of various composite entangling gate schemes (Cardioid, Antioid, CarNu etc), at different conditions (high\low $\bar{n}$, strong\weak carrier coupling). Finally, we show the measured non linearity and an active correction which improves the result for Cardioid $(1,2)$.

4.1 Calibration procedure

In order to execute a Cardioid (or any other entangling gate described above) we need to determine the the driving frequencies $\{\omega_{eg} \pm (\nu + n_i\xi_0)\}_{i=1}^{N}$, that is a set of pairs such that ω_{eg} is the carrier frequency (in this case for the $5S_{\frac{1}{2},m=-\frac{1}{2}} \rightarrow 4D_{\frac{5}{2},m=-\frac{3}{2}}$ transition), ν is the harmonic trap frequency (in this case of the center of mass mode) and ξ_0 is the fundamental symmetric detuning such that $\xi_0 = \frac{1}{T}$. The n_i specify the degrees of freedom from which the relative amplitudes are directly determined (by solving the relevant Vandermonde matrix, see 2.5).

The calibration procedure consists of measuring the carrier frequency ω_{eg} by using a carrier transition. Similarly, by measuring blue side-band frequency $\omega_{bsb} = \omega_{eg} + \nu$, we extract the trapping frequency $\nu = \omega_{bsb} - \omega_{eg}$.

We then scan the symmetric detuning ξ by initializing two ions to $|SS\rangle$ and driving them with the driving fields specified by $\{\omega_{eg} \pm (\nu + n_i\xi)\}_{i=1}^{N}$ for time $T = \frac{1}{\xi}$ and measure the population P_{SS}, P_{DD}. From the analytic expression we note that:

$$G\left(\frac{\xi}{\xi_0}\right) \equiv P_{SS} - P_{DD} = \cos\left(\frac{\pi}{2}\left(\frac{\xi_0}{\xi}\right)^2\right) \tag{122}$$

Where $\xi_0 = 2\eta\Omega$ is the "correct" symmetric detuning and ξ is the scanned value. We note that this relation is independent of choice of $\bar{n}$, N, n_i or relative phases (that is, Cardioid, Antioid or any general gate), thus fitting the measurements to this relation is a good way to determine the desired ξ_0. In practice we use the normalized

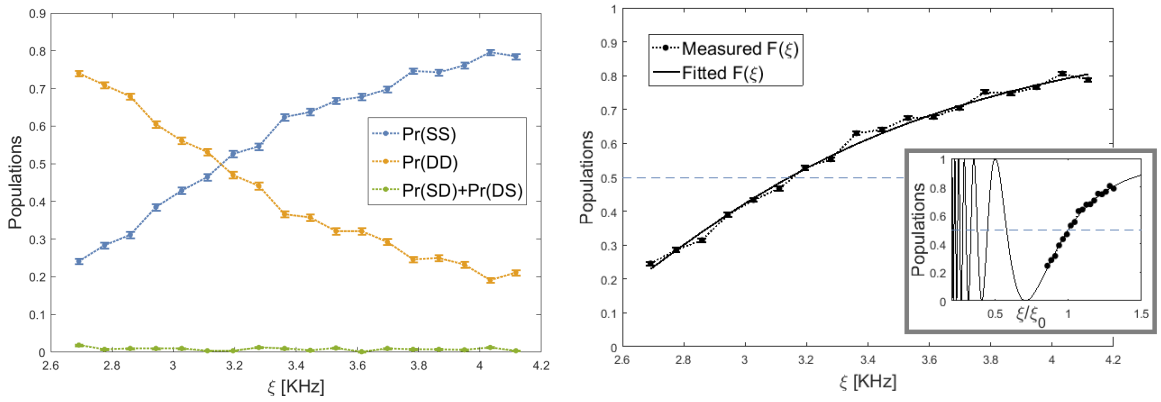

Figure 24: **Example of typical symmetric detuning calibration,** in this case of Cardioid $(2,3)$. **Left:** Populations as a function of ξ for interaction time $T = \frac{1}{\xi}$. We note the populations cross at approximately 50%-50% population of $|SS\rangle$ (blue) and $|DD\rangle$ (orange), the value of ξ at that point is ξ_0. We note that even though we do not expect motional population some nevertheless exists. Error bars reflect binomial noise due to 800 measurements at each frequency point. **Right:** Calculated $F(\xi)$ (solid) and fit (dashed) for the measured data (using robust bi-square method). Fitted symmetric detuning is $\xi_0 = 3.14 \pm 0.02$ KHz with $R^2 > 0.99$. In the inset we present a wider range of $F(\xi)$ (extrapolated according to theory).

quantity:

$$F\left(\frac{\xi}{\xi_0}\right) \equiv \frac{P_{SS} - P_{DD}}{P_{SS} + P_{DD}} = \cos\left(\frac{\pi}{2}\left(\frac{\xi_0}{\xi}\right)^2\right) \tag{123}$$

Which tends to be less sensitive to errors which are symmetric in $|SS\rangle$ and $|DD\rangle$ (such as off resonance carrier coupling or time errors due to errors in measuring ν). An example for such a measurement is shown in Fig. 24 (left). We note that while the theory predict no motion throughout the scan, there is nevertheless some population in $|SD\rangle$ and $|DS\rangle$. In addition the measured and fitted curves for $F(\xi)$ are shown (right).

Next we calibrate the anti-symmetric detuning. This calibration is required since when activating the driving fields off-resonance couplings to far energy levels cause AC Stark shifts, which in turn causes ω_{eg} to change slightly from the measured carrier transition. To account for this effect we simply add a synthetic anti-symmetric detuning δ such that in total we have $\omega_{r_i,b_i} = \omega_{eg} \pm (\nu + n_i\xi_0) + \delta - \delta_{AC}$, where δ and δ_{AC} are the synthetic and AC Stark shift anti-symmetric detuning respectively. We then scan δ while measuring the populations at interaction time $t = 2T = \frac{2}{\xi_0}$. When $\delta = \delta_{AC}$ such an interaction should cause a flip from $|SS\rangle$ to $|DD\rangle$, however when $\delta \neq \delta_{AC}$ the interaction causes excitation of $|SD\rangle$ and $|DS\rangle$ - thus we look for a fringe around $\delta = \delta_{AC}$ and fit a phenomenological Gaussian to it. A typical example for such a calibration is shown in Fig. 25.

One may interlace symmetric & anti-symmetric calibrations a few times, in this procedure we preform two cycles of such calibrations and preform a carrier calibration before each one in order to compensate for laser field frequency drifts and magnetic field slow noise.

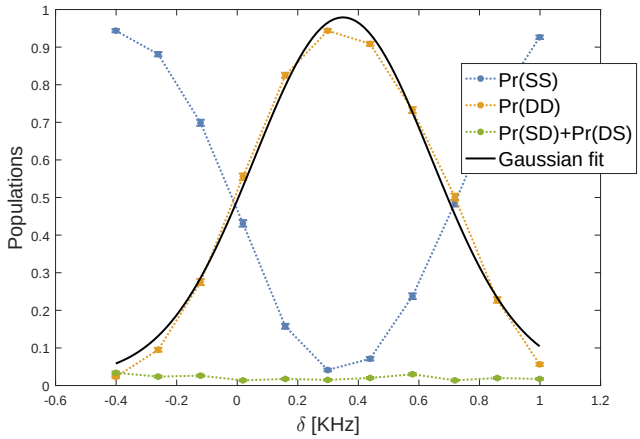

Figure 25: **Example of typical anti-symmetric calibration, in this case of Cardioid** $(2,3)$**.** We note the the population of $|DD\rangle$ peaks (orange) as the population of $|SS\rangle$ is minimized. We fit a phenomenological Gaussian (using robust bi-square method) to the population of $|DD\rangle$ such that the center of the Gaussian is the calibrated δ (black), in this example we obtain $\delta = 0.34 \pm 0.02$ KHz with $R^2 > 0.99$. Error bars reflect binomial noise due to 800 measurements at each frequency point.

4.2 Time scans

Fig. 26 shows the evolution of different Cardioid schemes in comparison to the MS and Antioid gates. All are obtained after performing the calibration procedure described above and by using ground state cooling such that $\bar{n} \approx 0.17$. We notice that as we use more spectral components the flatness around the gate time is increased (in all populations), which means that the robustness to gate timing-errors is increased. We also note that even though the Antioid $(2,3)$ and Cardioid $(2,3)$ have the same power spectral density, they do not create the same response - the Antioid has sharp features and is much more sensitive, which indicates that the effect is coherent.

As mentioned in the theoretical part, for a large $\bar{n}$ the gates show a steep response (the dependence on $\bar{n}$ is exponential). Indeed Fig. 27 shows population evolution where the ions were only Doppler cooled and not ground state cooled (for consistency this includes the calibration procedure as well). The drive used for these schemes is exactly that of Fig. 26, however this exponential dependence causes the curves to be very different. Nevertheless, the basic robustness properties and comparison between different gates remains the same.

In addition we measured similar population evolution scans for the CarNu $(2,3,7)$ gate, shown in Fig. 28. This scheme has a gate timing-error robustness similar to that for the Cardioid $(2,3)$, which is combined with robustness to harmonic frequency error.

4.3 Fidelity scans

In order to measure the gate fidelity we need to obtain the density matrix elements: $\rho_{SS,SS}$, $\rho_{DD,DD}$ and $\rho_{SS,DD}$, that is two populations and a coherence term. The time scans (above) provide the populations, however the coherence term is obtained by a parity measurement. As described (and first implemented) in [23], this is done by performing the entangling gate and then a global $\frac{\pi}{2}$ pulse right after it with a phase ϕ. By scanning the phase ϕ

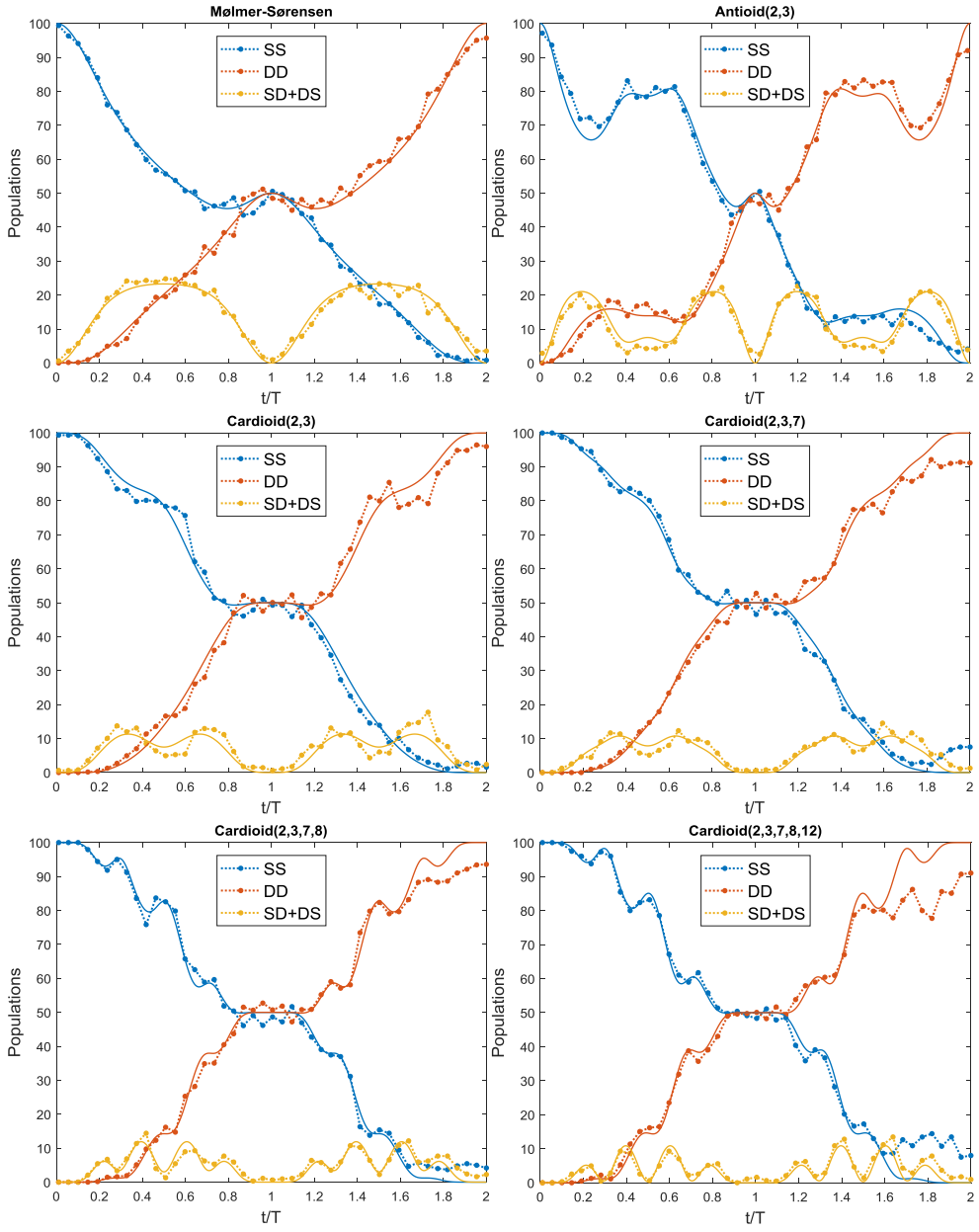

Figure 26: **Population evolution of Cardioid schemes.** All data (points connected by dashed line) are obtained by performing each measurement 625 time (2% projection noise at 50% population), theoretical curves (thin solid lines) are without any fitting parameters. All schemes are valid entangling gates, therefore at $t = T$ the SS and DD populations are at 50% and the SD and DS are at 0. The MS gate (top left) is the benchmark for all other schemes. The Antioid $(2, 3)$ (top right) shows a steep approach to the entanglement point, which causes it to be sensitive to gate timing-errors, however the Cardioid $(2, 3)$ (middle left) has the same spectral components but shows an increased flatness around gate time, which shows that the robustness is a coherent effect determined by the phase difference of the different components and cannot be explained only by power spectral density. As we use more harmonic components we create a more flat response, as seen in the Cardioid $(2, 3, 7)$ (middle right), Caridoid $(2, 3, 7, 8)$ (bottom left) and Cardioid $(2, 3, 7, 8, 12)$ (bottom right). We also note that the maximal population of SD and DS decreases, this is because the phase space trajectory becomes more centered around the origin.

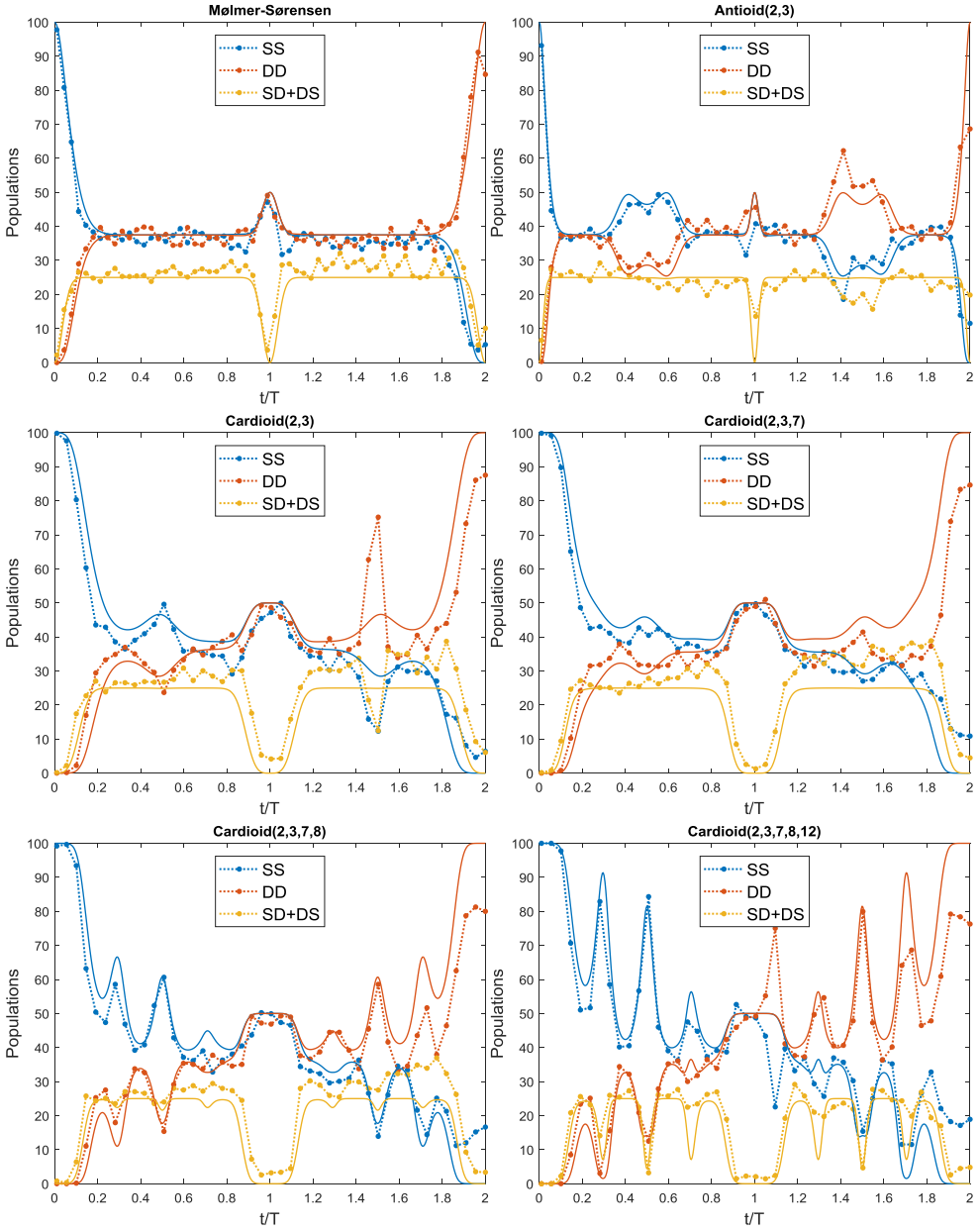

Figure 27: **Population evolution of "hot" Cardioid gates at $\bar{n} \approx 9.8$.** All data (points connected by dashed line) are obtained by performing each measurement 625 time (2% projection noise at 50% population), theoretical curves (thin solid lines) are without any fitting parameters. All schemes are valid entangling gates, therefore at $t = T$ the SS and DD populations are at 50% and the SD and DS are at 0. The gates shown here are exactly those shown in 26, however the curves are very different due to the strong dependence on temperature. Nevertheless the same robustness properties described in the "cold" gates are valid here as well here.

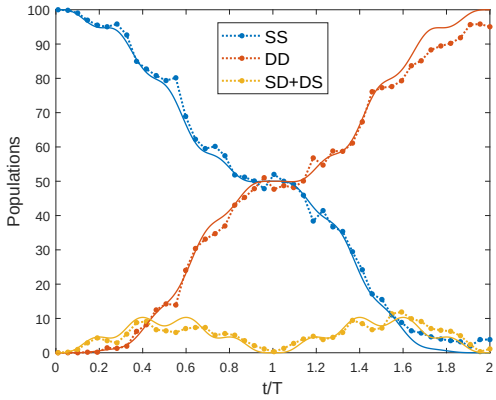

Figure 28: **Population evolution of CarNu** $(2,3,7)$**.** All data (points connected by dashed line) are obtained by performing each measurement 625 time (2% projection noise at 50% population), theoretical curves (thin solid lines) are without any fitting parameters. This gate has gate timing-error robustness properties similar to those of Cardioid $(2,3)$ and in addition robustness to harmonic trap frequency error.

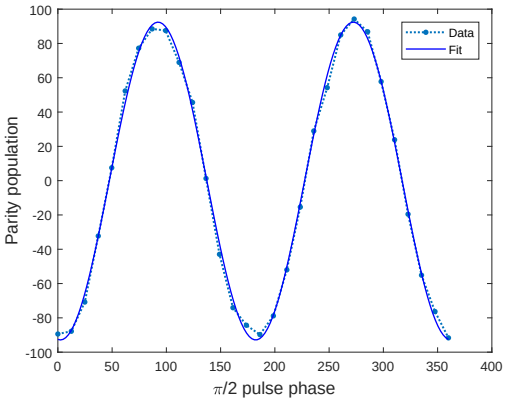

Figure 29: **Parity fringe.** Data (points connected by dashed line) are obtained by performing each measurement 625 time (2% projection noise at 50% population), fit is to $A\sin(2\phi+\phi_0)+c$. This is an oscillation of the even parity populations $\rho_{SS,SS}+\rho_{DD,DD}$ and the odd parity populations $\rho_{SD,SD}+\rho_{DS,DS}$. Complemented by the populations at gate time we evaluate this example with a fidelity of $F\approx 95.5\%$. To obtain fidelity as a function of some parameter (such as gate timing-error) we scan an interval of this parameter and obtain such a parity curve and population information at each point.

we generate oscillations between $\rho_{SS,SS}+\rho_{DD,DD}$ and $\rho_{SD,SD}+\rho_{DS,DS}$ which is known as a *parity fringe*. The fidelity is then given by $F_g=\frac{1}{2}\left(\rho_{SS,SS}+\rho_{DD,DD}\right)+\frac{1}{4}A$ where A is the contrast of the obtained parity fringe. Such a parity scan is shown in Fig. 29:

To demonstrate the robustness to gate timing-error we scan the gate time around $\delta t=0$ (which simulates a gate time implementation error) and measure the fidelity by the method described above. Fig. 30 shows the results of such scans for hot and cold scenarios.

To demonstrate the robustness to harmonic trap frequency we scan the harmonic trap frequency error around $\delta\nu=0$. Such a scan is shown in Fig. 31, where it is seen that the CarNu $(2,3,7)$ has the most robust response. As mentioned in the theoretical section this robustness is not in an order-by-order manner, but rather the prefactor of the leading quadratic dependence. However, for gate purity the improvement is order by order as is shown in the

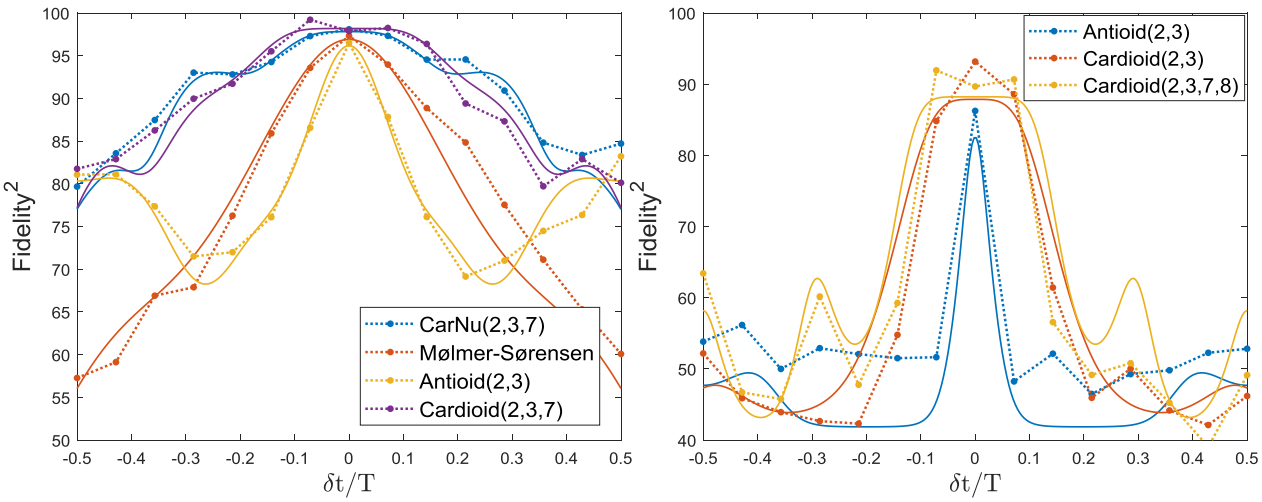

Figure 30: **Gate timing-error robustness scan.** All data (points connected by dashed line) are obtained by performing each measurement 625 time (2% projection noise at 50% population), fits (thin solid lines) are by allowing rescaling and shift of the theoretical response. **Left:** Robustness of different schemes in a cold ($\bar{n} \approx 0.17$) scenario. Clearly the CarNu $(2,3,7)$ (which has 2nd order gate timing-error robustness) and the Cardioid $(2,3,7)$ (which has 3rd order gate timing-error robustness) show a distinct improvement on the MS scheme. **Right:** Robustness of different schemes in a hot ($\bar{n} \approx 9.8$) scenario. Due to the exponential appearance of $\bar{n}$ in the fidelity function the features are much narrower than the cold scenario, however the flatness of the Cardioid schemes remains obvious.

figure as well.

4.4 Off resonance carrier coupling

The improvement in fidelity due to diminishing direct off resonance carrier coupling is measured as well. To enhance the effect we first tuned the trap frequency to ~ 500 KHz such that $\frac{\Omega}{\nu} \approx 5\%$, which corresponds to $\sim 2\%$ infidelities in the standard MS entanglement schemes. Then we measured a time scan of both the MS gate and the Cardioid $(2,3)$ where we paid special attention to the initial and final moments of the gate. As easily seen in Fig. 32, the MS scheme is prone to carrier oscillations which are seen at the initial times of the gate (with 2% contrast) and also at the gate time (where they are less distinct since the gate evolution has also kicked in and in addition projection noise is also at a 2% level). However the Cardioid scheme does not show these oscillations at all, which results in a better entanglement procedure (seen as less population in the SD and DS states).

4.5 Third order non-linearity

As discussed in the theory section, using a Cardioid $(1,2,3,...)$ drive will create an on resonance side-band drive due to non-linearity of the various RF devices used (see 2.8). This effect was measured with two approaches. First, the RF was measured directly using a spectrometer before and after the RF amplifier. In Fig. 33 (left) we observe the spectrum of the RF modulating signal for the Cardioid $(1,2)$ before amplification, while after amplification (right) we observe two additional spectral components due to third order non-linear effects of the RF amplifier, one of these new components corresponds to an on-resonance side-band excitation and the other is negligible.

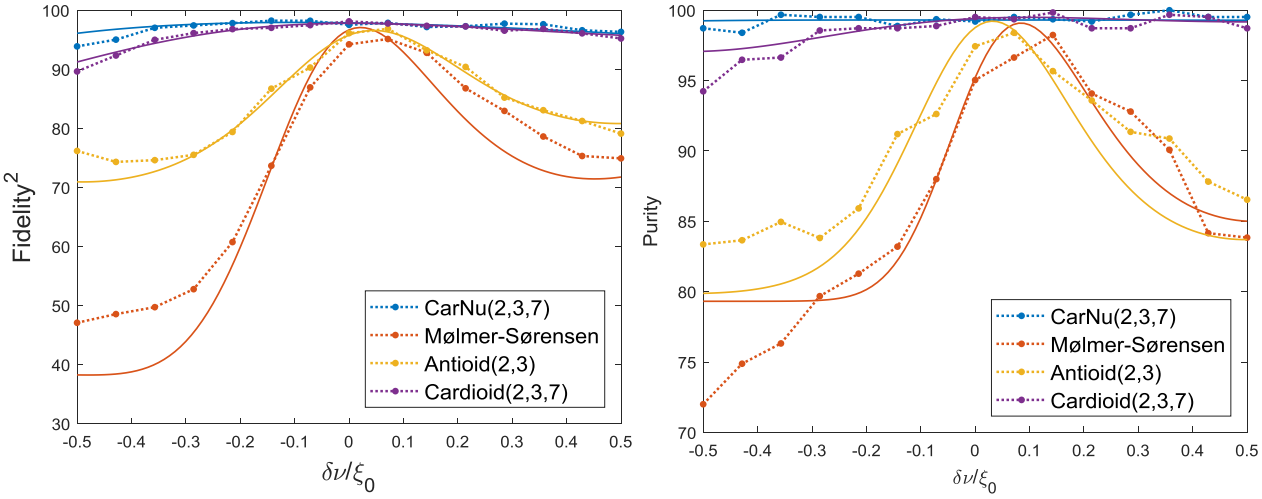

Figure 31: **Harmonic trap error fidelity scan.** All data (points connected by dashed line) are obtained by performing each measurement 625 time (2% projection noise at 50% population), fits (thin solid lines) are by allowing rescaling and shift of the theoretical response. **Left:** Fidelity of different schemes in a cold ($\bar{n} \approx 0.17$) scenario. Clearly the CarNu $(2,3,7)$ (which has 2nd order robustness) shows the best robustness however it is still quadratic in the error. We note that Cardioid $(2,3,7)$ also shows a flat response, this similarity to CarNu $(2,3,7)$ is since the optimization is on the prefactor of the leading quadratic dependence, which corresponds to a less pronounced effect. **Right:** Purity of different schemes. Here the CarNu $(2,3,7)$ purity error scales as $\left(\frac{\delta\nu}{\xi_0}\right)^4$ while the error is quadratic for all other schemes, and the advantage over Cardioid $(2,3,7)$ is clearer.

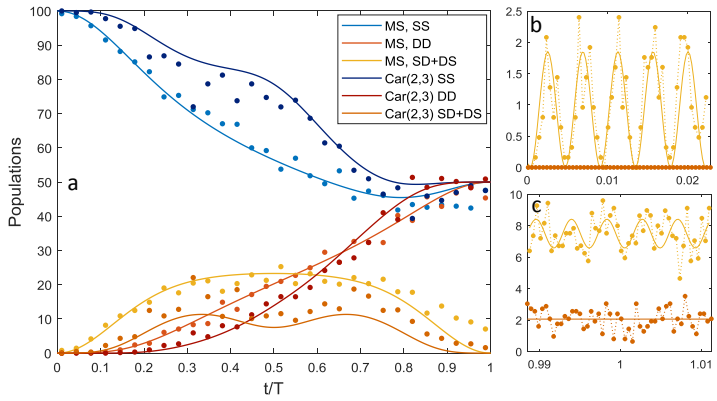

Figure 32: **Off resonance carrier coupling.** All data (points connected by dashed line) are obtained by averaging 625 measurements each (2% projection error at 50% probability). **(a)** Population evolution scan of a standard MS gate, Cardioid(2,3) gate and analytic evolution (solid) with no fitting parameters. Here $\frac{\Omega}{\nu} \sim 5\%$ which corresponds to a $\sim 2\%$ infidelity for the standard scheme and $\sim 0.1\%$ for the Cardioid(2,3) scheme. This is seen by the fact that the combined motional populations, SD and DS (yellow for MS, orange for Cardioid(2,3)), do not return to 0 at the gate time. **(b)** Shows a zoom-in scan on the initial part of the gate evolution of the motional populations combined. The carrier oscillations are easily observed in the MS gate (yellow points), their amplitude is heuristically fitted to off-resonance Rabi oscillations, $A_{t=0}\sin^2\left(\tilde{\Omega}t\right)$, with an effective Rabi frequency of $\tilde{\Omega} = \sqrt{\Omega^2+\nu^2}$ (solid yellow). For the Cardioid $(2,3)$ no oscillations are apparent (orange points) **(c)** Shows a zoom-in on the evolution around gate time of the motional populations combined. Here the oscillations are less distinct since the projection noise is at equal footing with them. We extend the previous fit by adding a constant, $A_{t=0}\sin^2\left(\tilde{\Omega}t\right) + C_{t=T}$ (solid lines). The MS gate (yellow points) now oscillates around $C_{t=T} = 8\%$. The Cardioid(2,3) drive results in significantly less of the motional populations (orange points) which oscillates around $C_{t=T} = 2\%$ (orange solid). This corresponds directly to increased gate fidelity.

Figure 33: **Example of 3rd order non linear signature of RF amplifier**. **Left:** Spectrum of the blue side of the RF modulating signal for the Cardioid $(1, 2)$ measured after combining 4 DDS signals and before amplification. In this example we have $\omega + \nu = 85$ MHz and $\xi = 0.008$ MHz (these numbers were chosen arbitrarily), such that we observe $\omega_{b_1} = \omega + \nu + \xi_0$ as the left peak and $\omega_{b_2} = \omega + \nu + 2\xi_0$ as the right peak, both with an amplitude of ~ -10 dBm. **Right:** Same spectrum as but measured after RF amplification. Two new components appear: $\omega_{3,1} = 2\omega_{b_1} - \omega_{b_2} = 85$ MHz (left-most), and $\omega_{3,2} = 2\omega_{b_2} - \omega_{b_1} = 85.024$ MHz (right-most) which are $40dBm$ lower than the original driving fields. We note that $\omega_{3,1} = \omega + \nu$ and thus creates on resonance blue side-band excitations.

Next, we conducted a Rabi time scan experiment where the ion was interrogated with a drive detuned by δ from its carrier transition and the shelving efficiency was measured, we then repeated the experiment with detuning 2δ, and finally conducted the experiment with both δ and 2δ present (and non-linear effect due to RF amplification). We have made sure that $\delta \gg \Omega$ such that any measured response cannot be attributed to power broadening mechanisms. Fig. 34 shows the result of these three scenarios - notably both δ and 2δ do not effectively excite any population on their own, however combined we see a considerable build up of population from which we estimate $\Omega_3 \approx \frac{1}{5}\Omega$, where Ω is the on resonance Rabi frequency and Ω_3 is the non-linear component Rabi frequency. This again shows that the non-linear term has a significant effect. easily measurable on the ions.

As mentioned in the theoretical section, another possibility for negating this non-linear effect is by actively compensating the unwanted responses (by adding a components with an opposite phase). This was done as well but showed less stability, therefore to really employ such a correction a feedback mechanism needs to be put in place. Here we show a Cardioid $(1, 2)$ gate which was obtained by calibrating a feed forward correction to the non-linear response. Fig. 35 shows the gate evolution and gate timing-error fidelity scan obtained, which shows a good fit to the theory.

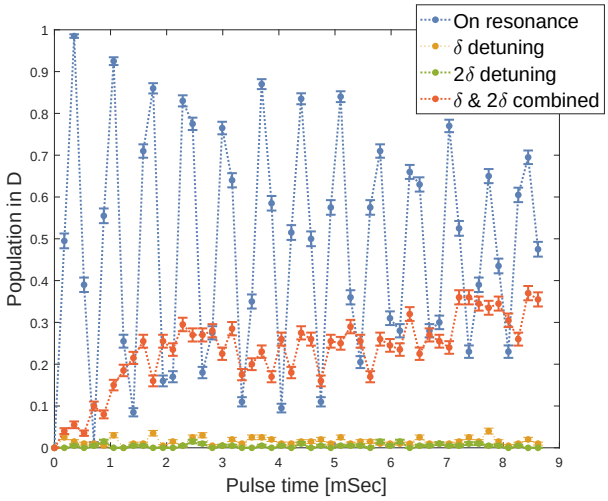

Figure 34: **Non-linear effects of RF amplifier as measured on ion.** When scanning the interrogation time of an on resonance drive (blue) Rabi oscillations occur with a Rabi frequency of $\Omega \approx 700$ Hz (exact value is unimportant). When scanning with a drive detuned by δ (orange) or 2δ (green) no significant population is excited and the coupling is effectively 0. Combining the two drives one naively expects that the result at most will be a sum of the two drives however due to non-linear effect of the RF amplifier an on-resonance components is created which creates a significant excitation (red). Here $\delta = 8$ KHz $\gg \Omega$ such that no power broadening is expected. By comparing the pulse time needed to excite 10% of the population (that is in the linear regime of the response) we may estimate that ratio between the non-linear component and on resonance Rabi frequencies: $\frac{\Omega_3}{\Omega} \approx \frac{1}{5}$. The data is notably noisy due to the long interrogation times, nevertheless the effect of the non-linear components is significant and easily observed. Error bars represent binomial noise due to 200 measurements at each time point.

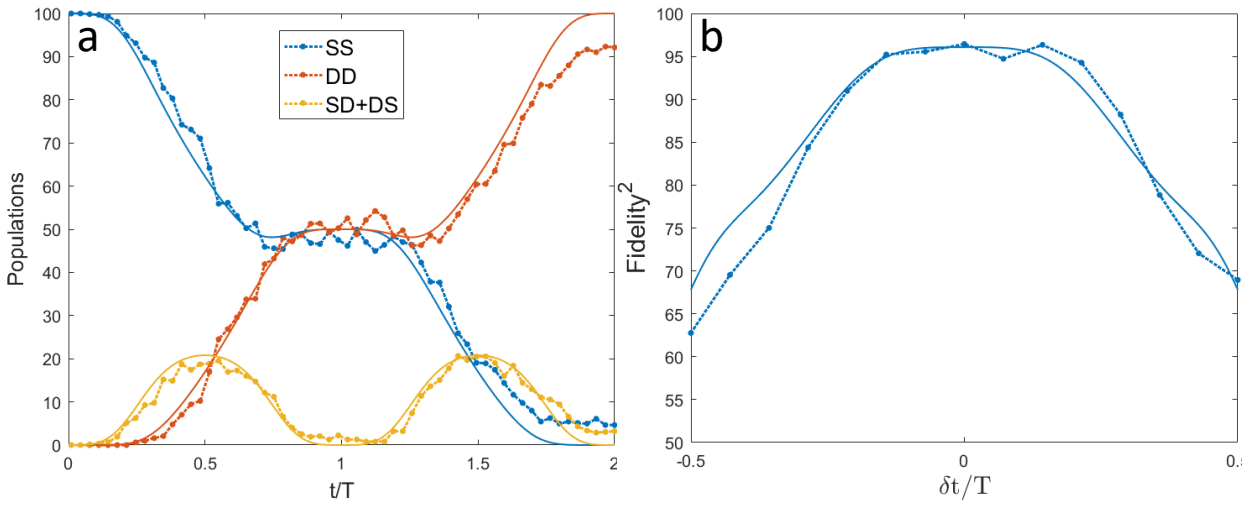

Figure 35: **Cardioid(1,2) using active non-linear compensation method.** All data (points connected by dashed line) are obtained by averaging 625 measurements each (2% projection error at 50% probability). **Left:** Population evolution scan of Cardioid(1,2) while using active compensation of third order non-linear response. Theoretical curves (solid thin lines) are without any fitting parameters. The gate evolution is well behaved and fits the theory, nevertheless some decoherence-like effect are seen around $t = 2T$ as the motion does not return to 0. **(b)** Cardioid(1,2) fidelity to gate timing-error. Fit (solid thin line) is obtained by allowing rescaling of the theoretical response. The fidelity flattens around the gate time but reaches only 96.45%, probably due to non-linear effects which still persist.

5 Summary

In this work we have derived and demonstrated methods for creating entangling gates which are robust to different error mechanisms. Our main result, the CarNu $(2, 3, 7)$ is a two-qubit entangling gate which is robust to gate timing-errors, harmonic trap frequency errors and off-resonance carrier coupling. From a broader point of view, we introduced a methodology which treats the different spectral components of the entangling scheme as degrees of freedom, which are then used to increasing the robustness of the scheme to error mechanisms of choice.

For the case of gate timing-error robustness and off-resonance carrier coupling we proposed a method for an order-by-order increase of the fidelity. And have managed to provide analytical explanations for the intuitions and methods already used today. Furthermore, we have improved on these methods by constructing schemes which do not require additional pulses and which are not prone to technical non-linear effects which are always present in RF devices. For the case of harmonic trap frequency error we are able to reduce the prefactor of the quadratic scaling of the fidelity and improve the gate purity in an order-by-order manner. Most importantly, these results are measured explicitly and easily fit the theoretical predictions. Hopefully, the methodology and experiments introduced here will allow for better realization of the exciting prospects of QIP.

References

[1] Peter W. Shor. Polynomial-Time Algorithms for Prime Factorization and Discrete Logarithms on a Quantum Computer. 41(2):303–332, 1995. URL: http://arxiv.org/abs/quant-ph/9508027{%}0Ahttp://dx.doi.org/10.1137/S0097539795293172, arXiv:9508027, doi:10.1137/S0097539795293172.

[2] T. D. Ladd, F. Jelezko, R. Laflamme, Y. Nakamura, C. Monroe, and J. L. O'Brien. Quantum computers. *Nature*, 464(7285):45–53, mar 2010. URL: http://dx.doi.org/10.1038/nature08812http://www.nature.com/doifinder/10.1038/nature08812, arXiv:1009.2267, doi:10.1038/nature08812.

[3] David P. DiVincenzo. The Physical Implementation of Quantum Computation. *Fortschritte der Physik*, 48(9-11):771–783, sep 2000. URL: http://arxiv.org/abs/quant-ph/0002077{%}0Ahttp://dx.doi.org/10.1002/1521-3978(200009)48:9/11{%}3C771::AID-PROP771{%}3E3.0.CO;2-Ehttp://arxiv.org/abs/1708.08039http://doi.wiley.com/10.1002/1521-3978{%}28200009{%}2948{%}3A9{%}2F11{%}3C771{%}3A{%}3AAID-PROP771{%}3E3.0.CO{%}3B2-E, arXiv:1708.08039, doi:10.1002/1521-3978(200009)48:9/11<771::AID-PROP771>3.0.CO;2-E.

[4] A. Yu. Kitaev. Quantum computations: algorithms and error correction. *Uspekhi Mat. Nauk*, 52(6):53–112, 1997. URL: http://mi.mathnet.ru/rm892, doi:10.4213/rm892.

[5] Dorit Aharonov and Michael Ben-Or. Fault-Tolerant Quantum Computation with Constant Error Rate. *SIAM Journal on Computing*, 38(4):1207–1282, jan 2008. URL: http://arxiv.org/abs/quant-ph/9906129http://epubs.siam.org/doi/10.1137/S0097539799359385, arXiv:9906129, doi:10.1137/S0097539799359385.

[6] R. Shaniv, N. Akerman, and R. Ozeri. Atomic quadrupole moment measurement using dynamic decoupling. *Physical Review Letters*, 116(14):1–5, 2016. arXiv:1511.07277, doi:10.1103/PhysRevLett.116.140801.

[7] Ravid Shaniv and Roee Ozeri. Quantum Lock-in Force Sensing using Optical Clock Doppler Velocimetry. *ArXiv e-prints arXiv:1602.08645*, 8:1–11, 2016. URL: http://arxiv.org/abs/1602.08645{%}0Ahttp://dx.doi.org/10.1038/ncomms14157, arXiv:1602.08645, doi:10.1038/ncomms14157.

[8] Ravid Shaniv, Tom Manovitz, Yotam Shapira, Nitzan Akerman, and Roee Ozeri. Heisenberg-limited Rabi spectroscopy. pages 1–18, 2017. arXiv:arXiv:1708.02743v1.

[9] P. O. Schmidt. Spectroscopy Using Quantum Logic. *Science*, 309(5735):749–752, jul 2005. URL: http://www.sciencemag.org/cgi/doi/10.1126/science.1114375, doi:10.1126/science.1114375.

[10] P. O. Schmidt, T. Rosenband, J. C J Koelemeij, D. B. Hume, W. M. Itano, J. C. Bergquist, and D. J. Wineland. Spectroscopy of atomic and molecular ions using quantum logic. *AIP Conference Proceedings*, 862:305–312, 2006. doi:10.1063/1.2387937.

[11] R. Gerritsma, G. Kirchmair, F. Zähringer, E. Solano, R. Blatt, and C. F. Roos. Quantum simulation of the Dirac equation. *Nature*, 463(7277):68–71, 2010. URL: http://www.nature.com/doifinder/10.1038/nature08688, arXiv:arXiv:0909.0674v1, doi:10.1038/nature08688.

[12] Michael Johanning, Andrés F Varón, and Christof Wunderlich. Quantum simulations with cold trapped ions. *Journal of Physics B: Atomic, Molecular and Optical Physics*, 42(15):154009, aug 2009. URL: http://www.nature.com/doifinder/10.1038/nphys2252http://arxiv.org/abs/0905.0118http://dx.doi.org/10.1088/0953-4075/42/15/154009http://stacks.iop.org/0953-4075/42/i=15/a=154009?key=crossref.0f4ea245ed663cbd9cce633bfb5c4894, arXiv:0905.0118, doi:10.1088/0953-4075/42/15/154009.

[13] Christian F. Roos. Ion trap quantum gates with amplitude-modulated laser beams. *New Journal of Physics*, 10(1):013002, jan 2008. URL: http://stacks.iop.org/1367-2630/10/i=1/a=013002?key=crossref.0cd67d9408fea34e2d258aeb1f179ffd, arXiv:0710.1204, doi:10.1088/1367-2630/10/1/013002.

[14] G. Kirchmair, J. Benhelm, F. Zähringer, R. Gerritsma, C. F. Roos, and R. Blatt. Deterministic entanglement of ions in thermal states of motion. *New Journal of Physics*, 11, 2009. arXiv:0810.0670, doi:10.1088/1367-2630/11/2/023002.

[15] M. Palmero, S. Martínez-Garaot, D. Leibfried, D. J. Wineland, and J. G. Muga. Fast phase gates with trapped ions. *Physical Review A*, 95(2):022328, feb 2017. URL: https://link.aps.org/doi/10.1103/PhysRevA.95.022328, arXiv:1609.01892, doi:10.1103/PhysRevA.95.022328.

[16] V. M. Schäfer, C. J. Ballance, K. Thirumalai, L. J. Stephenson, T. G. Ballance, A. M. Steane, and D. M. Lucas. Fast quantum logic gates with trapped-ion qubits. pages 1–6, sep 2017. URL: http://arxiv.org/abs/1709.06952, arXiv:1709.06952.

[17] J. D. Wong-Campos, S. A. Moses, K. G. Johnson, and C. Monroe. Demonstration of two-atom entanglement with ultrafast optical pulses. 20742, 2017. URL: http://arxiv.org/abs/1709.05179, arXiv:1709.05179.

[18] Pak Hong Leung, Kevin A. Landsman, Caroline Figgatt, Norbert M. Linke, Christopher Monroe, and Kenneth R. Brown. Robust two-qubit gates in a linear ion crystal using a frequency-modulated driving force. (0):1–8, aug 2017. URL: http://arxiv.org/abs/1708.08039, arXiv:1708.08039.

[19] Klaus Mølmer and Anders Sørensen. Multiparticle Entanglement of Hot Trapped Ions. *Physical Review Letters*, 82(9):1835–1838, mar 1999. URL: https://link.aps.org/doi/10.1103/PhysRevLett.82.1835, arXiv:9810040, doi:10.1103/PhysRevLett.82.1835.

[20] Anders Sørensen and Klaus Mølmer. Entanglement and quantum computation with ions in thermal motion.

Physical Review A, 62(2):022311, jul 2000. URL: https://link.aps.org/doi/10.1103/PhysRevA.62.022311, arXiv:0002024, doi:10.1103/PhysRevA.62.022311.

[21] Nitzan Akerman. *Trapped ions and free photons*. PhD thesis, Weizmann Institute of Science, 2012.

[22] J I Cirac and P Zoller. Quantum computations with trapped ions. *Physical Review Letters*, 74(20):4091–4094, 1995. doi:10.1002/1521-3978(200009)48:9/11<785::AID-PROP785>3.0.CO;2-V.

[23] C. A. Sackett, D. Kielpinski, B. E. King, C. Langer, V. Meyer, C. J. Myatt, M. Rowe, Q. A. Turchette, W. M. Itano, D. J. Wineland, and C. Monroe. Experimental entanglement of four particles. *Nature*, 404(6775):256–9, 2000. arXiv:0312197, doi:10.1038/35005011.

[24] Michael A. Nielsen and Isaac L. Chuang. *Quantum Computation and Quantum Information*. Cambridge University Press, Cambridge, 2010. URL: http://ebooks.cambridge.org/ref/id/CBO9780511976667, doi:10.1017/CBO9780511976667.

[25] André Eckardt and Egidijus Anisimovas. High-frequency approximation for periodically driven quantum systems from a Floquet-space perspective. *New Journal of Physics*, 17(9):93039, 2015. URL: http://dx.doi.org/10.1088/1367-2630/17/9/093039, arXiv:1502.0647, doi:10.1088/1367-2630/17/9/093039.

[26] Saar Rahav, Ido Gilary, and Shmuel Fishman. Effective Hamiltonians for periodically driven systems. *Physical Review A*, 68(1):013820, 2003. URL: http://arxiv.org/abs/nlin/0301033{%}5Cnhttp://link.aps.org/doi/10.1103/PhysRevA.68.013820, arXiv:0301033, doi:10.1103/PhysRevA.68.013820.

[27] Toby Cubitt. Partial trace: TrX, 2009. URL: http://www.dr-qubit.org/matlab.html.

[28] Ravid Shaniv. *Spectral noise analysis of a narrow line-width laser using a single trapped ion*. PhD thesis.

[29] S. Blanes, F. Casas, J. A. Oteo, and J. Ros. A pedagogical approach to the Magnus expansion. *European Journal of Physics*, 31(4):907–918, 2010. URL: http://iopscience.iop.org/0143-0807/31/4/020{%}5Cnhttp://iopscience.iop.org/0143-0807/31/4/020/pdf/0143-0807{_}31{_}4{_}020.pdf{%}5Cnhttp://stacks.iop.org/0143-0807/31/i=4/a=020?key=crossref.d5162f9835893478accab28c1a5d2cb3, doi:10.1088/0143-0807/31/4/020.

[30] G. Szegö. *Orthogonal Polynomials*, volume XXIII. 1975. URL: http://catalog.enu.kz:55555/guid/246D7239-1B5D-42CA-A07F-EA66E8E8040F.pdf, doi:0821810235.

6 Appendix

6.1 Mølmer-Sørensen gate

6.1.1 Interaction Hamiltonian

Starting with:

$$\begin{cases} \hat{H}_0 = \nu\left(\hat{a}^\dagger\hat{a} + \frac{1}{2}\right) + \sum_i \omega_{eg}\frac{\hat{\sigma}_z^{(i)}}{2} \\ \hat{V} = \hat{V}\left(\omega_r\right) + \hat{V}\left(\omega_b\right) \\ \hat{V}\left(\omega\right) = \sum_i \frac{\hbar\Omega}{2}\left[\hat{\sigma}_+^{(i)} e^{i(k\hat{x}-\omega t+\phi)}\right] + h.c \\ \eta\left(\hat{a}^\dagger + \hat{a}\right) = k\hat{x} \end{cases} \tag{124}$$

We move to an interaction picture with respect to $\hat{H}_0$ by using:

$$\begin{cases} e^{i\frac{\omega_{eg}t}{2}\hat{\sigma}_z}\hat{\sigma}_+ e^{-i\frac{\omega_{eg}t}{2}\hat{\sigma}_z} = e^{i\omega_{eg}t}\hat{\sigma}_+ \\ e^{i\nu\left(\hat{a}^\dagger\hat{a}+\frac{1}{2}\right)t} e^{i\eta\left(\hat{a}^\dagger+\hat{a}\right)} e^{-i\nu\left(\hat{a}^\dagger\hat{a}+\frac{1}{2}\right)t} = e^{i\eta\left(\hat{a}^\dagger e^{i\nu t}+\hat{a}e^{-i\nu t}\right)} \end{cases} \tag{125}$$

To obtain:

$$\hat{V}_I\left(\omega\right) = \sum_i \frac{\hbar\Omega}{2} e^{i\omega_{eg}t}\hat{\sigma}_+^{(i)} e^{i\eta\left(\hat{a}^\dagger e^{i\nu t}+\hat{a}e^{-i\nu t}\right)} e^{-i(\omega t+\phi)} + h.c \tag{126}$$

Assuming $\eta \ll 1$ (that is, that we are well within the Lamb-Dicke regime) we get:

$$\hat{V}_I\left(\omega\right) = \sum_i \frac{\hbar\Omega}{2} e^{i\omega_{eg}t}\hat{\sigma}_+^{(i)}\left(\mathbb{1} + i\eta\left(\hat{a}^\dagger e^{i\nu t} + \hat{a}e^{-i\nu t}\right)\right) e^{-i(\omega t+\phi)} + h.c + \mathcal{O}\left(\eta^2\right) \tag{127}$$

$$= \sum_i \frac{\hbar\Omega}{2}\hat{\sigma}_+^{(i)}\left(e^{i(\omega_{eg}-\omega)t} + i\eta\left(\hat{a}^\dagger e^{i(\omega_{eg}-\omega+\nu)t} + \hat{a}e^{-i(\omega-\omega_{eg}+\nu)t}\right)\right) e^{-i\phi} + h.c + \mathcal{O}\left(\eta^2\right) \tag{128}$$

We define the red and blue detuned frequencies as:

$$\begin{cases} \omega_r = \omega_{eg} - \nu - \xi + \delta \\ \omega_b = \omega_{eg} + \nu + \xi + \delta \end{cases} \tag{129}$$

Where ξ is the symmetric detuning and δ is the anti-symmetric detuning. Using a rotating wave approximation we may eliminate terms that rotate master than ν. For the red detuned laser:

$$\hat{V}_I^{RWA}\left(\omega_r\right) = \frac{\hbar\eta\Omega}{2} i\sum_i\left(\hat{\sigma}_+^{(i)}\hat{a}e^{-i(-\xi+\delta)t}e^{-i\phi} - \hat{\sigma}_-^{(i)}\hat{a}^\dagger e^{i(-\xi+\delta)t}e^{i\phi}\right) \tag{130}$$

Similarly, for the blue detuned

$$\hat{V}_I^{RWA}(\omega_b) = \frac{\hbar\eta\Omega}{2} i \sum_i \left(\hat{\sigma}_+^{(i)} \hat{a}^\dagger e^{-i(\xi+\delta)t} e^{-i\phi} - \hat{\sigma}_-^{(i)} \hat{a} e^{i(\xi+\delta)t} e^{i\phi} \right) \tag{131}$$

Combining the two we get:

$$\hat{V}_I = \frac{\hbar\eta\Omega}{2} \sum_i \left[i\hat{\sigma}_+^{(i)} e^{-i\phi} \left(\hat{a} e^{-i(\delta-\xi)t} + \hat{a}^\dagger e^{-i(\delta+\xi)t} \right) + h.c \right] \tag{132}$$

6.1.2 Unitary evolution solution

We aim solve Schrödinger's equation:

$$i\partial_t \hat{U} = \hat{V}_I \hat{U} \tag{133}$$

Under the initial conditions:

$$\hat{U}(t=0) = \mathbb{1} \tag{134}$$

For the on resonance standard MS gate:

$$\hat{V}_I(t) = f(t)\, \hat{J}_y \hat{x} + g(t)\, \hat{J}_y \hat{p} \tag{135}$$

We make use of the ansatz:

$$\hat{U}(t) = e^{-iA(t)\hat{J}_y^2} e^{-iF(t)\hat{J}_y\hat{x}} e^{-iG(t)\hat{J}_y\hat{p}} \tag{136}$$

Note this can also be considered as a Magnus expansion (which is derived and explained in detail in [29]), such that these are all the relevant orders due to the commutation relation:

$$\left[\hat{J}_y\hat{x}, \left[\hat{J}_y\hat{x}, \hat{J}_y\hat{p} \right] \right] = \left[\hat{J}_y\hat{p}, \left[\hat{J}_y\hat{x}, \hat{J}_y\hat{p} \right] \right] = 0 \tag{137}$$

The lhs of Schrödinger then reads:

$$\frac{\partial \hat{U}(t)}{\partial t} = -iA'(t)\, \hat{J}_y^2 e^{-iA(t)\hat{J}_y^2} e^{-iF(t)\hat{J}_y\hat{x}} e^{-iG(t)\hat{J}_y\hat{p}} \tag{138}$$

$$- ie^{-iA(t)\hat{J}_y^2} F'(t)\, \hat{J}_y\hat{x} e^{-iF(t)\hat{J}_y\hat{x}} e^{-iG(t)\hat{J}_y\hat{p}} \tag{139}$$

$$- ie^{-iA(t)\hat{J}_y^2} e^{-iF(t)\hat{J}_y\hat{x}} G'(t)\, \hat{J}_y\hat{p} e^{-iG(t)\hat{J}_y\hat{p}} \tag{140}$$

While the right hand side reads:

$$\hat{V}_I\hat{U}(t) = \left(f(t)\hat{J}_y\hat{x} + g(t)\hat{J}_y\hat{p}\right)e^{-iA(t)\hat{J}_y^2}e^{-iF(t)\hat{J}_y\hat{x}}e^{-iG(t)\hat{J}_y\hat{p}} \tag{141}$$

$$= f(t)\hat{J}_y\hat{x}e^{-iA(t)\hat{J}_y^2}e^{-iF(t)\hat{J}_y\hat{x}}e^{-iG(t)\hat{J}_y\hat{p}} + g(t)\hat{J}_y\hat{p}e^{-iA(t)\hat{J}_y^2}e^{-iF(t)\hat{J}_y\hat{x}}e^{-iG(t)\hat{J}_y\hat{p}}$$

$$= f(t)\left(\left[\hat{J}_y\hat{x}, e^{-iA(t)\hat{J}_y^2}\right] + e^{-iA(t)\hat{J}_y^2}\hat{J}_y\hat{x}\right)e^{-iF(t)\hat{J}_y\hat{x}}e^{-iG(t)\hat{J}_y\hat{p}} \tag{142}$$

$$+ g(t)\left(\left[\hat{J}_y\hat{p}, e^{-iA(t)J_y^2}\right] + e^{-iA(t)J_y^2}\hat{J}_y\hat{p}\right)e^{-iF(t)\hat{J}_y\hat{x}}e^{-iG(t)\hat{J}_y\hat{p}} \tag{143}$$

$$= f(t)e^{-iA(t)J_y^2}\hat{J}_y\hat{x}e^{-iF(t)\hat{J}_y\hat{x}}e^{-iG(t)\hat{J}_y\hat{p}} + g(t)e^{-iA(t)\hat{J}_y^2}\left(\left[\hat{J}_y\hat{p}, e^{-iF(t)\hat{J}_y\hat{x}}\right] + e^{-iF(t)\hat{J}_y\hat{x}}\hat{J}_y\hat{p}\right)e^{-iG(t)\hat{J}_y\hat{p}}$$

$$= f(t)e^{-iA(t)\hat{J}_y^2}\hat{J}_y\hat{x}e^{-iF(t)\hat{J}_y\hat{x}}e^{-iG(t)\hat{J}_y\hat{p}} + g(t)e^{-iA(t)\hat{J}_y^2}\left(-\hat{J}_y^2F(t)e^{-iF(t)\hat{J}_y\hat{x}} + e^{-iF(t)\hat{J}_y\hat{x}}\hat{J}_y\hat{p}\right)e^{-iG(t)\hat{J}_y\hat{p}}$$

$$= f(t)e^{-iA(t)\hat{J}_y^2}\hat{J}_y\hat{x}e^{-iF(t)\hat{J}_y\hat{x}}e^{-iG(t)\hat{J}_y\hat{p}} \tag{144}$$

$$- \hat{J}_y^2F(t)g(t)e^{-iA(t)\hat{J}_y^2}e^{-iF(t)\hat{J}_y\hat{x}}e^{-iG(t)\hat{J}_y\hat{p}} \tag{145}$$

$$+ g(t)e^{-iA(t)\hat{J}_y^2}e^{-iF(t)\hat{J}_y\hat{x}}\hat{J}_y\hat{p}e^{-iG(t)\hat{J}_y\hat{p}} \tag{146}$$

Where we used the commutation relation:

$$\left[\hat{J}_y\hat{p}, e^{-iF(t)\hat{J}_y\hat{x}}\right] = \sum_{n=1}^{\infty}\frac{(-iF(t))^n}{n!}\left[\hat{J}_y\hat{p}, \left(\hat{J}_y\hat{x}\right)^n\right] \tag{147}$$

$$\left[\hat{J}_y\hat{p}, \left(\hat{J}_y\hat{x}\right)^n\right] = \hat{J}_y\hat{p}\hat{J}_y^n\hat{x}^n - \hat{J}_y^n\hat{x}^n\hat{J}_y\hat{p} = \hat{J}_y^{n+1}[\hat{p}, \hat{x}^n] = \hat{J}_y^{n+1}(-i)n\hat{x}^{n-1} \tag{148}$$

$$\Rightarrow \left[\hat{J}_y\hat{p}, e^{-iF(t)\hat{J}_y\hat{x}}\right] = \sum_{n=1}^{\infty}\frac{(-iF(t))^n}{n!}\hat{J}_y^{n+1}(-i)n\hat{x}^{n-1} \tag{149}$$

$$= -\hat{J}_y^2F(t)\sum_{n=1}^{\infty}\frac{(-iF(t))^{n-1}}{(n-1)!}\hat{J}_y^{n-1}\hat{x}^{n-1} = -\hat{J}_y^2F(t)e^{-iF(t)\hat{J}_y\hat{x}} \tag{150}$$

Comparing the two results we conclude that:

$$\begin{cases} A'(t) = -F(t)g(t) \\ F'(t) = f(t) \\ G'(t) = g(t) \end{cases} \Rightarrow \begin{cases} A(t) = -\int_0^t d\tau F(\tau)g(\tau) \\ F(t) = \int_0^t d\tau f(\tau) \\ G(t) = \int_0^t d\tau g(\tau) \end{cases} \tag{151}$$

We note that this proof does not assume anything on $f(t), g(t)$ (besides integrability).

6.2 Evolution in the qubit subspace (tracing out the trap)

6.2.1 Deriving Kraus decomposition

Following For the special case of unentangled initial conditions $\hat{\rho}(0) = \hat{\rho}_q(0) \otimes \hat{\rho}_h(0)$ then the dynamics is:

$$\hat{\rho}_q(t) = \mathrm{Tr}_h\left[\hat{U}(t)\,\hat{\rho}(t)\,\hat{U}^\dagger(t)\right] \tag{152}$$

$$= \sum_{i,j} \lambda_j \left\langle \psi_j^h \middle| \hat{U}(t)\,\hat{\rho}_q(0) \otimes \left(\left|\psi_i^h\right\rangle\left\langle\psi_i^h\right|\right)\hat{U}^\dagger(t) \middle| \psi_j^h \right\rangle \tag{153}$$

$$= \sum_{i,j} \lambda_j \left\langle \psi_j^h \middle| \hat{U}(t) \middle| \psi_i^h \right\rangle \hat{\rho}_q(0) \left\langle \psi_i^h \middle| \hat{U}^\dagger(t) \middle| \psi_j^h \right\rangle \tag{154}$$

$$= \sum_{i,j} \hat{K}_{i,j}(t)\,\hat{\rho}_q(0)\,\hat{K}_{i,j}^\dagger(t) \tag{155}$$

Where we used $\hat{\rho}_h(0) = \sum_i \lambda_i \left|\psi_i^h\right\rangle\left\langle\psi_i^h\right|$ and defined the Kraus operators:

$$\hat{K}_{i,j}(t) = \sqrt{\lambda_j}\left\langle \psi_j^h \middle| \hat{U}(t) \middle| \psi_i^h \right\rangle \tag{156}$$

So the evolution depends on the total unitary evolution operator and on the trap initial state.

6.2.2 Direct calculation of Kraus operators

Rewriting in terms of ladder operator In terms of ladder operators the evolution operator reads:

$$\hat{U} = e^{-iA(t)\hat{J}_y^2} e^{-iF(t)\hat{J}_y\hat{x}} e^{-iG(t)\hat{J}_y\hat{p}} \tag{157}$$

$$= e^{-iA(t)\hat{J}_y^2} e^{-iF(t)\hat{J}_y\left(\frac{\hat{a}^\dagger+\hat{a}}{\sqrt{2}}\right)} e^{-iG(t)\hat{J}_y\left(i\frac{\hat{a}^\dagger-\hat{a}}{\sqrt{2}}\right)} \tag{158}$$

We note that:

$$\left[\hat{J}_y\hat{a}^\dagger, \hat{J}_y\hat{a}\right] = \hat{J}_y^2\left[\hat{a}^\dagger, \hat{a}\right] = -\hat{J}_y^2 \tag{159}$$

$$\Rightarrow \left[\hat{J}_y\hat{a}^\dagger, \left[\hat{J}_y\hat{a}^\dagger, \hat{J}_y\hat{a}\right]\right] = \left[\hat{J}_y\hat{a}, \left[\hat{J}_y\hat{a}^\dagger, \hat{J}_y\hat{a}\right]\right] = 0 \tag{160}$$

Therefore Baker-Campbell-Hausdorff (BCH) lemma reduces to:

$$\left[\hat{A}, \left[\hat{A}, \hat{B}\right]\right] = \left[\hat{B}, \left[\hat{A}, \hat{B}\right]\right] = 0 \Rightarrow e^{\hat{A}+\hat{B}} = e^{\hat{A}} e^{\hat{B}} e^{-\frac{1}{2}\left[\hat{A},\hat{B}\right]} \tag{161}$$

We obtain (dropping the t, ξ notation):

$$e^{-\frac{iF(t)\hat{J}_y}{\sqrt{2}}\left(\hat{a}^\dagger+\hat{a}\right)} = e^{-\frac{iF\hat{J}_y\hat{a}^\dagger}{\sqrt{2}}}e^{-\frac{iF\hat{J}_y\hat{a}}{\sqrt{2}}}e^{-\frac{F^2\hat{J}_y^2}{4}} \tag{162}$$

$$e^{\frac{G(t)\hat{J}_y}{\sqrt{2}}\left(\hat{a}^\dagger-\hat{a}\right)} = e^{\frac{G\hat{J}_y\hat{a}^\dagger}{\sqrt{2}}}e^{-\frac{G\hat{J}_y\hat{a}}{\sqrt{2}}}e^{-\frac{G^2\hat{J}_y^2}{4}} \tag{163}$$

Thus:

$$\hat{U} = e^{-iA\hat{J}_y^2}\left(e^{-\frac{iF}{\sqrt{2}}\hat{J}_y\hat{a}^\dagger}e^{-\frac{iF}{\sqrt{2}}\hat{J}_y\hat{a}}e^{-\frac{F^2\hat{J}_y^2}{4}}\right)\left(e^{\frac{G}{\sqrt{2}}\hat{J}_y\hat{a}^\dagger}e^{-\frac{G}{\sqrt{2}}\hat{J}_y\hat{a}}e^{-\frac{G^2\hat{J}_y^2}{4}}\right) \tag{164}$$

$$= \left(e^{-\left(iA+\frac{F^2+G^2}{4}\right)\hat{J}_y^2}\right)\left(e^{-\frac{iF}{\sqrt{2}}\hat{J}_y\hat{a}^\dagger}e^{-\frac{iF}{\sqrt{2}}\hat{J}_y\hat{a}}e^{\frac{G}{\sqrt{2}}\hat{J}_y\hat{a}^\dagger}e^{-\frac{G}{\sqrt{2}}\hat{J}_y\hat{a}}\right) \tag{165}$$

To commute we use:

$$\left[e^{f\hat{J}_y\hat{a}}, e^{g\hat{J}_y a^\dagger}\right] = e^{f\hat{J}_y\hat{a}}e^{g\hat{J}_y\hat{a}^\dagger} - e^{g\hat{J}_y\hat{a}^\dagger}e^{f\hat{J}_y\hat{a}} \tag{166}$$

$$\underbrace{=}_{BCH} e^{f\hat{J}_y\hat{a}+g\hat{J}_y\hat{a}^\dagger}e^{\frac{fg}{2}\hat{J}_y^2} - e^{g\hat{J}_y\hat{a}^\dagger+f\hat{J}_y\hat{a}}e^{-\frac{fg}{2}\hat{J}_y^2} \tag{167}$$

$$= e^{g\hat{J}_y\hat{a}^\dagger+f\hat{J}_y\hat{a}}\left(e^{\frac{fg}{2}\hat{J}_y^2} - e^{-\frac{fg}{2}\hat{J}_y^2}\right) \tag{168}$$

$$\underbrace{=}_{BCH} e^{g\hat{J}_y\hat{a}^\dagger}e^{f\hat{J}_y\hat{a}}e^{\frac{fg}{2}\hat{J}_y^2}\left(e^{\frac{fg}{2}\hat{J}_y^2} - e^{-\frac{fg}{2}\hat{J}_y^2}\right) = e^{g\hat{J}_y\hat{a}^\dagger}e^{f\hat{J}_y\hat{a}}\left(e^{fg\hat{J}_y^2} - \mathbb{1}\right) \tag{169}$$

In our case:

$$\left[e^{-\frac{iF}{\sqrt{2}}\hat{J}_y\hat{a}}, e^{\frac{G}{\sqrt{2}}\hat{J}_y\hat{a}^\dagger}\right] = e^{\frac{G}{\sqrt{2}}\hat{J}_y\hat{a}^\dagger}e^{-\frac{iF}{\sqrt{2}}\hat{J}_y\hat{a}}\left(e^{\frac{-iFG}{2}\hat{J}_y^2} - \mathbb{1}\right) \tag{170}$$

Therefore:

$$\hat{U} = e^{-\left(iA+\frac{F^2+G^2}{4}\right)\hat{J}_y^2}\left(e^{-\frac{iF}{\sqrt{2}}\hat{J}_y\hat{a}^\dagger}e^{-\frac{iF}{\sqrt{2}}\hat{J}_y\hat{a}}e^{\frac{G}{\sqrt{2}}\hat{J}_y\hat{a}^\dagger}e^{-\frac{G}{\sqrt{2}}\hat{J}_y\hat{a}}\right) \tag{171}$$

$$= e^{-\left(iA+\frac{F^2+G^2}{4}\right)\hat{J}_y^2}\left(e^{-\frac{iF}{\sqrt{2}}\hat{J}_y\hat{a}^\dagger}\left(\left[e^{-\frac{iF}{\sqrt{2}}\hat{J}_y\hat{a}}, e^{\frac{G}{\sqrt{2}}\hat{J}_y\hat{a}^\dagger}\right] + e^{\frac{G}{\sqrt{2}}\hat{J}_y a^\dagger}e^{-\frac{iF}{\sqrt{2}}\hat{J}_y\hat{a}}\right)e^{-\frac{G}{\sqrt{2}}\hat{J}_y\hat{a}}\right) \tag{172}$$

$$= e^{-\left(iA+\frac{F^2+G^2}{4}+\frac{iFG}{2}\right)\hat{J}_y^2}\left(e^{-\frac{iF}{\sqrt{2}}\hat{J}_y\hat{a}^\dagger}e^{\frac{G}{\sqrt{2}}\hat{J}_y\hat{a}^\dagger}e^{-\frac{iF}{\sqrt{2}}\hat{J}_y\hat{a}}e^{-\frac{G}{\sqrt{2}}\hat{J}_y\hat{a}}\right) \tag{173}$$

$$= e^{-\left(iA+\frac{(F+iG)(F-iG)}{4}\right)\hat{J}_y^2}\left(e^{-\frac{iF-G}{\sqrt{2}}\hat{J}_y\hat{a}^\dagger}e^{-\frac{iF+G}{\sqrt{2}}\hat{J}_y\hat{a}}\right) \tag{174}$$

This final equation is a good starting point for tracing out the trap degrees of freedom.

Partial tracing To proceed we need to eliminate the trap degrees of freedom. We note that:

$$\left\langle n\left|e^{T\hat{a}^{\dagger}}\right|k\right\rangle \underbrace{=}_{n\geq k}\left\langle n\left|\sum_{j=0}^{\infty}\frac{\left(T\hat{a}^{\dagger}\right)^{j}}{j!}\right|k\right\rangle =\frac{T^{n-k}}{(n-k)!}\sqrt{k+1}\sqrt{k+2}\cdots\sqrt{n}=\frac{T^{n-k}}{(n-k)!}\sqrt{\frac{n!}{k!}} \tag{175}$$

Similarly:

$$\left\langle k\left|e^{T\hat{a}}\right|m\right\rangle \underbrace{=}_{m\geq k}\left\langle k\left|\sum_{j=0}^{\infty}\frac{\left(e^{T\hat{a}}\right)^{j}}{j!}\right|m\right\rangle =\frac{T^{m-k}}{(m-k)!}\sqrt{m}\sqrt{m-1}\cdots\sqrt{k+1}=\frac{T^{m-k}}{(m-k)!}\sqrt{\frac{m!}{k!}} \tag{176}$$

Also, for two qubits we have: $\hat{J}_y^1=\hat{J}_y^3=\hat{J}_y^5=...$ and $\hat{J}_y^2=\hat{J}_y^4=\hat{J}_y^6=....$. Therefore, by assuming $n+m\neq 0$ and $n\neq m$ we have:

$$H_{nm} \equiv \left\langle n \left| e^{-\frac{iF-G}{\sqrt{2}}\hat{J}_y\hat{a}^\dagger} e^{-\frac{iF+G}{\sqrt{2}}\hat{J}_y\hat{a}} \right| m \right\rangle \tag{177}$$

$$= \sum_k \left\langle n \left| e^{-\frac{iF-G}{\sqrt{2}}\hat{J}_y\hat{a}^\dagger} \right| k \right\rangle \left\langle k \left| e^{-\frac{iF+G}{\sqrt{2}}\hat{J}_y\hat{a}} \right| m \right\rangle \tag{178}$$

$$\sum_{k\leq\min\{n,m\}} \frac{\left(-\frac{iF-G}{\sqrt{2}}\hat{J}_y\right)^{n-k}}{(n-k)!}\sqrt{\frac{n!}{k!}}\frac{\left(-\frac{iF+G}{\sqrt{2}}\hat{J}_y\right)^{m-k}}{(m-k)!}\sqrt{\frac{m!}{k!}} \tag{179}$$

$$= \sqrt{n!m!}\sum_{k\leq\min\{n,m\}} \frac{\left(-\frac{iF-G}{\sqrt{2}}\right)^{n-k}\left(-\frac{iF+G}{\sqrt{2}}\right)^{m-k}\hat{J}_y^{n+m-2k}}{(n-k)!\,(m-k)!k!} \tag{180}$$

$$= \hat{J}_y^{n+m}\sqrt{n!m!}\left(-\frac{iF-G}{\sqrt{2}}\right)^n\left(-\frac{iF+G}{\sqrt{2}}\right)^m \sum_{k\leq\min\{n,m\}} \frac{\left(\frac{iF-G}{\sqrt{2}}\cdot\frac{iF+G}{\sqrt{2}}\right)^{-k}}{(n-k)!\,(m-k)!k!} \tag{181}$$

$$= \hat{J}_y^{n+m}\sqrt{n!m!}\left(-\frac{iF-G}{\sqrt{2}}\right)^n\left(-\frac{iF+G}{\sqrt{2}}\right)^m \begin{cases} \sum_{k=0}^n \frac{1}{(n-k)!(m-k)!k!}\left(-\frac{F^2+G^2}{2}\right)^{-k} & n\leq m \\ \sum_{k=0}^m \frac{1}{(n-k)!(m-k)!k!}\left(-\frac{F^2+G^2}{2}\right)^{-k} & m\leq n \end{cases} \tag{182}$$

$$\underbrace{=}_{\substack{k\to n-k \\ k\to m-k}} \frac{\hat{J}_y^{n+m}}{\sqrt{n!m!}}\left(-\frac{iF-G}{\sqrt{2}}\right)^n\left(-\frac{iF+G}{\sqrt{2}}\right)^m \begin{cases} \left(-\frac{F^2+G^2}{2}\right)^{-n}\sum_{k=0}^n \frac{n!m!\left(-\frac{F^2+G^2}{2}\right)^k}{(m-n+k)!(n-k)!k!} & n\leq m \\ \left(-\frac{F^2+G^2}{2}\right)^{-m}\sum_{k=0}^m \frac{n!m!\left(-\frac{F^2+G^2}{2}\right)^k}{(n-m+k)!(m-k)!k!} & m\leq n \end{cases} \tag{183}$$

$$= \frac{\hat{J}_y^{n+m}}{\sqrt{n!m!}}\left(-\frac{iF-G}{\sqrt{2}}\right)^n\left(-\frac{iF+G}{\sqrt{2}}\right)^m \begin{cases} \left(-\frac{F^2(t)+G^2}{2}\right)^{-n} n!\sum_{k=0}^n \binom{n+(m-n)}{n-k}\frac{(-1)^k}{k!}\left(\frac{F^2+G^2}{2}\right)^k & n\leq m \\ \left(-\frac{F^2+G^2}{2}\right)^{-m} m!\sum_{k=0}^m \binom{m+(n-m)}{m-k}\frac{(-1)^k}{k!}\left(\frac{F^2+G^2}{2}\right)^k & m\leq n \end{cases} \tag{184}$$

$$= \frac{\hat{J}_y^{n+m}}{\sqrt{n!m!}}\left(-\frac{iF-G}{\sqrt{2}}\right)^n\left(-\frac{iF+G}{\sqrt{2}}\right)^m \begin{cases} \left(-\frac{F^2+G^2}{2}\right)^{-n} n!L_n^{(m-n)}\left(\frac{F^2+G^2}{2}\right) & n\leq m \\ \left(-\frac{F^2+G^2}{2}\right)^{-m} m!L_m^{(n-m)}\left(\frac{F^2+G^2}{2}\right) & m\leq n \end{cases} \tag{185}$$

$$= \frac{\hat{J}_y^{n+m}}{\sqrt{n!m!}} \begin{cases} (-1)^m\left(\frac{iF+G}{\sqrt{2}}\right)^{m-n} n!L_n^{(m-n)}\left(\frac{F^2+G^2}{2}\right) & n\leq m \\ (-1)^n\left(\frac{iF-G}{\sqrt{2}}\right)^{n-m} m!L_m^{(n-m)}\left(\frac{F^2+G^2}{2}\right) & m\leq n \end{cases} \tag{186}$$

Where $L_n^{(\alpha)}$ is the generalized n'th order Laguerre polynomial defined by:

$$L_n^{(\alpha)}(x) = \sum_{k=0}^{\infty}(-1)^k\binom{n+\alpha}{n-k}\frac{x^k}{k!} \tag{187}$$

We note that for $n=m=0$ then we just get:

$$\left\langle 0\left|e^{-\frac{iF-G}{\sqrt{2}}\hat{J}_y\hat{a}^\dagger}e^{-\frac{iF+G}{\sqrt{2}}\hat{J}_y\hat{a}}\right|0\right\rangle=\sum_k\left\langle 0\left|e^{-\frac{iF-G}{\sqrt{2}}\hat{J}_y\hat{a}^\dagger}\right|k\right\rangle\left\langle k\left|e^{-\frac{iF+G}{\sqrt{2}}\hat{J}_y\hat{a}}\right|0\right\rangle \tag{188}$$

$$=\sum_k\langle 0\left|\mathbb{1}\right|k\rangle\langle k\left|\mathbb{1}\right|0\rangle=\mathbb{1} \tag{189}$$

Which also fits the previous derivation since:

$$\frac{\hat{J}_y^0}{\sqrt{0!0!}}(-1)^0\left(\frac{iF(t)\pm G}{\sqrt{2}}\right)^0 0!L_0^{(0)}(0)=\mathbb{1} \tag{190}$$

For $n=m$ we get:

$$H_{nn}\equiv\left\langle n\left|e^{-\frac{iF-G}{\sqrt{2}}\hat{J}_y\hat{a}^\dagger}e^{-\frac{iF+G}{\sqrt{2}}\hat{J}_y\hat{a}}\right|n\right\rangle=\sum_k\left\langle n\left|e^{-\frac{iF-G}{\sqrt{2}}\hat{J}_y\hat{a}^\dagger}\right|k\right\rangle\left\langle k\left|e^{-\frac{iF+G}{\sqrt{2}}\hat{J}_y\hat{a}}\right|n\right\rangle \tag{191}$$

$$\sum_{k=0}^n\frac{\left(-\frac{iF-G}{\sqrt{2}}\hat{J}_y\right)^{n-k}}{(n-k)!}\sqrt{\frac{n!}{k!}}\frac{\left(-\frac{iF+G}{\sqrt{2}}\hat{J}_y\right)^{n-k}}{(m-k)!}\sqrt{\frac{n!}{k!}} \tag{192}$$

$$=n!\sum_{k=0}^n\frac{\left(-\frac{F^2+G^2}{2}\right)^{n-k}\hat{J}_y^{2(n-k)}}{(n-k)!\,(n-k)!k!}\underbrace{=}_{k\to n-k}n!\sum_{k=0}^n\frac{\left(-\frac{F^2+G^2}{2}\right)^k\hat{J}_y^{2k}}{k!k!\,(n-k)!} \tag{193}$$

$$=\mathbb{1}+\hat{J}_y^2\left(L_n\left(\frac{F^2+G^2}{2}\right)-1\right) \tag{194}$$

Where $L_n(x)\equiv L_n^{(0)}(x)$. Therefore:

$$\left\langle n\left|\hat{U}\right|m\right\rangle=e^{-\left(iA(t)+\frac{F^2+G^2}{4}+\frac{iFG}{2}\right)\hat{J}_y^2}\left\langle n\left|e^{-\frac{iF-G}{\sqrt{2}}\hat{J}_y\hat{a}^\dagger}e^{-\frac{iF+G}{\sqrt{2}}\hat{J}_y\hat{a}}\right|m\right\rangle \tag{195}$$

$$=e^{-\left(iA+\frac{F^2+G^2}{4}+\frac{iFG}{2}\right)\hat{J}_y^2}\begin{cases}\frac{\hat{J}_y^{n+m}}{\sqrt{n!m!}}(-1)^m\left(\frac{iF+G}{\sqrt{2}}\right)^{m-n}n!L_n^{(m-n)}\left(\frac{F^2+G^2}{2}\right) & n<m\\ \frac{\hat{J}_y^{n+m}}{\sqrt{n!m!}}(-1)^n\left(\frac{iF-G}{\sqrt{2}}\right)^{n-m}m!L_m^{(n-m)}\left(\frac{F^2+G^2}{2}\right) & n>m\\ \mathbb{1}+\hat{J}_y^2\left(L_n\left(\frac{F^2+G^2}{2}\right)-1\right) & n=m\end{cases} \tag{196}$$

We define:

$$\Phi\equiv\frac{F^2+G^2}{2},\qquad z\equiv iA+\frac{F^2+G^2}{4}+\frac{iFG}{2} \tag{197}$$

We note that assuming $F,G\in\mathbb{R}$ then $2\Re[z]=\Phi$. Using:

$$e^{z\hat{J}_y^2}=\frac{\mathbb{1}\otimes\mathbb{1}(e^z+1)+\sigma_y\otimes\sigma_y(e^z-1)}{2}\Rightarrow e^{z\hat{J}_y^2}\hat{J}_y^n=e^z\hat{J}_y^n \tag{198}$$

We simplify our result:

$$\left\langle n\left|\hat{U}\right|m\right\rangle = \begin{cases} e^{-z}\frac{\hat{J}_y^{n+m}}{\sqrt{n!m!}}\left(-1\right)^m\left(\frac{iF+G}{\sqrt{2}}\right)^{m-n} n!L_n^{(m-n)}\left(\Phi\right) & n<m \\ e^{-z}\frac{\hat{J}_y^{n+m}}{\sqrt{n!m!}}\left(-1\right)^n\left(\frac{iF-G}{\sqrt{2}}\right)^{n-m} m!L_m^{(n-m)}\left(\Phi\right) & n>m \\ e^{-z}L_n\left(\Phi\right)\hat{J}_y^2+\frac{\mathbb{1}\otimes\mathbb{1}-\sigma_y\otimes\sigma_y}{2} & n=m \end{cases} \tag{199}$$

$$= \begin{cases} e^{-\left(iA(t)+\frac{F^2(t)+G^2(t)}{4}+\frac{iF(t)G(t)}{2}\right)}\frac{\hat{J}_y^{n+m}}{\sqrt{n!m!}}\left(-1\right)^m\left(\frac{iF(t)+G(t)}{\sqrt{2}}\right)^{m-n} n!L_n^{(m-n)}\left(\frac{F^2(t)+G^2(t)}{2}\right) & n<m \\ e^{-\left(iA(t)+\frac{F^2(t)+G^2(t)}{4}+\frac{iF(t)G(t)}{2}\right)}\frac{\hat{J}_y^{n+m}}{\sqrt{n!m!}}\left(-1\right)^n\left(\frac{iF(t)-G(t)}{\sqrt{2}}\right)^{n-m} m!L_m^{(n-m)}\left(\frac{F^2(t)+G^2(t)}{2}\right) & n>m \\ e^{-\left(iA(t)+\frac{F^2(t)+G^2(t)}{4}+\frac{iF(t)G(t)}{2}\right)}L_n\left(\frac{F^2(t)+G^2(t)}{2}\right)\hat{J}_y^2+\frac{\mathbb{1}\otimes\mathbb{1}-\sigma_y\otimes\sigma_y}{2} & n=m \end{cases} \tag{200}$$

$$= \left(-1\right)^{n_>}\sqrt{\frac{n_<!}{n_>!}}e^{-\left(iA(t)+\frac{F^2(t)+G^2(t)}{4}+\frac{iF(t)G(t)}{2}\right)}\hat{J}_y^{n+n'}\left(\frac{G\left(t\right)+iF\left(t\right)}{\sqrt{2}}\right)^{n_>-n_<}L_{n_<}^{n_>-n_<}\left(\frac{F^2\left(t\right)+G^2\left(t\right)}{2}\right) \tag{201}$$

$$+\delta_{n,n'}\frac{\mathbb{1}\otimes\mathbb{1}-\sigma_y\otimes\sigma_y}{2} \tag{202}$$

6.2.3 Summation for thermal state

Starting with:

$$\left\langle n\left|\hat{U}\right|m\right\rangle = \begin{cases} e^{-z}\frac{\hat{J}_y^{n+m}}{\sqrt{n!m!}}\left(-1\right)^m\left(\frac{iF+G}{\sqrt{2}}\right)^{m-n} n!L_n^{(m-n)}\left(\Phi\right) & n<m \\ e^{-z}\frac{\hat{J}_y^{n+m}}{\sqrt{n!m!}}\left(-1\right)^n\left(\frac{iF-G}{\sqrt{2}}\right)^{n-m} m!L_m^{(n-m)}\left(\Phi\right) & n>m \\ e^{-z}L_n\left(\Phi\right)\hat{J}_y^2+\frac{\mathbb{1}\otimes\mathbb{1}-\sigma_y\otimes\sigma_y}{2} & n=m \end{cases} \tag{203}$$

We treat the three cases $m>n$, $m<n$ and $m=n$. Starting with $m>n$ we have:

$$\hat{K}_{m,n}\hat{\rho}_q\left(0\right)\hat{K}_{m,n}^\dagger = \lambda_n\left\langle n\left|\hat{U}\right|m\right\rangle\hat{\rho}_q\left(0\right)\left(\left\langle n\left|\hat{U}\right|m\right\rangle\right)^\dagger \tag{204}$$

$$= \frac{1}{\bar{n}+1}\left(\frac{\bar{n}}{\bar{n}+1}\right)^n e^{-z}\frac{\hat{J}_y^{n+m}}{\sqrt{n!m!}}\left(-1\right)^m\left(\frac{G+iF}{\sqrt{2}}\right)^{m-n} n!L_n^{(m-n)}\left(\Phi\right) \tag{205}$$

$$\cdot\,\hat{\rho}_q\left(0\right)e^{-z^*}\frac{\hat{J}_y^{n+m}}{\sqrt{n!m!}}\left(-1\right)^m\left(\frac{G-iF}{\sqrt{2}}\right)^{m-n} n!L_n^{(m-n)}\left(\Phi\right) \tag{206}$$

$$= \hat{J}_y^{n+m}\hat{\rho}_q\left(0\right)\hat{J}_y^{n+m}\frac{1}{\bar{n}+1}\left(\frac{\bar{n}}{\bar{n}+1}\right)^n\frac{e^{-\Phi}\Phi^{m-n}}{n!m!}\left(n!L_n^{(m-n)}\left(\Phi\right)\right)^2 \tag{207}$$

Similarly for $n > m$:

$$\hat{K}_{m,n}\hat{\rho}_q(0)\hat{K}_{m,n}^{\dagger} = \lambda_n \left\langle n\left|\hat{U}\right|m\right\rangle \hat{\rho}_q(0)\left(\left\langle n\left|\hat{U}\right|m\right\rangle\right)^{\dagger} \tag{208}$$

$$= \hat{J}_y^{n+m}\hat{\rho}_q(0)\hat{J}_y^{n+m}\frac{1}{\bar{n}+1}\left(\frac{\bar{n}}{\bar{n}+1}\right)^n \frac{e^{-\Phi}\Phi^{n-m}}{n!m!}\left(m!L_m^{(n-m)}(\Phi)\right)^2 \tag{209}$$

We can summarize these two options as follows - for $n \neq m$:

$$\begin{cases} \hat{K}_{m,n}\hat{\rho}_q(0)\hat{K}_{m,n}^{\dagger} \equiv \hat{J}_y^{n+m}\hat{\rho}_q(0)\hat{J}_y^{n+m}\frac{1}{\bar{n}+1}\left(\frac{\bar{n}}{\bar{n}+1}\right)^n h_{nm}^2 \\ h_{nm}^2 = \frac{e^{-\Phi}\Phi^{|n-m|}}{m!n!}\left(k!L_k^{(|n-m|)}(\Phi)\right)^2 \\ k = \min(n,m) \end{cases} \tag{210}$$

And for $n = m$:

$$\hat{K}_{n,n}\hat{\rho}_q(0)\hat{K}_{n,n}^{\dagger} = \lambda_n \left\langle n\left|\hat{U}\right|n\right\rangle \hat{\rho}_q(0)\left(\left\langle n\left|\hat{U}\right|n\right\rangle\right)^{\dagger} \tag{211}$$

$$= \frac{1}{\bar{n}+1}\left(\frac{\bar{n}}{\bar{n}+1}\right)^n \left[h_{nn}^2\hat{J}_y^2\hat{\rho}_q(0)\hat{J}_y^2 + \frac{\mathbb{1}\otimes\mathbb{1}-\sigma_y\otimes\sigma_y}{2}\hat{\rho}_q(0)\frac{\mathbb{1}\otimes\mathbb{1}-\sigma_y\otimes\sigma_y}{2}\right] \tag{212}$$

$$+ \frac{1}{\bar{n}+1}\left(\frac{\bar{n}}{\bar{n}+1}\right)^n L_n(\Phi)\left[\hat{J}_y^2\hat{\rho}_q(0)\frac{\mathbb{1}\otimes\mathbb{1}-\sigma_y\otimes\sigma_y}{2}e^{-z} + \frac{\mathbb{1}\otimes\mathbb{1}-\sigma_y\otimes\sigma_y}{2}\hat{\rho}_q(0)\hat{J}_y^2 e^{-z^*}\right] \tag{213}$$

To sum the second line on n we use the identity:

$$\sum_{n=0}^{\infty} x^n L_n(y) = \frac{e^{\frac{xy}{x-1}}}{1-x} \tag{214}$$

$$\Rightarrow \sum_{n=0}^{\infty}\left(\frac{\bar{n}}{\bar{n}+1}\right)^n L_n(\Phi) = (\bar{n}+1)e^{-\bar{n}\Phi} \tag{215}$$

Thus:

$$\sum_{n=0}^{\infty}\hat{K}_{n,n}\hat{\rho}_q(0)\hat{K}_{n,n}^{\dagger} = \frac{1}{\bar{n}+1}\sum_{n=0}^{\infty}\left(\frac{\bar{n}}{\bar{n}+1}\right)^n h_{nn}^2\hat{J}_y^2\hat{\rho}_q(0)\hat{J}_y^2 + \frac{\mathbb{1}\otimes\mathbb{1}-\sigma_y\otimes\sigma_y}{2}\hat{\rho}_q(0)\frac{\mathbb{1}\otimes\mathbb{1}-\sigma_y\otimes\sigma_y}{2} \tag{216}$$

$$+ e^{-\bar{n}\Phi}\left[\hat{J}_y^2\hat{\rho}_q(0)\frac{\mathbb{1}\otimes\mathbb{1}-\sigma_y\otimes\sigma_y}{2}e^{-z} + \frac{\mathbb{1}\otimes\mathbb{1}-\sigma_y\otimes\sigma_y}{2}\hat{\rho}_q(0)\hat{J}_y^2 e^{-z^*}\right] \tag{217}$$

Therefore the evolution is given by:

$$\hat{\rho}_q(t) = \sum_{n,m} \hat{K}_{m,n} \hat{\rho}_q(0) \hat{K}^\dagger_{m,n} \tag{218}$$

$$= \frac{\hat{J}_y^2 \hat{\rho}_q(0) \hat{J}_y^2}{\bar{n}+1} \sum_{n+m \text{ even}} \left(\frac{\bar{n}}{\bar{n}+1}\right)^n h_{nm}^2 + \frac{\hat{J}_y \hat{\rho}_q(0) \hat{J}_y}{\bar{n}+1} \sum_{n,m \text{ odd}} \left(\frac{\bar{n}}{\bar{n}+1}\right)^n h_{nm}^2 \tag{219}$$

$$+ \frac{\mathbb{1}\otimes\mathbb{1} - \sigma_y \otimes \sigma_y}{2} \hat{\rho}_q(0) \frac{\mathbb{1}\otimes\mathbb{1} - \sigma_y \otimes \sigma_y}{2} \tag{220}$$

$$+ e^{-\bar{n}\Phi} \left(\hat{J}_y^2 \hat{\rho}_q(0) \frac{\mathbb{1}\otimes\mathbb{1} - \sigma_y \otimes \sigma_y}{2} e^{-z} + \frac{\mathbb{1}\otimes\mathbb{1} - \sigma_y \otimes \sigma_y}{2} \hat{\rho}_q(0) \hat{J}_y^2 e^{-z^*} \right) \tag{221}$$

Solving the series To solve the even and odd sums we use the following identities:

$$\begin{cases} \sum_{n=0}^{\infty} n! \frac{L_n^{(\alpha)}(x) L_n^{(\alpha)}(y) z^n}{\Gamma(n+\alpha+1)} = \frac{(xyz)^{-\frac{1}{2}\alpha}}{1-z} e^{-z\frac{x+y}{1-z}} I_\alpha\left(2\frac{\sqrt{xyz}}{1-z}\right) & \text{Poisson kernel} \\ \cosh\left(\frac{\sqrt{z+2+\frac{1}{z}}}{2}x\right) = \sum_{l=-\infty}^{\infty} z^l I_{2l}(x) \\ \sinh\left(\frac{\sqrt{z+2+\frac{1}{z}}}{2}x\right) = \sum_{l=-\infty}^{\infty} z^l I_{2l+1}(x) \end{cases} \tag{222}$$

The first identity is known as Poisson kernel and may be found in [30] (p. 101), and the next two are a consequence of the generalization of the Jacobi identity. Where I_n is the n'th order modified Bessel function defined by:

$$I_n = \sum_{m=0}^{\infty} \frac{1}{m!\Gamma(m+\alpha+1)} \left(\frac{x}{2}\right)^{2m+n} \tag{223}$$

We start with computing the even sum, we change to even variables:

$$\begin{cases} n+m = 2k \\ n-m = 2l \end{cases} \tag{224}$$

Therefore:

$$\Sigma_e = \sum_{n+m \text{ even}} \left(\frac{\bar{n}}{\bar{n}+1}\right)^n h_{nm}^2 \tag{225}$$

$$= e^{-\Phi} \sum_{n+m \text{ even}} \left(\frac{\bar{n}}{\bar{n}+1}\right)^n \frac{\Phi^{|n-m|} \left(\min\left(n,m\right)!\right)^2}{n!m!} \left(L_{\min(n,m)}^{|n-m|}\left(\Phi\right)\right)^2 \tag{226}$$

$$= e^{-\Phi} \sum_{l=-\infty}^{\infty} \sum_{k=|l|}^{\infty} \left(\frac{\bar{n}}{\bar{n}+1}\right)^{k+l} \frac{\Phi^{2l} \left(\min\left(k-l,k+l\right)!\right)^2}{\left(k+l\right)!\left(k-l\right)!} \left(L_{\min(n,m)}^{|2l|}\left(\Phi\right)\right)^2 \tag{227}$$

$$= e^{-\Phi} \sum_{l=0}^{\infty} \sum_{k=l}^{\infty} \left(\frac{\bar{n}}{\bar{n}+1}\right)^{k+l} \Phi^{2l} \frac{\left(k-l\right)!}{\left(k+l\right)!} \left(L_{k-l}^{2l}\left(\Phi\right)\right)^2 \tag{228}$$

$$+ e^{-\Phi} \sum_{l=0}^{\infty} \sum_{k=l}^{\infty} \left(\frac{\bar{n}}{\bar{n}+1}\right)^{k-l} \Phi^{2l} \frac{\left(k-l\right)!}{\left(k+l\right)!} \left(L_{k-l}^{2l}\left(\Phi\right)\right)^2 - e^{-\Phi} \sum_{k=0}^{\infty} \left(\frac{\bar{n}}{\bar{n}+1}\right)^{k} \left(L_k\left(\Phi\right)\right)^2 \tag{229}$$

$$= e^{-\Phi} \sum_{l=0}^{\infty} \left[\left(\frac{\bar{n}}{\bar{n}+1}\right)^{l} + \left(\frac{\bar{n}}{\bar{n}+1}\right)^{-l}\right] \sum_{k=l}^{\infty} \left(\frac{\bar{n}}{\bar{n}+1}\right)^{k} \Phi^{2l} \frac{\left(k-l\right)!}{\left(k+l\right)!} \left(L_{k-l}^{2l}\left(\Phi\right)\right)^2 \tag{230}$$

$$- e^{-\Phi} \sum_{k=0}^{\infty} \left(\frac{\bar{n}}{\bar{n}+1}\right)^{k} \left(L_k\left(\Phi\right)\right)^2 \tag{231}$$

Where we split to to sums $l = 0, ..., \infty$ and $l = 0, ..., -\infty$ (and compensated for counting $l = 0$ twice). Next we shift $k \to k + l$ and get:

$$\Sigma_e = e^{-\Phi} \sum_{l=0}^{\infty} \left[\left(\frac{\bar{n}}{\bar{n}+1}\right)^{2l} + 1\right] \sum_{k=0}^{\infty} \left(\frac{\bar{n}}{\bar{n}+1}\right)^{k} \Phi^{2l} \frac{k!}{\left(k+2l\right)!} \left(L_l^{2l}\left(\Phi\right)\right)^2 \tag{232}$$

$$- e^{-\Phi} \sum_{k=0}^{\infty} \left(\frac{\bar{n}}{\bar{n}+1}\right)^{k} \left(L_k\left(\Phi\right)\right)^2 \tag{233}$$

This is exactly the Laguerre Poisson kernel identity (for both terms):

$$\Sigma_e = \left(\bar{n}+1\right) e^{-2\Phi\bar{n}} e^{-\Phi} \sum_{l=0}^{\infty} \left[\left(\frac{\bar{n}}{\bar{n}+1}\right)^{l} + \left(\frac{\bar{n}}{\bar{n}+1}\right)^{-l}\right] I_{2l}\left(2\Phi\sqrt{\bar{n}\left(\bar{n}+1\right)}\right) \tag{234}$$

$$- \left(\bar{n}+1\right) e^{-\Phi} e^{-2\Phi\bar{n}} I_0\left(2\Phi\sqrt{\bar{n}\left(\bar{n}+1\right)}\right) \tag{235}$$

$$= \left(\bar{n}+1\right) e^{-2\Phi\bar{n}} e^{-\Phi} \sum_{l=-\infty}^{\infty} \left(\frac{\bar{n}}{\bar{n}+1}\right)^{l} I_{2l}\left(2\Phi\sqrt{\bar{n}\left(\bar{n}+1\right)}\right) \tag{236}$$

And use the Bessel sum identity:

$$\Sigma_e = (\bar{n}+1)\, e^{-2\Phi\bar{n}} e^{-\Phi} \cosh\left(\frac{\sqrt{\frac{\bar{n}}{\bar{n}+1} + 2 + \frac{1}{\frac{\bar{n}}{\bar{n}+1}}}}{2} 2\Phi\sqrt{\bar{n}\,(\bar{n}+1)} \right) \tag{237}$$

$$= (\bar{n}+1)\, e^{-(2\bar{n}+1)\Phi} \cosh\left((2\bar{n}+1)\,\Phi\right) \tag{238}$$

$$= (\bar{n}+1)\, \frac{1 + e^{-2(2\bar{n}+1)\Phi}}{2} \tag{239}$$

We follow similar lines for the odd case by changing:

$$\begin{cases} n+m = 2k+1 \\ n-m = 2l+1 \end{cases} \tag{240}$$

And obtain

$$\Sigma_o = \sum_{n+m\,\text{odd}} \left(\frac{\bar{n}}{\bar{n}+1}\right)^n h_{nm}^2 \tag{241}$$

$$= e^{-\Phi} \sum_{n+m\,\text{odd}} \left(\frac{\bar{n}}{\bar{n}+1}\right)^n \frac{\Phi^{|n-m|}\left(\min(n,m)!\right)^2}{n!m!} \left(L^{(|n-m|)}_{\min(n,m)}(\Phi)\right)^2$$

$$= e^{-\Phi} \sum_{l=-\infty}^{\infty} \sum_{k} \left(\frac{\bar{n}}{\bar{n}+1}\right)^{l+k+1} \frac{\Phi^{|2l+1|}\left(\min(l+k+1, k-l)!\right)^2}{(l+k+1)!\,(k-l)!} \left(L^{(|2l+1|)}_{\min(l+k+1,k-l)}(\Phi)\right)^2 \tag{242}$$

$$= e^{-\Phi} \sum_{l=0}^{\infty} \sum_{k=l}^{\infty} \left(\frac{\bar{n}}{\bar{n}+1}\right)^{l+k+1} \frac{\Phi^{2l+1}\,(k-l)!}{(l+k+1)!} \left(L^{(2l+1)}_{k-l}(\Phi)\right)^2 \tag{243}$$

$$+ e^{-\Phi} \sum_{l=1}^{\infty} \sum_{k=l-1}^{\infty} \left(\frac{\bar{n}}{\bar{n}+1}\right)^{k-l+1} \frac{\Phi^{2l-1}\,(k-l+1)!}{(k+l)!} \left(L^{(|-2l+1|)}_{k-l+1}(\Phi)\right)^2 \tag{244}$$

$$= e^{-\Phi} \sum_{l=0}^{\infty} \sum_{k=0}^{\infty} \left(\frac{\bar{n}}{\bar{n}+1}\right)^{2l+k+1} \frac{\Phi^{2l+1} k!}{(2l+k+1)!} \left(L^{(2l+1)}_{k}(\Phi)\right)^2 \tag{245}$$

$$+ e^{-\Phi} \sum_{l=1}^{\infty} \sum_{k=0}^{\infty} \left(\frac{\bar{n}}{\bar{n}+1}\right)^{k} \frac{\Phi^{2l-1} k!}{(2l+k-1)!} \left(L^{(2l-1)}_{k}(\Phi)\right)^2 \tag{246}$$

Again by using the Laguerre Poisson kernel identity, and the Bessel sum identity:

$$\Sigma_o = (\bar{n}+1)\, e^{-(2\bar{n}+1)\Phi} \sum_{l=0}^{\infty} \left(\frac{\bar{n}}{\bar{n}+1}\right)^{\frac{2l+1}{2}} I_{2l+1}\left(2\Phi\sqrt{\bar{n}\,(\bar{n}+1)}\right) \tag{247}$$

$$+ (\bar{n}+1)\, e^{-(2\bar{n}+1)\Phi} \sum_{l=1}^{\infty} \left(\frac{\bar{n}}{\bar{n}+1}\right)^{-\frac{2l-1}{2}} e^{-2\Phi\bar{n}} I_{2l-1}\left(2\Phi\sqrt{\bar{n}\,(\bar{n}+1)}\right) \tag{248}$$

$$= (\bar{n}+1)\, e^{-(2\bar{n}+1)\Phi} \sum_{l=-\infty}^{\infty} \left(\frac{\bar{n}}{\bar{n}+1}\right)^{\frac{2l+1}{2}} I_{2l+1}\left(2\Phi\sqrt{\bar{n}\,(\bar{n}+1)}\right) \tag{249}$$

$$= (\bar{n}+1)\, e^{-(2\bar{n}+1)\Phi} \sinh\left(\frac{\sqrt{\frac{\bar{n}}{\bar{n}+1}+2+\frac{1}{\frac{\bar{n}}{\bar{n}+1}}}}{2} 2\Phi\sqrt{\bar{n}\,(\bar{n}+1)}\right) \tag{250}$$

$$= (\bar{n}+1)\, e^{-(2\bar{n}+1)\Phi} \sinh\left((2\bar{n}+1)\,\Phi\right) \tag{251}$$

$$= (\bar{n}+1)\, \frac{1-e^{-2(2\bar{n}+1)\Phi}}{2} \tag{252}$$

Back to evolution Setting the even and odd sums we obtain the total process:

$$\hat{\rho}_q(t) = \sum_{n,m} \hat{K}_{m,n} \hat{\rho}_q(0)\, \hat{K}_{m,n}^{\dagger} \tag{253}$$

$$= \frac{\hat{J}_y^2 \hat{\rho}_q(0)\, \hat{J}_y^2}{2} e^{-2(2\bar{n}+1)\Phi} - \frac{\hat{J}_y \hat{\rho}_q(0)\, \hat{J}_y}{2} e^{-2(2\bar{n}+1)\Phi} \tag{254}$$

$$+ \frac{\mathbb{1}\otimes\mathbb{1} - \sigma_y\otimes\sigma_y}{2} \hat{\rho}_q(0) \frac{\mathbb{1}\otimes\mathbb{1} - \sigma_y\otimes\sigma_y}{2} + \frac{\hat{J}_y^2 \hat{\rho}_q(0)\, \hat{J}_y^2}{2} + \frac{\hat{J}_y \hat{\rho}_q(0)\, \hat{J}_y}{2} \tag{255}$$

$$+ e^{-\bar{n}\Phi} \left(\hat{J}_y^2 \hat{\rho}_q(0) \frac{\mathbb{1}\otimes\mathbb{1} - \sigma_y\otimes\sigma_y}{2} e^{-z} + \frac{\mathbb{1}\otimes\mathbb{1} - \sigma_y\otimes\sigma_y}{2} \hat{\rho}_q(0)\, \hat{J}_y^2 e^{-z^*} \right) \tag{256}$$

Since $F(0) = G(0) = A(0) = 0$ then $\Phi(0) = z(0) = 0$ then we can use a sanity check:

$$\hat{\rho}_q(0) = \hat{J}_y^2 \hat{\rho}_q(0)\, \hat{J}_y^2 + \frac{\mathbb{1}\otimes\mathbb{1} - \sigma_y\otimes\sigma_y}{2} \hat{\rho}_q(0) \frac{\mathbb{1}\otimes\mathbb{1} - \sigma_y\otimes\sigma_y}{2} \tag{257}$$

$$+ \hat{J}_y^2 \hat{\rho}_q(0) \frac{\mathbb{1}\otimes\mathbb{1} - \sigma_y\otimes\sigma_y}{2} + \frac{\mathbb{1}\otimes\mathbb{1} - \sigma_y\otimes\sigma_y}{2} \hat{\rho}_q(0)\, \hat{J}_y^2 \tag{258}$$

$$= \left(\frac{\mathbb{1}\otimes\mathbb{1} + \sigma_y\otimes\sigma_y}{2} + \frac{\mathbb{1}\otimes\mathbb{1} - \sigma_y\otimes\sigma_y}{2}\right) \hat{\rho}_q(0) \left(\frac{\mathbb{1}\otimes\mathbb{1} + \sigma_y\otimes\sigma_y}{2} + \frac{\mathbb{1}\otimes\mathbb{1} - \sigma_y\otimes\sigma_y}{2}\right) \tag{259}$$

With some more manipulation we note that:

$$\frac{\hat{J}_y^2 \hat{\rho}_q(0)\, \hat{J}_y^2}{2} + \frac{\hat{J}_y \hat{\rho}_q(0)\, \hat{J}_y}{2} + \frac{\mathbb{1}\otimes\mathbb{1} - \sigma_y\otimes\sigma_y}{2} \hat{\rho}_q(0) \frac{\mathbb{1}\otimes\mathbb{1} - \sigma_y\otimes\sigma_y}{2} \tag{260}$$

Is equal to:

$$\hat{\rho}_q(0) - \frac{\hat{J}_y^2\hat{\rho}_q(0)\hat{J}_y^2}{2} + \frac{\hat{J}_y\hat{\rho}_q(0)\hat{J}_y}{2} - \hat{J}_y^2\hat{\rho}_q(0)\frac{\mathbb{1}\otimes\mathbb{1}-\sigma_y\otimes\sigma_y}{2} - \frac{\mathbb{1}\otimes\mathbb{1}-\sigma_y\otimes\sigma_y}{2}\hat{\rho}_q(0)\hat{J}_y^2 \tag{261}$$

Therefore:

$$\hat{\rho}_q(t) = \hat{\rho}_q(0) + \frac{\hat{J}_y^2\hat{\rho}_q(0)\hat{J}_y^2}{2}\left(e^{-2(2\bar{n}+1)\Phi}-1\right) - \frac{\hat{J}_y\hat{\rho}_q(0)\hat{J}_y}{2}\left(e^{-2(2\bar{n}+1)\Phi}-1\right) \tag{262}$$

$$+ \hat{J}_y^2\hat{\rho}_q(0)\frac{\mathbb{1}\otimes\mathbb{1}-\sigma_y\otimes\sigma_y}{2}\left(e^{-z-\bar{n}\Phi}-1\right) + \frac{\mathbb{1}\otimes\mathbb{1}-\sigma_y\otimes\sigma_y}{2}\hat{\rho}_q(0)\hat{J}_y^2\left(e^{-z^*-\bar{n}\Phi}-1\right) \tag{263}$$

$$= \hat{\rho}_q(0) + \frac{\hat{J}_y^2\hat{\rho}_q(0)\hat{J}_y^2}{2}\left(e^{-2(2\bar{n}+1)\frac{F^2(t)+G^2(t)}{2}}-1\right) \tag{264}$$

$$- \frac{\hat{J}_y\hat{\rho}_q(0)\hat{J}_y}{2}\left(e^{-2(2\bar{n}+1)\frac{F^2(t)+G^2(t)}{2}}-1\right) \tag{265}$$

$$+ \hat{J}_y^2\hat{\rho}_q(0)\frac{\mathbb{1}\otimes\mathbb{1}-\sigma_y\otimes\sigma_y}{2}\left(e^{-\left(\bar{n}+\frac{1}{2}\right)\frac{F^2(t)+G^2(t)}{2}-i\left(A(t)+\frac{F(t)G(t)}{2}\right)}-1\right) \tag{266}$$

$$+ \frac{\mathbb{1}\otimes\mathbb{1}-\sigma_y\otimes\sigma_y}{2}\hat{\rho}_q(0)\hat{J}_y^2\left(e^{-\left(\bar{n}+\frac{1}{2}\right)\frac{F^2(t)+G^2(t)}{2}+i\left(A(t)+\frac{F(t)G(t)}{2}\right)}-1\right) \tag{267}$$

6.3 Optimizing robustness to gate timing-errors

6.3.1 Ladder Cardioid drive - phase space trajectory

We derive F, G for an ladder Cardioid drive. Setting the amplitudes:

$$r_j = (-1)^{N-j}\frac{N!}{2^N}\sqrt{\frac{2\sqrt{\pi}}{(N-1)!\Gamma\left(N+\frac{1}{2}\right)}}\binom{N-1}{j-1} \tag{268}$$

We obtain:

$$F(t) = -\frac{1}{\sqrt{2}}\sum_{j=1}^{N}\frac{r_j}{j}\left(\sin\left(j\xi_0 t\right)\right) \tag{269}$$

$$= -\frac{N!}{2^N}\sqrt{\frac{\sqrt{\pi}}{(N-1)!\Gamma\left(N+\frac{1}{2}\right)}}\sum_{j=1}^{N}(-1)^{N-j}\binom{N-1}{j-1}\frac{1}{j}\sin\left(j\xi_0 t\right) \tag{270}$$

$$= -\frac{(-1)^N}{2^N}\sqrt{\frac{\sqrt{\pi}\,(N-1)!}{4\Gamma\left(N+\frac{1}{2}\right)}}i\left(e^{-i\frac{N\xi_0 t}{2}}\left(e^{i\frac{\xi_0 t}{2}}-e^{-i\frac{\xi_0 t}{2}}\right)^N - e^{i\frac{N\xi_0 t}{2}}(-1)^N\left(e^{i\frac{\xi_0 t}{2}}-e^{-i\frac{\xi_0 t}{2}}\right)^N\right) \tag{271}$$

$$= \begin{cases} -\sqrt{\frac{\sqrt{\pi}(N-1)!}{\Gamma\left(N+\frac{1}{2}\right)}}\sin\left(\frac{N\xi_0 t}{2}\right)(-1)^{\frac{N}{2}}\sin^N\left(\frac{\xi_0 t}{2}\right) & N=2K \\ \sqrt{\frac{\sqrt{\pi}(N-1)!}{\Gamma\left(N+\frac{1}{2}\right)}}\cos\left(\frac{N\xi_0 t}{2}\right)(-1)^{\frac{N+1}{2}}\sin^N\left(\frac{\xi_0 t}{2}\right) & N=2K-1 \end{cases} \tag{272}$$

$$= \sqrt{\frac{\sqrt{\pi}\,(N-1)!}{\Gamma\left(N+\frac{1}{2}\right)}}\sin^N\left(\frac{\xi_0 t}{2}\right)\left(\left(\frac{1-(-1)^N}{2}\right)(-1)^{\frac{N+1}{2}}\cos\left(\frac{N\xi_0 t}{2}\right) - \left(\frac{1+(-1)^N}{2}\right)(-1)^{\frac{N}{2}}\sin\left(\frac{N\xi_0 t}{2}\right)\right) \tag{273}$$

Similarly, one can show that:

$$G(t)=\sqrt{\frac{\sqrt{\pi}\,(N-1)!}{\Gamma\left(N+\frac{1}{2}\right)}}\sin^{N}\left(\frac{\xi_0 t}{2}\right)\left(\left(\frac{1-(-1)^{N}}{2}\right)(-1)^{\frac{N+1}{2}}\sin\left(\frac{N\xi_0 t}{2}\right)+\left(\frac{1+(-1)^{N}}{2}\right)(-1)^{\frac{N}{2}}\cos\left(\frac{N\xi_0 t}{2}\right)\right) \tag{274}$$

6.3.2 Accumulated phase

We derive $A(t)$ for the ladder Cardioid drive. By setting:

$$\begin{cases} R(t)=\sqrt{G^2(t)+F^2(t)}=\sqrt{\frac{\sqrt{\pi}(N-1)!}{\Gamma\left(N+\frac{1}{2}\right)}}\left|\sin^{N}\left(\frac{\xi_0 t}{2}\right)\right| \\ \phi(t)=\arctan\left(\frac{F(t)}{G(t)}\right)=(-1)^{N}\,\frac{N\xi_0 t}{2} \end{cases} \tag{275}$$

We compute directly:

$$A(t)=-\int_0^t d\tau F(\tau)\,g(\tau)=-\int_0^t d\tau R(\tau)\sin(\phi(\tau))\,\frac{\partial}{\partial\tau}\left(R(\tau)\cos(\phi(\tau))\right) \tag{276}$$

$$=-\int_0^t d\tau\frac{\partial R(\tau)}{\partial\tau}R(\tau)\sin(\phi(\tau))\cos(\phi(\tau))+\int_0^t d\tau R^2(\tau)\sin^2(\phi(\tau))\,\frac{\partial\phi(\tau)}{\partial\tau} \tag{277}$$

$$=-\frac{1}{2}\int_0^t d\tau\frac{\partial R^2(\tau)}{\partial\tau}\sin(\phi(\tau))\cos(\phi(\tau))+\int_0^{\phi_f} R^2(\phi)\sin^2(\phi)\,d\phi \tag{278}$$

$$=-\frac{1}{4}R^2(t)\sin(2\phi(t))+\frac{1}{2}\int_0^t d\tau R^2(\tau)\,\frac{\partial}{\partial\tau}\left(\frac{1}{2}\sin(2\phi(\tau))\right)+\int_0^{\phi_f} R^2(\phi)\sin^2(\phi)\,d\phi \tag{279}$$

$$=\frac{1}{2}\int_0^t d\tau R^2(\tau)\cos(2\phi(\tau))\,\frac{\partial\phi(\tau)}{\partial\tau}+\int_0^{\phi_f} R^2(\phi)\sin^2(\phi)\,d\phi-\frac{1}{4}R^2(t)\sin(2\phi(t)) \tag{280}$$

$$=\int_0^{\phi_f} R^2(\phi)\left(\sin^2(\phi)+\frac{1}{2}\cos(2\phi)\right)d\phi-\frac{1}{4}R^2(t)\sin(2\phi(t)) \tag{281}$$

$$=\frac{1}{2}\int_0^{\phi_f} R^2(\phi)\,d\phi-\frac{1}{4}R^2(t)\sin(2\phi(t)) \tag{282}$$

$$=(-1)^{N}\int_0^{\phi_f}\frac{\sqrt{\pi}\,(N-1)!}{2\Gamma\left(N+\frac{1}{2}\right)}\sin^{2N}\left(\frac{\phi}{N}\right)d\phi-\frac{1}{4}R^2(t)\sin(2\phi(t)) \tag{283}$$

$$=\frac{\sqrt{\pi}N!}{\Gamma\left(N+\frac{1}{2}\right)}\frac{\xi_0}{4}\int_0^t\sin^{2N}\left(\frac{\xi_0\tau}{2}\right)d\tau-\frac{1}{4}R^2(t)\sin(2\phi(t)) \tag{284}$$

$$=\frac{\pi}{4}-\frac{\sqrt{\pi}N!}{2\Gamma\left(N+\frac{1}{2}\right)}\cos\left(\frac{\xi_0 t}{2}\right)\,{}_2F_1\left(\frac{1}{2},\frac{1}{2}-N;\frac{3}{2};\cos^2\left(\frac{\xi_0 t}{2}\right)\right)-\frac{1}{4}R^2(t)\sin(2\phi(t)) \tag{285}$$

Where ${}_2F_1\left(a,b;c;z\right)$ is the hypergeometric function and we leave the second term implicit since it cancels terms in $\rho\left(t\right)$ and $F_g^2\left(t\right)$.

6.4 Floquet expansion for off resonance drive

6.4.1 Order by order expansion

Given a $\tau=\frac{1}{\xi}$ periodic Hamiltonian:

$$\hat{H}\left(t\right)=\hat{H}\left(t+\tau\right)=\hat{H}_0+\hat{V}\left(t\right) \tag{286}$$

Such that $\hbar\xi\gg\left|\hat{H}_0\right|$, then we postulate a time dependent rotating frame $\hat{U}_{mm}=e^{iF(t)}$ set by the micro-motion operator $\hat{F}\left(t\right)$ which is also τ periodic:

$$i\partial_t\left|\psi\right\rangle=\hat{H}\left|\psi\right\rangle \tag{287}$$

$$e^{i\hat{F}(t)}i\partial_t\left|\psi\right\rangle+i\left(\frac{\partial}{\partial t}e^{i\hat{F}(t)}\right)\left|\psi\right\rangle=e^{i\hat{F}(t)}\hat{H}\left|\psi\right\rangle+i\left(\frac{\partial}{\partial t}e^{i\hat{F}(t)}\right)\left|\psi\right\rangle \tag{288}$$

$$i\frac{\partial}{\partial t}\left(e^{i\hat{F}(t)}\left|\psi\right\rangle\right)=\left(e^{i\hat{F}(t)}\hat{H}e^{-i\hat{F}(t)}+i\left(\frac{\partial}{\partial t}e^{i\hat{F}(t)}\right)e^{-i\hat{F}(t)}\right)\left(e^{i\hat{F}(t)}\left|\psi\right\rangle\right) \tag{289}$$

$$i\frac{\partial}{\partial t}\left|\tilde{\psi}\right\rangle=\hat{H}_F\left|\tilde{\psi}\right\rangle \tag{290}$$

Where in the second line we multiplied by $e^{i\hat{F}(t)}$ from the left and added $i\left(\frac{\partial}{\partial t}e^{i\hat{F}(t)}\right)\left|\psi\right\rangle$. Such that we defined the rotating frame: $\left|\tilde{\psi}\right\rangle=e^{i\hat{F}(t)}\left|\psi\right\rangle$ and the Floquet Hamiltonian:

$$\hat{H}_F=e^{i\hat{F}(t)}\hat{H}e^{-i\hat{F}(t)}+i\left(\frac{\partial}{\partial t}e^{i\hat{F}(t)}\right)e^{-i\hat{F}(t)} \tag{291}$$

We will now construct $\hat{H}_F$ by requiring it to remain time independent, this will enforce the construction of $\hat{F}$ as well. To do so explicitly we expand in a power series of the form:

$$\hat{H}_F=\sum_{n=0}^{\infty}\hat{H}_{F,n},\quad\hat{F}=\sum_{n=1}^{\infty}\hat{F}_n \tag{292}$$

Such that: $\mathcal{O}\left(\hat{H}_{F,n}\right)=\mathcal{O}\left(\hat{F}_n\right)=\mathcal{O}\left(\xi^{-n}\right)$. Making use of the identities (see appendix: 6.4.3):

$$\begin{cases}e^{i\hat{F}}\hat{H}e^{-i\hat{F}}=\hat{H}+i\left[\hat{F},\hat{H}\right]-\frac{1}{2!}\left[\hat{F},\left[\hat{F},\hat{H}\right]\right]-\frac{i}{3!}\left[\hat{F},\left[\hat{F},\left[\hat{F},\hat{H}\right]\right]\right]+...\\ \left(\frac{\partial e^{i\hat{F}}}{\partial\tau}\right)e^{-i\hat{F}}=i\frac{\partial\hat{F}}{\partial\tau}-\frac{1}{2!}\left[\hat{F},\frac{\partial\hat{F}}{\partial\tau}\right]-\frac{i}{3!}\left[\hat{F},\left[\hat{F},\frac{\partial\hat{F}}{\partial\tau}\right]\right]+...\end{cases} \tag{293}$$

Such that in order ξ^{-0} we have:

$$\hat{H}_{F,0} = e^{i\hat{F}(t)}\hat{H}e^{-i\hat{F}(t)} + i\left[\partial_t e^{i\hat{F}(t)}\right]e^{-i\hat{F}(t)} = \hat{H} - \frac{\partial \hat{F}_1}{\partial t} \tag{294}$$

And by demanding a time independent Floquet Hamiltonian:

$$\frac{\partial}{\partial t}\hat{H}_{F,0} = 0 \Rightarrow \hat{F}_1 = \int_0^t dt' \hat{H}\left(t'\right) \tag{295}$$

We note that due to the τ periodicity of $\hat{H}$ then $\hat{F}_1 \sim \mathcal{O}\left(\xi^{-1}\right)$ as required. In addition $\hat{F}_1$ is determined up to a constant Hermitian operator which will not change $\hat{H}_{F,0}$ (and similarly for high orders) .

Following a similar course we can easily construct the next two orders:

$$\begin{cases} \hat{H}_{F,1} = i\left[\hat{F}_1, \hat{H}\right] - \frac{\partial \hat{F}_2}{\partial \tau} - \frac{i}{2}\left[\hat{F}_1, \frac{\partial \hat{F}_1}{\partial \tau}\right] & \mathcal{O}\left(\xi^{-1}\right) \\ \hat{H}_{F,2} = i\left[\hat{F}_2, \hat{H}\right] - \frac{1}{2}\left[\hat{F}_1, \left[\hat{F}_1, \hat{H}\right]\right] - \frac{\partial \hat{F}_3}{\partial \tau} - \frac{i}{2}\left[\hat{F}_1, \frac{\partial \hat{F}_2}{\partial \tau}\right] - \frac{i}{2}\left[\hat{F}_2, \frac{\partial \hat{F}_1}{\partial \tau}\right] + \frac{1}{6}\left[\hat{F}_1, \left[\hat{F}_1, \frac{\partial \hat{F}_1}{\partial \tau}\right]\right] & \mathcal{O}\left(\xi^{-2}\right) \end{cases} \tag{296}$$

And demand time independence order by order.

Finally, the evolution is given by:

$$\hat{U}\left(t\right) = e^{-i\hat{F}(t)}e^{-i\hat{G}t}e^{i\hat{F}(0)} \tag{297}$$

That is, rotating to the time independent frame, evolving a time independent Hamiltonian, and rotating back.

6.4.2 Implementing for off resonance MS gate

In the case of a MS interaction we have the Hamiltonian:

$$\tilde{V}_I = -\eta\Omega\hat{J}_y\left(\hat{a}^\dagger e^{i\xi t} + \hat{a}e^{-i\xi t}\right) + \delta\hat{J}_z \tag{298}$$

Thus, in the notation of the Floquet expansion we have:

$$\hat{H}_0 = \delta\hat{J}_z, \quad \hat{V}\left(t\right) = -\eta\Omega\hat{J}_y\left(\hat{a}^\dagger e^{i\xi t} + \hat{a}e^{-i\xi t}\right) \tag{299}$$

Thus:

$$\hat{F}_1 = \int_0^t dt'\hat{H}\left(t'\right) = \int_0^t dt'\hat{V}\left(t'\right) = \frac{i\eta\Omega\hat{J}_y}{\xi}\left(\hat{a}^\dagger e^{i\xi t} - \hat{a}e^{-i\xi t}\right) \tag{300}$$

Such that:

$$\hat{H}_{F,0} = \hat{H} - \frac{\partial \hat{F}_1}{\partial \tau} = \delta\hat{J}_z \tag{301}$$

In order ξ^{-1} we have:

$$\hat{H}_{F,1} = i\left[\hat{F}_1, \hat{H}\right] - \frac{\partial \hat{F}_2}{\partial \tau} - \frac{i}{2}\left[\hat{F}_1, \frac{\partial \hat{F}_1}{\partial \tau}\right] \tag{302}$$

$$= -\frac{\partial \hat{F}_2}{\partial \tau} + i\left[\frac{i\eta\Omega \hat{J}_y}{\xi}\left(\hat{a}^\dagger e^{i\xi t} - \hat{a}e^{-i\xi t}\right), -\eta\Omega \hat{J}_y\left(\hat{a}^\dagger e^{i\xi t} + \hat{a}e^{-i\xi t}\right) + \delta \hat{J}_z\right] \tag{303}$$

$$- \frac{i}{2}\left[\frac{i\eta\Omega \hat{J}_y}{\xi}\left(\hat{a}^\dagger e^{i\xi t} - \hat{a}e^{-i\xi t}\right), -\eta\Omega \hat{J}_y\left(\hat{a}^\dagger e^{i\xi t} + \hat{a}e^{-i\xi t}\right)\right] \tag{304}$$

$$= -\frac{\partial \hat{F}_2}{\partial t} - \frac{(\eta\Omega)^2 \hat{J}_y^2}{\xi} - \frac{i\eta\Omega\delta}{\xi}\hat{J}_x\left(\hat{a}^\dagger e^{i\xi t} - \hat{a}e^{-i\xi t}\right) \tag{305}$$

Thus:

$$\hat{F}_2 = -\frac{i\eta\Omega\delta}{\xi}\hat{J}_x \int dt' \left(\hat{a}^\dagger e^{i\xi t} - \hat{a}e^{-i\xi t}\right) = -\frac{\eta\Omega\delta}{\xi^2}\hat{J}_x\left(\hat{a}^\dagger e^{i\xi t} + \hat{a}e^{-i\xi t}\right) \tag{306}$$

Such that:

$$\hat{H}_{F,1} = -\frac{(\eta\Omega)^2}{\xi}\hat{J}_y^2 \tag{307}$$

In order ξ^{-2} we have:

$$\hat{H}_{F,2} = i\left[\hat{F}_2, \hat{H}\right] - \frac{1}{2}\left[\hat{F}_1, \left[\hat{F}_1, \hat{H}\right]\right] - \frac{\partial \hat{F}_3}{\partial t} - \frac{i}{2}\left[\hat{F}_1, \frac{\partial \hat{F}_2}{\partial t}\right] - \frac{i}{2}\left[\hat{F}_2, \frac{\partial \hat{F}_1}{\partial t}\right] + \frac{1}{6}\left[\hat{F}_1, \left[\hat{F}_1, \frac{\partial \hat{F}_1}{\partial t}\right]\right] \tag{308}$$

$$= -\frac{\delta^2\eta\Omega}{\xi^2}\hat{J}_y\left(\hat{a}^\dagger e^{i\xi t} + \hat{a}e^{-i\xi t}\right) - \frac{\delta(\eta\Omega)^2}{2\xi^2}\hat{J}_z\left(\hat{a}^\dagger e^{i\xi t} + \hat{a}e^{-i\xi t}\right)^2 - \frac{\partial \hat{F}_3}{\partial t} \tag{309}$$

Thus:

$$\hat{F}_3 = i\frac{\delta^2\eta\Omega}{\xi^3}\hat{J}_y\left(\hat{a}^\dagger e^{i\xi t} - \hat{a}e^{-i\xi t}\right) + \frac{\delta(\eta\Omega)^2}{4\xi^3}i\hat{J}_z\left(\left(\hat{a}^\dagger\right)^2 e^{2i\xi t} - (\hat{a})^2 e^{-2i\xi t}\right) \tag{310}$$

Which leads to:

$$\hat{H}_{F,2} = -\frac{\delta\eta\Omega^2}{\xi^2}\hat{J}_z\left(\hat{a}^\dagger\hat{a} + \frac{1}{2}\right) \tag{311}$$

So up to order ξ^{-3} we have:

$$\hat{H}_F = \hat{J}_z\delta\left(1 - \frac{\delta(\eta\Omega)^2}{\xi^2}\left(\hat{a}^\dagger\hat{a} + \frac{1}{2}\right)\right) - \frac{(\eta\Omega)^2}{\xi}\hat{J}_y^2 + \mathcal{O}\left(\xi^{-3}\right) \tag{312}$$

With:

$$\hat{F} = \frac{i\eta\Omega\hat{J}_y}{\xi}\left(\hat{a}^\dagger e^{i\xi t} - \hat{a}e^{-i\xi t}\right) - \frac{\eta\Omega\delta}{\xi^2}\hat{J}_x\left(\hat{a}^\dagger e^{i\xi t} + \hat{a}e^{-i\xi t}\right) \tag{313}$$

$$+ i\frac{\delta^2\eta\Omega}{\xi^3}\hat{J}_y\left(\hat{a}^\dagger e^{i\xi t} - \hat{a}e^{-i\xi t}\right) + \frac{\delta(\eta\Omega)^2}{4\xi^3}i\hat{J}_z\left(\left(\hat{a}^\dagger\right)^2 e^{2i\xi t} - (\hat{a})^2 e^{-2i\xi t}\right) \tag{314}$$

We will state the next order (which are needed for reasonable results at $\frac{\delta}{\xi} \lesssim 1$):

$$\hat{H}_F = \hat{J}_z \delta \left(1 - \frac{\delta \left(\eta\Omega\right)^2}{\xi^2}\left(\hat{a}^\dagger \hat{a} + \frac{1}{2}\right)\right) - \frac{\left(\eta\Omega\right)^2}{\xi}\left(1 + \frac{\delta^2}{\xi^2}\right)\hat{J}_y^2 + \mathcal{O}\left(\xi^{-3}\right) \tag{315}$$

And:

$$\hat{F} = \frac{i\eta\Omega\hat{J}_y}{\xi}\left(\hat{a}^\dagger e^{i\xi t} - \hat{a}e^{-i\xi t}\right) - \frac{\eta\Omega\delta}{\xi^2}\hat{J}_x\left(\hat{a}^\dagger e^{i\xi t} + \hat{a}e^{-i\xi t}\right) \tag{316}$$

$$+ \frac{1}{\xi^3}\left[i\delta^2\eta\Omega\hat{J}_y\left(\hat{a}^\dagger e^{i\xi t} - \hat{a}e^{-i\xi t}\right) + i\delta\left(\eta\Omega\right)^2\hat{J}_z\left(\left(\hat{a}^\dagger\right)^2 e^{2i\xi t} - \left(\hat{a}\right)^2 e^{-2i\xi t}\right)\right] \tag{317}$$

$$+ \frac{1}{\xi^4}\left[\delta\left(\eta\Omega\right)^3\left(i\frac{29}{12}\hat{J}_z\hat{J}_y\hat{a}^\dagger e^{i\xi t} + \frac{5}{3}\hat{J}_x\hat{a}^\dagger e^{i\xi t} + \frac{11}{24}\hat{J}_x\left(\hat{a}^\dagger\right)^2\hat{a}e^{i\xi t} - \frac{3}{72}\hat{J}_x\left(\hat{a}^\dagger\right)^3 e^{3i\xi t}\right) - \delta^3\eta\Omega\hat{J}_x\hat{a}^\dagger e^{i\xi t} + h.c\right] \tag{318}$$

6.4.3 Commutator identities

We prove the following identities:

$$\begin{cases} e^{i\hat{F}}\hat{H}e^{-i\hat{F}} = \hat{H} + i\left[\hat{F},\hat{H}\right] - \frac{1}{2!}\left[\hat{F},\left[\hat{F},\hat{H}\right]\right] - \frac{i}{3!}\left[\hat{F},\left[\hat{F},\left[\hat{F},\hat{H}\right]\right]\right] + ... \\ \left(\frac{\partial e^{i\hat{F}}}{\partial\tau}\right)e^{-i\hat{F}} = i\frac{\partial\hat{F}}{\partial\tau} - \frac{1}{2!}\left[\hat{F},\frac{\partial\hat{F}}{\partial\tau}\right] - \frac{i}{3!}\left[\hat{F},\left[\hat{F},\frac{\partial\hat{F}}{\partial\tau}\right]\right] + ... \end{cases} \tag{319}$$

For the first we define:

$$\hat{G}\left(x\right) = e^{ix\hat{F}}\hat{H}e^{-ix\hat{F}} = \sum_{n=0}^{\infty}\frac{1}{n!}\hat{G}_n x^n \tag{320}$$

We note that:

$$\frac{\partial\hat{G}}{\partial x} = i\hat{F}e^{ix\hat{F}}\hat{H}e^{-ix\hat{F}} - i\hat{F}e^{ix\hat{F}}\hat{H}e^{-ix\hat{F}} \tag{321}$$

$$= \left[i\hat{F},\hat{G}\left(x\right)\right] = \sum_{n=0}^{\infty}\frac{1}{n!}\left[i\hat{F},\hat{G}_n\right]x^n \tag{322}$$

Comparing with the derivative of the Taylor expansion:

$$\frac{\partial}{\partial x}\sum_{n=0}^{\infty}\frac{1}{n!}\hat{G}_n x^n = \sum_{n=1}^{\infty}\frac{1}{(n-1)!}\hat{G}_n x^{n-1} = \sum_{n=0}^{\infty}\frac{1}{n!}\hat{G}_{n+1}x^n \tag{323}$$

Therefore:

$$\sum_{n=0}^{\infty}\frac{1}{n!}\hat{G}_{n+1}x^n = \sum_{n=0}^{\infty}\frac{1}{n!}\left[i\hat{F},\hat{G}_n\right]x^n \tag{324}$$

So we get a recursion relation

$$\hat{G}_{n+1} = \left[i\hat{F},\hat{G}_n\right], \quad \hat{G}_0 = \hat{H} \tag{325}$$

Hence we get:

$$\hat{G}_n = \underbrace{[i\hat{F}, [i\hat{F}, [i\hat{F}, ...[i\hat{F}}_{n \text{ times}}, \hat{G}]]]...] = i^n \underbrace{[\hat{F}, [\hat{F}, [\hat{F}, ...[\hat{F}}_{n \text{ times}}, \hat{G}]]]...] \tag{326}$$

The identity is obtained by setting $x = 1$.

For the second identity we define:

$$\hat{Y}(x) = \frac{\partial}{\partial t}\left(e^{ix\hat{F}}\right) e^{-ix\hat{F}} \tag{327}$$

And note that:

$$\frac{\partial \hat{Y}}{\partial x} = \frac{\partial}{\partial t}\left(e^{ix\hat{F}} i\hat{F}\right) e^{-ix\hat{F}} + \frac{\partial}{\partial t}\left(e^{ix\hat{F}}\right)\left(-i\hat{X}\right) e^{-ix\hat{F}} \tag{328}$$

$$= i\left[\frac{\partial}{\partial t}\left(e^{ix\hat{F}}\hat{F}\right) - \frac{\partial}{\partial t}\left(e^{ix\hat{F}}\right)\hat{F}\right] e^{-ix\hat{F}} \tag{329}$$

$$= e^{ix\hat{F}} \frac{\partial}{\partial t}\left(i\hat{F}\right) e^{-ix\hat{F}} \tag{330}$$

Therefore:

$$\frac{\partial \hat{Y}}{\partial x} = \frac{\partial\left(i\hat{F}\right)}{\partial t} + ix\left[\hat{F}, \frac{\partial\left(i\hat{F}\right)}{\partial t}\right] - \frac{x^2}{2!}\left[\hat{F}, \left[\hat{F}, \frac{\partial\left(i\hat{F}\right)}{\partial t}\right]\right] - \frac{ix^3}{3!}\left[\hat{F}, \left[\hat{F}, \left[\hat{F}, \frac{\partial\left(i\hat{F}\right)}{\partial t}\right]\right]\right] + ... \tag{331}$$

Integrating on x and setting $x = 1$ we get:

$$\hat{Y} = i\frac{\partial \hat{F}}{\partial t} - \frac{1}{2}\left[\hat{F}, \frac{\partial \hat{F}}{\partial t}\right] - \frac{i}{3!}\left[\hat{F}, \left[\hat{F}, \frac{\partial \hat{F}}{\partial t}\right]\right] + \frac{1}{4!}\left[\hat{F}, \left[\hat{F}, \left[\hat{F}, \frac{\partial \hat{F}}{\partial t}\right]\right]\right] + ... \tag{332}$$

$$= \sum_{n=1}^{\infty} \frac{i^n}{n!} \underbrace{[\hat{F}, [\hat{F}, [\hat{F}, ...[\hat{F}}_{n-1 \text{ times}}, \frac{\partial \hat{F}}{\partial t}]]]...] \tag{333}$$

As required.